https://doi.org/10.5194/egusphere-2026-2109
Preprint. Discussion started: 1 July 2026

Urban atmospheric CO_2 plumes from space - Part 1: Atmospheric modeling of the urban boundary layer

Alohotsy Rafalimanana[1], Thomas Lauvaux[1,2], Charbel Abdallah[1], Mali Chariot[2,3], Michel Ramonet[2], Josselin Doc[2], Olivier Laurent[2], Morgan Lopez[2], Anja Raznjevic[4], Maarten Krol[4], Leena Järvi[5], Andreas Christen[6], Dana Looschelders[6], Leslie David[7], Olivier Sanchez[7], Laura Bignotti[8], Benjamin Loubet[8], Sue Grimmond[9], and William Morrison[10]

[1]Climate Impacts on Environment Laboratory (CIEL), Université de Reims-Champagne Ardenne, EMR CNRS 7007 AEROLAB, Reims, France
[3]Origins.earth, Reims, France
[2]Laboratoire des Sciences du Climat et de l'Environnement (LSCE), IPSL, CEA-CNRS-UVSQ, Université Paris-Saclay, 91191 Gif sur Yvette Cedex, France
[4]Meteorology and Air Quality, Wageningen University, Wageningen, the Netherlands
[5]Institute for Atmospheric and Earth System Research (INAR) / Physics, Faculty of Science, University of Helsinki, Helsinki, Finland
[6]Chair of Environmental Meteorology, Faculty of Environment and Natural Resources, University of Freiburg, Freiburg, Germany
[7]Airparif, Paris, France
[8]ECOSYS, University Paris Saclay, INRAE, AgroParisTech, Palaiseau, France
[9]University of Reading, Reading, United Kingdom
[10]School of GeoSciences, University of Edinburgh, Edinburgh, EH9 3FF, United Kingdom

Correspondence: Alohotsy Rafalimanana: alohotsy.rafalimanana@univ-reims.fr

Abstract. Interpreting atmospheric CO_2 observations over cities from space requires transport models that accurately link concentration patterns to surface fluxes, making realistic urban boundary-layer representation critical. This study examines how urban physics parameterizations influence boundary-layer dynamics and near-surface CO_2 mixing ratios over the Paris metropolitan area under winter and summer conditions. Using the Weather Research and Forecasting model, four configurations are evaluated: no-urban representation (No_URB), a single-layer urban canopy model (SLUCM), and two multi-layer schemes (BEP: Building Effect Parameterization and BEM: Building Energy Model). Model outputs are assessed against surface energy flux observations, turbulence measurements, planetary boundary layer height (PBLH), and near-surface CO_2 mixing ratios from dense urban and suburban monitoring networks, alongside wind, temperature and humidity. Urban physics exert strong control on wintertime boundary-layer structure and CO_2 variability, with scheme differences driven primarily by sensible heat flux, friction velocity, and turbulent kinetic energy, producing large contrasts in PBLH and CO_2 accumulation. In summer, PBLH diurnal patterns converge across schemes, with a characteristic plateau during active convection, and CO_2 variability becomes dominated by convective mixing. BEM provides the most physically consistent representation across both seasons. Sensitivity tests with three planetary boundary layer schemes show that Mellor–Yamada–Janjic coupled with BEM best reproduces wintertime CO_2, capturing realistic nighttime accumulation and daytime mixing, while Yonsei University and BouLac exhibit systematic

https://doi.org/10.5194/egusphere-2026-2109
Preprint. Discussion started: 1 July 2026

biases. These results demonstrate that realistic urban physics combined with an appropriate turbulence scheme are essential for physically consistent urban CO_2 simulations, particularly in winter.

1 Introduction

Urban areas are the dominant sources of anthropogenic carbon dioxide (CO_2) emissions, accounting for more than 70% of global fossil fuel related outputs (Churkina, 2016; Crippa et al., 2021). With cities expected to host two-thirds of the global population by mid-century, reducing urban emissions has become a critical component of climate mitigation strategies (Lwasa et al., 2022). Achieving this goal requires precise monitoring frameworks capable of quantifying emissions at fine spatial and temporal scales, combining socio-economic data to generate fossil fuel emissions inventories (Gurney et al., 2019; Huo et al., 2022), and integrating observations across multiple platforms such as satellites, ground-based sensor networks, and atmospheric models (Che et al., 2024).

In this context, atmospheric CO_2 observations over cities derived from dense ground-based networks or satellite platforms, provide valuable constraints on urban emissions. However, linking observed concentration patterns to surface fluxes depends critically on the realism with which atmospheric transport and mixing processes are represented. Urban environments pose particular challenges for CO_2 modeling because of their heterogeneous emission sources, complex surface morphology, and strong diurnal variability in meteorological conditions (Ye et al., 2020). Boundary-layer dynamics, turbulent mixing, and surface energy partitioning over urban areas play a central role in controlling near-surface CO_2 accumulation and dilution, and therefore directly affect the interpretation of both in situ and remote sensing observations.

More recently, the emergence of dense ground-based CO_2 monitoring networks across large metropolitan areas, *e.g.* Paris (Lian et al., 2024) or San Francisco (Delaria et al., 2021), has revealed small-scale CO_2 enhancements within large urban plumes. In parallel, the increasing availability of satellite column measurements scanning large point sources and cities, *e.g.* the Snapshot Area Mode of OCO-3 (Taylor et al., 2020; Kiel et al., 2021), offer unprecedented spatial coverage but at coarser spatial resolution. Reconciling these different observational perspectives requires transport models that can realistically represent the coupling between urban surface processes, boundary-layer structure, and CO_2 transport across scales (Ye et al., 2025).

Atmospheric inversion systems have emerged as a key tool for estimating urban fossil fuel emissions by assimilating atmospheric CO_2 observations into transport models (Staufer et al., 2016; Lauvaux et al., 2016; Lian et al., 2023). The robustness of these inversion frameworks depends strongly on the accuracy of the underlying transport models (Feng et al., 2016; Chen et al., 2023), particularly in heterogeneous urban environments (Schuh et al., 2021). While mesoscale models operating at kilometer-scale resolution are widely used and capable of capturing regional circulation patterns, their performance in urban areas is sensitive to how surface exchanges, turbulence, and boundary layer processes are parameterized (Gaudet et al., 2017). Inadequate representation of these processes can lead to biases in boundary layer height, vertical mixing, and near-surface concentrations, ultimately affecting inferred emissions.

To address these challenges, the Carbon Atmospheric Tracer Research to Improve Numerical schemes and Evaluation (CATRINE) project aims to evaluate and improve numerical schemes for tracer transport within the Copernicus Anthropogenic

https://doi.org/10.5194/egusphere-2026-2109
Preprint. Discussion started: 1 July 2026

CO_2 Monitoring and Verification Support Capacity. By systematically testing and optimizing transport schemes, CATRINE seeks to enhance the accuracy of CO_2 dispersion simulations in urban environments, thereby improving the robustness of inversion-based emission estimates.

The Weather Research and Forecasting (WRF) model (Skamarock et al., 2019), coupled with its passive tracer capabilities (Lauvaux et al., 2012), has been extensively applied to urban greenhouse gas studies (Lauvaux et al., 2016; Feng et al., 2016; Lei et al., 2021; Lian et al., 2023; Zhao et al., 2023; Danjou et al., 2024; Che et al., 2024). Within WRF, different urban canopy parameterizations are available, ranging from simplified representations to more complex multi-layer schemes that explicitly account for building geometry, energy storage, and momentum exchange. These urban physics schemes directly influence surface heat fluxes, friction velocity, turbulence generation, and planetary boundary layer development, all of which govern near-surface CO_2 variability.

This study constitutes Part 1 of a two-part investigation and focuses on evaluating how different representations of urban physics influence boundary layer dynamics and near-surface CO_2 mixing ratios over Paris. While Lian et al. (2021) examined the sensitivity of simulated atmospheric CO_2 mixing ratios to multiple sources of model uncertainty over the Paris region without ranking the performance of physical parameterizations, the present work evaluates the relative physical realism and predictive skill of urban canopy and planetary boundary layer (PBL) schemes using a multi-variable framework. Previous urban modeling studies have also explored the sensitivity of boundary layer dynamics to physical parameterizations. For example, Sarmiento et al. (2017) assessed the impact of different PBL and urban configurations on boundary layer characteristics over Indianapolis, but without evaluating CO_2 or tracer transport and without considering building energy model (BEM) based urban schemes. Similarly, Díaz-Isaac et al. (2018) conducted sensitivity experiments examining the influence of multiple physical parameterizations, including planetary boundary layer (PBL) schemes, land surface models (LSMs), cumulus, and microphysics schemes, on simulated CO_2 transport; however, their analysis did not include urban canopy parameterizations. Previous work in urban meteorology has highlighted the importance of accurately representing urban surface–atmosphere exchanges and canopy processes. Such representations are critical for simulating boundary layer dynamics and scalar transport in cities (Christen and Vogt, 2004; Grimmond et al., 2010; Loridan et al., 2010; Krayenhoff et al., 2020; Lipson et al., 2022).

Using WRF simulations with multiple urban parameterization schemes, we examine their impacts on surface energy fluxes, turbulence characteristics, planetary boundary layer height (PBLH), and CO_2 mixing ratios during both winter and summer. Rather than relying solely on PBLH as a proxy for vertical mixing, we analyze the variability and distributions of model-observation differences for surface fluxes, turbulence intensity, and PBLH to gain process level insight into urban CO_2 transport. This multi-variable framework enables a systematic evaluation of the relative roles of boundary layer and surface processes across different urban canopy schemes. In addition, we perform sensitivity tests with different planetary boundary layer (PBL) schemes to assess how the representation of turbulence and vertical mixing interacts with urban physics and influences near-surface CO_2 variability.

Model results are evaluated against an extensive observational dataset, including dense CO_2 monitoring networks, meteorological measurements, and boundary-layer observations. Paris serves as an ideal testbed due to the availability of multiscale,

https://doi.org/10.5194/egusphere-2026-2109
Preprint. Discussion started: 1 July 2026

high-quality observations. By systematically comparing urban physics configurations, we aim to identify physically consistent model behavior and assess implications for interpreting urban CO_2 observations.

By identifying the urban physics and PBL configuration that provides the most balanced and physically consistent representation of boundary-layer processes and CO_2 variability, this work establishes a robust baseline for subsequent investigations. In particular, it highlights the extent to which kilometer scale simulations can represent urban CO_2 variability and motivates further exploration of resolution dependence and turbulence resolving approaches. These aspects are addressed in Part 2 of this study, which will investigate the sensitivity of urban CO_2 plumes to horizontal resolution and turbulence resolving method using large eddy simulations.

The remainder of this paper is organized as follows. Section 2 describes the model configuration, urban physics schemes, and observational datasets. Section 3 presents the evaluation of surface fluxes, turbulence, boundary-layer structure, and near-surface CO_2 mixing ratios. Section 4 discusses the physical mechanisms underlying the model behavior and their implications for urban CO_2 monitoring. Section 5 summarizes the main findings and outlines perspectives for high-resolution modeling explored in Part 2.

2 Methodology, Models and Data

Model simulations and observational analyses were conducted for two intensive periods representing winter (10–31 January 2024) and summer (01–20 June 2024), selected to sample contrasting planetary boundary-layer dynamics, surface energy partitioning, CO_2 emission, and associated meteorological conditions such as temperature, relative humidity, and wind. Each simulation included a spin-up period to allow the large-scale circulation and background atmospheric composition to adjust to the model configuration, resulting in total simulation lengths of 31 days for winter and 29 days for summer. The spin-up periods (01–09 January and 23–31 May, respectively) were excluded from the analysis.

The area of study focuses on urban Paris and the surrounding Île-de-France region, a densely populated metropolitan area characterized by strong anthropogenic CO_2 emissions, complex land–atmosphere interactions, and pronounced urban heat island effects. This region encompasses a heterogeneous mix of urban, suburban, and peri-urban land-use types, providing a representative setting to investigate contrasts in surface fluxes, boundary-layer structure, and atmospheric transport processes. Paris, as one of Europe's largest megacities, exhibits marked seasonal variability in energy consumption, traffic density, and biospheric activity, making it particularly suitable for evaluating model performance under contrasting seasonal conditions in CO_2 emissions and meteorological controls on their dispersion. The Île-de-France region also benefits from a dense network of meteorological and atmospheric composition observations, which supports robust evaluation of model performance and facilitates integrated model–observation analyses.

2.1 WRF model configurations

The simulations were performed with the Advanced Research WRF model (WRF-ARW, version 4.6.1) (Skamarock et al., 2019) coupled with the chemistry module (WRF-Chem) (Grell et al., 2005; Peckham et al., 2017). The WRF-Chem module represents

https://doi.org/10.5194/egusphere-2026-2109
Preprint. Discussion started: 1 July 2026

CO_2 as a passive tracer, accounting only for transport and mixing processes while excluding chemical transformations (Lauvaux et al., 2012). The model allows individual surface flux components (e.g., biogenic, fossil fuel, and boundary inflow) to be treated as distinct tracers, thereby enabling the attribution of different sources and sinks within a single simulation. The model configuration consists of a parent domain and two one-way nested domains (Figure 1) centered over Paris, France (2.333° E, 48.666° N). The outermost domain (D01) provides lateral boundary conditions to the inner domains, with information passed from the parent to the nests without feedback to the coarser grid. The horizontal resolution ranges from 8.1 × 8.1 km in D01 to 900 × 900 m in the innermost domain (D03). The WRF-Chem model uses 51 vertical levels extending from the surface up to 50 hPa. The vertical grid is stretched, with finer resolution near the surface and coarser spacing aloft. The lowest model layer has a thickness of approximately 10 m, providing sufficient resolution to resolve near-surface boundary layer processes. Of the 51 levels, about 25 levels are located within the first 1000 m, capturing the bulk of the urban atmospheric boundary layer. This stretching ensures that the model adequately captures turbulence, vertical mixing, and the evolution of CO_2 plumes in the urban atmospheric boundary layer. Table 1 summarizes the principal characteristics of the simulation domains.

(a) Spatial domains used for WRF simulations

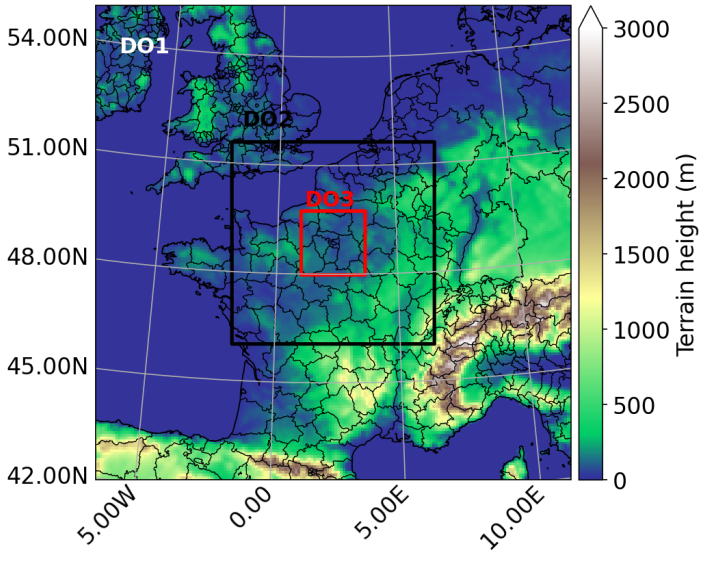

(b) A map showing the observations stations

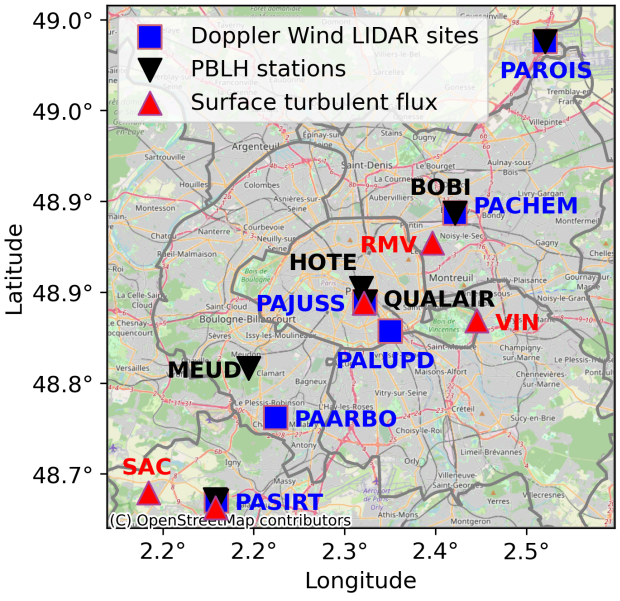

Figure 1. (a) WRF simulation domains with horizontal resolutions ranging from 8.1 km to 900 m. Colormap indicates terrain height (m). (b) Locations of observational sites used in this study. Blue symbols represent Doppler wind LIDAR positions, black symbols indicate the Automatic LIDAR Ceilometers (ALC) locations used for planetary boundary layer height (PBLH) retrievals and red triangles represent surface turbulent flux stations. Some sites host collocated instruments, notably PAROIS, PACHEM, PAJUSS, and PASIRT.

In this study, we examine the physical parameterizations used to represent the surface energy balance and the PBL dynamics in mesoscale mode, while selecting other numerical schemes from previous studies (*i.e.* microphysics, convection, advection

https://doi.org/10.5194/egusphere-2026-2109
Preprint. Discussion started: 1 July 2026

Table 1. Configuration of the nested simulation domains used in this study. For each domain, the table reports the horizontal grid resolution (m) in the x and y directions, the number of horizontal grid points, and the number of vertical levels used in the model

Domains	Resolution (m)	Grid points number	Vertical level number
D01	8100×8100	182×182	
D02	2700×2700	232×232	51
D03	900×900	220×220	

and radiation schemes). The microphysics scheme is set to the Thompson aerosol-aware scheme (Thompson et al., 2008) for the parent domain and to the WRF Single-Moment 5-class scheme (Hong et al., 2004) for nested domains. Longwave and shortwave radiation are computed using RRTMG (Iacono et al., 2008). Urban physics simulations are initially performed using the Mellor–Yamada–Janjic (MYJ) PBL scheme (Janjic, 1990) and the Janjić Eta surface layer (Janjic, 1996), coupled with the Noah land surface model (Chen and Dudhia, 2001). Four urban configurations are tested with MYJ: no urban physics (No_URB), the single-layer urban canopy model (SLUCM; Kusaka et al., 2001), the multi-layer Building Effect Parameterization (BEP; Martilli et al., 2002), and the multi-layer Building Energy Model (BEM; Salamanca and Martilli, 2010). A summary of the urban physics parameterization options used in this study is provided in Appendix A. To further assess sensitivity to PBL scheme, additional simulations are performed using BEM coupled with three PBL schemes: Mellor–Yamada–Janjic (MYJ), Yonsei University (YSU: Hong et al., 2006), and Bougeault–Lacarrère (BouLac; Bougeault and Lacarrere, 1989). For YSU, the surface layer is represented using the revised MM5 Monin–Obukhov formulation (Jiménez and Dudhia, 2012), while MYJ and BouLac retain the Janjić Eta surface layer. With horizontal resolutions ranging from 900 m to 8.1 km, larger-scale convection is explicitly resolved in all model domains, and no cumulus parameterization is required.

To improve the performance of the WRF simulations, the model was run with the Four Dimensional Data Assimilation (FDDA) scheme (Stauffer and Seaman, 1994) using meteorological measurements collected and quality-controlled by the World Meteorological Organization (WMO). Both surface observations and upper-air data (including rawinsondes and aircraft measurements) were assimilated online within all domains, which were operated in mesoscale mode. In total, 934 stations were assimilated over domain D01 (8.1 km resolution), 157 stations over domain D02 (2.7 km), and 11 stations over domain D03 (900 m), with updates performed every three hours.

2.2 Model Input Data

Initial and boundary meteorological conditions were provided by the European Centre for Medium-Range Weather Forecasts (ECMWF) ERA5 reanalysis (Hersbach et al., 2020). ERA5 offers hourly meteorological fields at 0.25°× 0.25° horizontal resolution, required to drive the WRF model, ensuring realistic synoptic conditions.

For surface characteristics, both topography and land cover were represented with high-resolution datasets to ensure consistency with the fine model grid spacing. In urban areas, where complex surface features strongly influence atmospheric dynamics, the use of high-resolution topography is particularly important. Several studies (Feng et al., 2016; Hedelius et al.,

https://doi.org/10.5194/egusphere-2026-2109
Preprint. Discussion started: 1 July 2026

2017; Wolf et al., 2020; Sun et al., 2024) have highlighted the critical role of fine-scale topographic inputs for accurate simulation of urban greenhouse gas distributions. Topographic data were obtained from the Copernicus Global Digital Elevation Model (CGDEM) provided by the European Space Agency (Agency, 2024), with 3 arc-seconds ($\sim$ 90 m) for the 900 m domains, and Global Multi-resolution Terrain Elevation Data (GMTED, 30 arc-seconds, $\sim$ 1 km) for the outer domains (2.7 km and 8.1 km). The higher-resolution CGDEM datasets capture fine terrain variability, reduce biases associated with smoothed surfaces, and enable more realistic surface–atmosphere interactions across scales. Land use and land cover (LULC) came from the hybrid 100 m CGLC-MODIS-LCZ dataset: combining Copernicus Global Land Service Land Cover, Moderate Resolution Imaging Spectroradiometer, and Local Climate Zones (Demuzere et al., 2023). This dataset provides a detailed description of urban and natural surfaces with a total of 61 land cover categories. It incorporates 10 urban built types, capturing the heterogeneity of urban surfaces. This heterogeneity influences roughness length, albedo, heat and moisture fluxes, and biogenic CO_2 exchanges. Accurate LULC input is particularly important in urban simulations, where spatial variations in land use strongly affect atmospheric mixing, heat islands, and pollutant dispersion.

Anthropogenic CO_2 emissions were obtained from a combination of two inventories with complementary strengths: the Netherlands Organisation for Applied Scientific Research (TNO) inventory (Super et al., 2020) (resolution: 1 km) and the Airparif inventory (resolution: 500 m). The Airparif dataset (Figure 2a) was applied over the Ile-de-France region, where its finer spatial detail provides a more realistic representation of emission patterns. The Airparif CO_2 inventory for 2019 estimates total emissions in the Île-de-France region at 39.4 Mt CO_2 yr^{-1}, with a strong dominance of small combustion sources associated with residential and tertiary heating (35.8%), followed by road transport (29.9%) (Table 2). Industrial activities, waste treatment, and power generation together account for approximately one quarter of regional emissions, while aviation, fugitive emissions, and other mobile sources provide smaller but non-negligible contributions. Emissions from solvents, shipping, and agricultural sectors are marginal. This sectoral distribution highlights the predominance of diffuse urban sources, which are particularly relevant for simulating urban CO_2 mixing ratios and their interaction with boundary-layer dynamics. This detailed, high-resolution inventory provides a robust foundation for WRF-Chem simulations of CO_2 tracers, offering spatially and sectorally resolved emission inputs that enhance the representation of anthropogenic carbon fluxes and support the evaluation of atmospheric CO_2 dynamics over the Paris metropolitan area.

Outside this region, the TNO inventory was used to ensure complete domain coverage. Since Airparif does not separate point and area sources, TNO point-source information was used to correct the Airparif emissions, ensuring a consistent representation of large emitters. This hybrid approach maximizes the spatial detail of the emissions while preserving source specificity.

Human respiration, which may contribute approximately 8–10% of total urban CO_2 emissions, was not included in the emission inventories used in this study, as this component had not yet been incorporated into the TNO and Airparif inventories at the time the simulations were conducted. Its recent inclusion in updated inventory versions represents a refinement to be considered in future work.

The annual CO_2 emissions from the inventory are first mapped onto the WRF-Chem grid and then converted to hourly emission rates using a scaling factor. The temporal disaggregation applies sector-specific scaling factors cascading from annual to monthly, weekly, daily, and hourly timescales. Since the spatial distribution of emission sectors varies across the domain,

https://doi.org/10.5194/egusphere-2026-2109
Preprint. Discussion started: 1 July 2026

Table 2. Sectoral CO_2 emissions in the Île-de-France region for 2019 based on the Airparif inventory.

Emission sector	**Emissions (Mt CO_2 yr^{-1})**	**Share (%)**
Small combustion (residential and tertiary heating)	14.10	35.8
Road transport	11.79	29.9
Industry	3.97	10.1
Waste	3.82	9.7
Power plants	2.80	7.1
Aviation	1.37	3.5
Fugitive emissions	0.67	1.7
Other mobile sources	0.61	1.5
Solvents	<0.5	<1
Shipping	<0.5	<1
Agricultural livestock	<0.5	<1
Other agricultural sources	<0.5	<1
Total	**39.4**	**100**

the effective diurnal emission cycle differs spatially as a natural consequence of the sector-specific temporal profiles and their geographic distribution. Uncertainties in these temporal profiles, particularly for sectors with variable activity patterns, may introduce phase errors in simulated near-surface CO_2 mixing ratios during morning and evening transition periods. Since all model configurations use identical emission inputs, however, such uncertainties affect all urban physics schemes equally and do not influence the intercomparison conclusions of this study.

The emissions are released at the first vertical model level, representing near-surface sources across the domain as the emission inventories do not provide source height information. While this layer is only ∼10 m deep and may not fully represent elevated sources such as vehicle exhaust or rooftop chimneys, using it provides a practical approximation of near-surface CO_2 emissions. This approach may lead to underestimation of tracer concentrations at rooftop sensor heights, where vertical mixing governs transport from the lowest layer.

Biogenic CO_2 fluxes were simulated using the Vegetation Photosynthesis and Respiration Model (VPRM), a satellite-based biosphere parameterization designed to represent net ecosystem exchange through the combined effects of photosynthesis and respiration (Mahadevan et al., 2008). VPRM estimates biogenic CO_2 exchange as a function of vegetation type, phenology, and meteorological drivers, relying on remotely sensed indicators of vegetation activity. In this study, the required surface input parameters for VPRM, including the Enhanced Vegetation Index (EVI), Land Surface Water Index (LSWI), and vegetation fraction (VEG_FRA), were generated using the wrf_preprocessor module of the PyVPRM package (Glauch et al., 2025). The vegetation fraction and land cover information were derived from the Copernicus Global Land Service Land Cover dataset at 100 m resolution (Buchhorn et al., 2020), while EVI and LSWI were computed from the MODIS/Terra Surface Reflectance 8-Day L3 Global 500 m SIN Grid V061 product (Eric, 2021). We note that in dense urban areas, EVI and LSWI are strongly

https://doi.org/10.5194/egusphere-2026-2109
Preprint. Discussion started: 1 July 2026

influenced by mixed pixels and low vegetation fractions, and therefore may not fully capture the small-scale variability of urban vegetation. This preprocessing step ensures overall consistency between the biospheric flux calculations and the WRF model land surface representation, enabling the direct integration of biogenic CO_2 fluxes into the WRF-Chem modeling system at the model grid scale.

Accurate simulation of tracer transport and dispersion in WRF-GHG requires the use of real-world boundary data from global models, which provide realistic lateral boundary conditions. Boundary and background CO_2 fields were provided by the Copernicus Atmosphere Monitoring Service (CAMS; Agustí-Panareda et al., 2023; Inness et al., 2019). We used CAMS global CO_2 reanalysis ($1° \times 1°$, 3-hourly), which assimilates both satellite and in situ observations within an inversion framework to constrain surface fluxes and large-scale transport (Chevallier et al., 2007). These fields ensure that the regional WRF-GHG simulations are consistent with large-scale CO_2 variability and background concentrations.

2.3 Observational datasets

For the validation of surface meteorology in the WRF-GHG simulations, observations from approximately 86 automatic weather stations distributed across Paris and the Île-de-France region were used. These stations are part of the French operational meteorological network coordinated by Météo-France and ACTRIS-FR (Aerosols, Clouds, and Trace gases Research InfraStructure - France), with data accessed through the AERIS (Atmosphere Data and Services Centre) data infrastructure (ACTRIS-FR and Météo-France, 2024). The dataset provides high-frequency surface observations at a 6 minute temporal resolution; in this study, only air temperature, relative humidity, wind speed, and wind direction were considered. Data availability varied among stations, not all stations provided complete records for all variables, particularly wind measurements; therefore, performance metrics were calculated using the subset of stations providing valid observations for each parameter. These observations were used to evaluate WRF-Chem performance at 900 m resolution for different urban physics parameterizations (No_URB, SLUCM, BEP, and BEM) by comparing modeled and observed values across all stations. Model evaluation focused on the subset of 44 meteorological stations located within the polygon covering the Greater Paris area, which coincides with the spatial extent of the CO_2 observation network. This ensures that the evaluation of surface meteorology is directly relevant to tracer transport analyses and the interpretation of urban physics effects on local boundary-layer processes.

To complement the near-surface meteorological comparison and to assess the WRF-Chem model's ability to represent the vertical structure of the urban atmospheric boundary layer, wind profile data from six Doppler wind LIDAR stations (Figure 1b) were used. Details of the station locations, including latitude, longitude, and altitude, are listed in Table B1. These observations are part of a multi-institution Doppler wind LIDAR dataset (Morrison et al., 2025), which includes measurements collected during the *urbisphere* project (Fenner et al., 2024). These LIDARS provide high-resolution measurements of wind speed and direction throughout the lower troposphere with a temporal resolution of 10 minutes. They are essential for evaluating boundary layer dynamics, turbulence, and vertical mixing, which directly influence the dispersion of CO_2 plumes.

Observations of PBLH derived from Automatic LIDAR Ceilometers (ALC) were used for validation (Kotthaus et al., 2020, 2023). The measurements were obtained using seven Vaisala CL61 ceilometers deployed during the *urbisphere* campaign (Figure 1b). Additional ceilometer observations from the PALAISEAU and QUALAIR stations were accessed via the Institut

https://doi.org/10.5194/egusphere-2026-2109
Preprint. Discussion started: 1 July 2026

Pierre-Simon Laplace (IPSL) Compute and Data Centre. Details of the station locations, including latitude, longitude, and altitude, are listed in Table D1. Aerosol-based mixed-layer height (MLH) was determined using the STRATfinder algorithm, with automated quality control applied via the quality control STRATfinder procedure, following the methodology described by Looschelders et al. (2025). The *urbisphere* ceilometer observations are available at a 1 minute temporal resolution, while data from the PALAISEAU and QUALAIR stations are provided at 15 minutes resolution. The observed PBLH was then compared with the modeled PBLH to evaluate the model's performance in capturing the temporal evolution and vertical structure of the urban boundary layer.

Observations of surface sensible heat (HFX) and latent heat (LH) fluxes, friction velocity (u_*) and turbulent kinetic energy (TKE) from seven stations were used to evaluate the modeled surface energy balance and turbulence intensity (Figure 1b). These measurements were obtained from the ICOS ETC Level-2 fluxes data product (Berveiller et al., 2026; Stagakis et al., 2025; Buysse et al., 2026; ICOS et al., 2025) and from the long-term measurements at SIRTA (Lohou et al., 2018), and are available at a 30 minute temporal resolution. At the SIRTA site, flux observations from the 50 m tower were used. The 2 m tower was not considered, as its footprint is limited to a small grassland area and is therefore not representative of the suburban surface conditions resolved by the model grid. The 50 m tower provides a larger and more representative footprint, although it remains dominated by vegetation. The geographical coordinates and altitudes of the stations are provided in Table C1. The multi-station observations enable assessment of the spatial and diurnal variability of surface fluxes and turbulence across different urban environments and provide a basis for evaluating the performances of the different urban physics parameterizations, and more specifically their ablity to reproduce the observed energy balance and turbulence dynamics, with implications for urban CO_2 mixing ratios.

Two complementary surface CO_2 networks (Figure 2b) were used to validate spatial and temporal aspects of WRF-Chem simulations. First, the Paris network of high-precision cavity ring-down spectroscopy sensors provide continuous (Picarro; Doc et al., 2024), accurate CO_2 measurements at multiple urban sites. A second network (mid-cost; Lian et al., 2024) of distributed rooftop sensors offer broader spatial coverage, albeit at lower precision using SenseAir HPP and K96 instruments. Details of each station's position and elevation are summarized in Tables E1 and E2. Both datasets provide hourly CO_2 mixing ratios and are used to assess model performance at 900 m resolution, specifically to evaluate how different urban physics parameterizations influence the model's ability to capture short-term variability, to reproduce diurnal cycles, and to represent spatial gradients and emission-driven CO_2 mixing ratios peaks across the urban domain. For the model-observation comparison, simulated CO_2 mixing ratios were extracted at the model level closest to the measurement height of each station.

2.4 Evaluation strategy and statistical metrics

To examine the influence of urban physics representations on simulated near-surface CO_2 mixing ratios, model results are compared with observations over a 21-day winter period (10–31 January 2024) and a 19-day summer period (01–20 June 2024). The site level time series and diurnal cycles analysis focuses on two urban-core sites, JUS (Picarro network) and EIF (Mid-cost network), and one suburban site, SAC, providing complementary perspectives on CO_2 variability across contrasting urban environments, while aggregated statistics are computed over all stations.

https://doi.org/10.5194/egusphere-2026-2109
Preprint. Discussion started: 1 July 2026

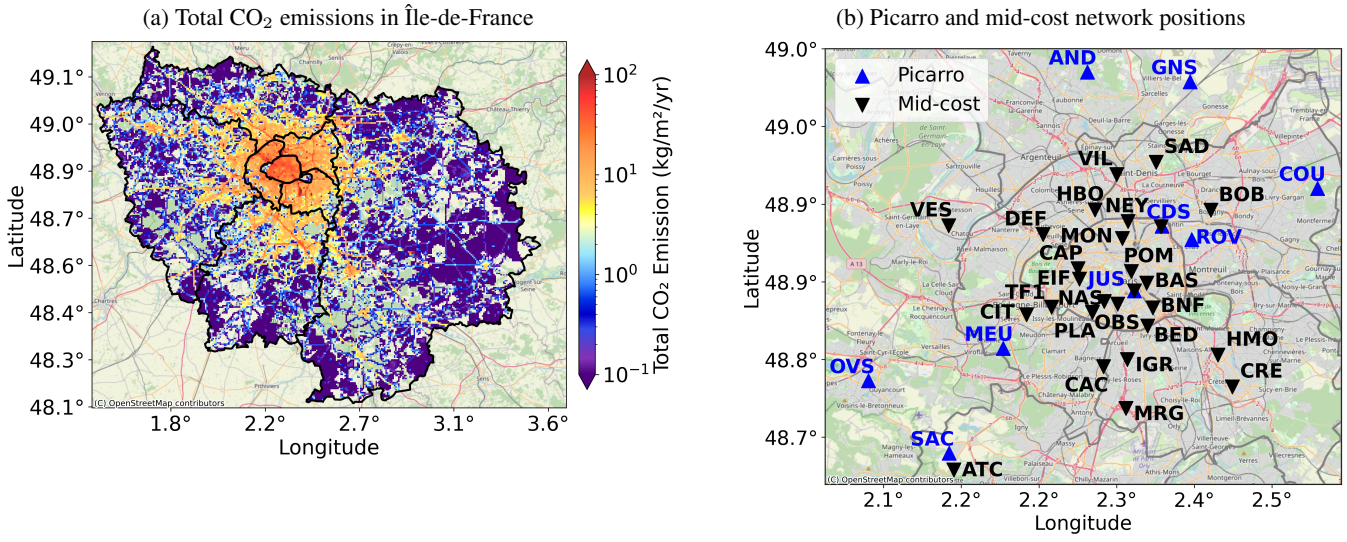

Figure 2. (a) Total CO_2 emissions in Île-de-France from Airparif inventories (2019). (b) Paris area showing Picarro and mid-cost (HPP and K96) network positions.

The impact of urban representation on surface energy exchanges is evaluated by comparing four simulations: without urban physics (No_URB), using the single-layer urban canopy model (SLUCM), the Building Effect Parameterization (BEP), and the Building Energy Model (BEM), all performed at 900 m horizontal resolution.

The WRF simulations at 900 m resolution produced output every 10 minutes intervals. To ensure consistent comparison with observational data, observations with finer temporal resolution (e.g., 1 minute) were averaged to 10 minutes to match the model output, while hourly observations were compared against hourly-averaged model output. This procedure allows us to preserve sub-hourly variability where possible without introducing inconsistencies between datasets.

For surface and boundary layer variables, including sensible heat flux (HFX), latent heat flux (LH), friction velocity (u_*), and planetary boundary layer height (PBLH), WRF outputs three-dimensional fields as functions of time and horizontal position. For the inter-comparison, PBLH is diagnosed using the bulk Richardson number method, where the PBLH is defined as the lowest level at which the bulk Richardson number exceeds a critical threshold (Stull, 1988; Vogelezang and Holtslag, 1996). Model values were therefore extracted from the grid cell corresponding to each observation site. Given the 900 m horizontal resolution of the WRF model, which is comparable to the typical spatial extent of the dominant eddy-covariance flux footprints (Kljun et al., 2015), the majority of the flux contribution is expected to originate from within or near the grid cell containing the tower. However, the effective footprint depends on wind direction and atmospheric conditions, and different landscape elements within the grid cell may contribute unevenly to the measured fluxes. Although footprint extent varies with atmospheric stability and wind conditions, it generally remains of the same order as the model resolution. As a result and given the mismatch between the fine-scale footprint variability and the model grid resolution, no additional spatial averaging or footprint weighting was applied.

https://doi.org/10.5194/egusphere-2026-2109
Preprint. Discussion started: 1 July 2026

For near-surface meteorological variables (air temperature, humidity, wind speed, and wind direction), variations in instrument height among stations were accounted for by selecting the model level closest to the respective measurement height. The same approach was applied to simulated CO_2 mixing ratios and turbulence kinetic energy (TKE).

Model performance is evaluated using complementary statistical metrics: the correlation coefficient (R), mean bias error (MBE), mean absolute error (MAE), and root mean square error (RMSE). Statistics are computed over daytime periods only, when surface–atmosphere coupling is strongest and fluxes are sufficiently developed. The specific daytime evaluation windows depend on the variable considered and are defined to reflect the underlying physical processes governing each quantity.

For surface fluxes (HFX, LH, u_*, and TKE) statistics are computed between 10–16 UTC in winter and 09–18 UTC in summer, when they are sufficiently strong to ensure meaningful surface–atmosphere coupling and to avoid early morning and late evening conditions characterized by weak or near-zero fluxes.

The statistical evaluation of PBLH focuses on the main convective period (10–17 UTC in winter and 10–19 UTC in summer), encompassing the growth, peak, and early decay phases of the daytime boundary layer. This evaluation window is shifted slightly later than that used for surface heat fluxes to account for the delayed, integrated response of boundary-layer development to sustained surface heating. Differences between modeled and observed PBLH should be interpreted with caution, as they are derived using different methods, with observations typically based on aerosol backscatter and the model relying on Richardson number based diagnostics. It should be noted that summertime PBLH evaluation is limited to the Qualair and Palaiseau sites due to data availability, whereas winter statistics are computed over the full observational network.

For near-surface CO_2 mixing ratios, daytime statistics focus on periods of active turbulent mixing (11–16 UTC in winter and 10–18 UTC in summer), allowing assessment of how urban driven boundary layer processes influence concentration biases.

In contrast to surface fluxes, PBLH, CO_2, which are evaluated during daytime hours to focus on periods of active turbulence and boundary layer development, near-surface meteorological variables and wind profile are evaluated over the full diurnal cycle.

Additionally, model–observation comparisons are visualized using diurnal cycles, scatterplots, time series, vertical profiles, spatial transects, and distribution plots to illustrate temporal evolution, spatial variability, correlation, and overall variability of the studied variables.

3 Results

3.1 Impact of urban physics on surface heat flux

The analysis focuses on sensible heat flux (HFX) and latent heat flux (LH) to evaluate WRF model's ability to represent surface–atmosphere energy exchanges across different urban physics configurations in both winter and summer.

The temporal evolution of surface fluxes is examined using diurnal cycles at two representative sites: Jussieu (JUS), located in the dense urban core of Paris, and SIRTA, representative of a suburban environment. These sites are selected to illustrate the contrasting surface energy exchange characteristics of urban and suburban areas and to diagnose the physical response of each urban physics scheme.

https://doi.org/10.5194/egusphere-2026-2109
Preprint. Discussion started: 1 July 2026

Figure 3a and Figure 3b illustrate the diurnal evolution of HFX at JUS, representative of the dense urban core of Paris, for winter and summer, respectively. Across all urban physics configurations and seasons, the simulated HFX exhibits a consistent temporal structure, with a clear morning increase, a midday maximum, and an afternoon decay. This indicates that the timing of surface energy forcing is well captured by WRF, and that differences among urban physics schemes primarily affect the magnitude of HFX rather than its phase.

In winter at JUS, the observed HFX increases shortly after sunrise (∼08:30 UTC), peaks around midday (12–13 UTC), and declines toward a quasi-stable state by late afternoon (∼16 UTC), consistent with the diurnal cycle of solar forcing. Both the No_URB and SLUCM configurations reproduce this diurnal evolution but systematically underestimate the flux throughout the daytime, reflecting insufficient surface heating. This behavior highlights the inability of simplified or absent urban representations to capture the combined effects of urban heat storage, radiative trapping, and canyon-induced turbulence. In contrast, the BEP scheme strongly overestimates HFX during the active daytime period, indicating excessive heat release associated with its parameterized building effects and enhanced roughness-driven mixing. The BEM configuration also overestimates HFX but remains substantially closer to observations, particularly during peak daytime hours, suggesting a more realistic representation of urban heat storage and surface–atmosphere exchange. We note that the JUS flux tower has a local footprint that is small compared to the 900 m WRF grid cell. Therefore, some differences between modeled and observed HFX may reflect the mismatch between the local measurements and the grid-averaged surface characteristics rather than model errors.

During summer at JUS, HFX increases earlier in the day (around 05 UTC), peaks near 12–13 UTC, and decreases gradually until approximately 20 UTC. All configurations overestimate HFX during the active daytime period, but the magnitude of the bias is smaller in absolute terms than in winter. Among the tested schemes, BEM again provides the closest agreement with observations during daytime hours. At night, HFX are generally low. No_URB and SLUCM produce smaller nighttime fluxes, which happen to be close to observations, whereas BEP and BEM maintain elevated fluxes due to urban heat storage and release.

Nighttime HFX is higher in winter for BEP than in summer, reflecting the seasonal differences in stored building heat release. BEM shows lower nighttime HFX than BEP in winter because its additional processes redistribute energy more gradually, retaining some flux within building interiors or partitioning it differently.

At the suburban SIRTA site (Figure 3c and Figure 3d), observed HFX magnitudes are weaker than at JUS in both seasons, reflecting lower building density and reduced heat storage. This difference also reflects the stronger latent heat flux (LH) at SIRTA (Figures 4c and 4d), which reduces the fraction of net radiation partitioned into sensible heat. In the WRF model, winter HFX at SIRTA remain lower than at JUS, consistent with the suburban setting, while summer fluxes reach magnitudes similar to the urban site. In winter, all urban physics configurations capture the timing of the observed diurnal cycle reasonably well. BEP significantly overestimates the flux, and BEM also overestimates it but to a lesser extent. Because winter HFX magnitudes are generally low and LH is limited, the No_URB and SLUCM configurations reproduce the observed diurnal variations reasonably well, suggesting that the representation of building cover at SIRTA is adequate even in the simpler schemes. During summer, all configurations exhibit similar daytime behavior, mirroring the pattern seen at the urban site JUS, with overestimation of daytime HFX. This overestimation may partly reflect excessive surface–atmosphere coupling in the model, and could also be influenced by underestimated LH (Figure 4d) due to factors such as soil moisture, vegetation characteristics, or local atmospheric humidity.

https://doi.org/10.5194/egusphere-2026-2109
Preprint. Discussion started: 1 July 2026

To complement the site-specific diurnal analysis, Table 3 summarizes the statistical performance of each configuration across all available observation sites during daytime periods. HFX simulations exhibit strong sensitivity to urban physics parameterization in both winter and summer. In winter, No_URB and SLUCM show low correlations with observations and systematic negative biases, confirming the underestimation observed in the diurnal cycles. BEP substantially improves temporal variability but introduces a pronounced positive bias, consistent with its overestimation of daytime fluxes. BEM achieves the best overall balance between correlation and bias reduction, providing the most physically consistent representation of HFX. Similar relative performance is observed in summer, despite higher absolute flux magnitudes, with BEM consistently reducing bias compared to BEP and outperforming simpler schemes.

Taken together, the diurnal and statistical analyses demonstrate that WRF captures the timing of HFX well across all configurations, while the magnitude of surface–atmosphere heat exchange is strongly controlled by urban physics. Simplified or absent urban schemes underestimate urban heating, BEP tends to over-enhance sensible heat release and BEM provides the most realistic representation across seasons and site types. These results underscore the critical role of detailed urban parameterizations in simulating urban surface energy exchange and provide a robust foundation for subsequent analyses of turbulence, boundary-layer development, and urban CO_2 transport.

LH exhibits a weaker diurnal amplitude than HFX at both sites, except at SIRTA in summer, reflecting the secondary role of evapotranspiration in the urban surface energy balance, particularly during winter.

At the dense urban site JUS, the No_URB configuration produces near-zero LH throughout the day in both seasons and does not reproduce a clear diurnal cycle (Figures 4a and 4b). This behavior reflects the absence of explicit urban vegetation and limited moisture availability in the land-surface representation, leading to strongly suppressed evapotranspiration.

In contrast, SLUCM, BEP, and BEM reproduce a coherent diurnal evolution, with LH increasing after sunrise, reaching a midday maximum, and decreasing toward evening. In JUS in summer, maximum LH values reach approximately 50 W m^{-2}, approximately twice the winter maxima, consistent with stronger radiative forcing and enhanced seasonal vegetation activity. While the timing of the diurnal cycle is similar across urban schemes, their magnitudes differ substantially. SLUCM produces LH closest to the observed daytime values, whereas BEP tends to underestimate LH, and BEM slightly overestimates it, although with smaller deviations from observations than BEP. These differences highlight the sensitivity of urban evapotranspiration to the treatment of vegetation, surface moisture, and energy partitioning within each urban physics scheme.

At the suburban SIRTA site, LH are generally similar to those at the urban site JUS during winter (Figure 4c), No_URB, SLUCM and BEP configurations tend to underestimate LH during the active daytime period, while BEM showing a similar variation relative to observations. In summer, observed LH at SIRTA is stronger than at JUS, reflecting higher vegetation cover and greater soil moisture availability (Figure 4d). Despite this, all configurations underestimate LH: No_URB produces almost no LH, while BEM remains the highest among them.

Table 3 further evaluates the performance of LH simulations using daytime statistics aggregated across all observation sites. In winter, LH exhibits very weak correlations and comparable error magnitudes (MAE and RMSE) across all configurations, indicating limited sensitivity to urban canopy parameterization under conditions of strongly suppressed evapotranspiration. During summer, when evapotranspiration becomes more active, differences among urban representations become more discernible.

https://doi.org/10.5194/egusphere-2026-2109
Preprint. Discussion started: 1 July 2026

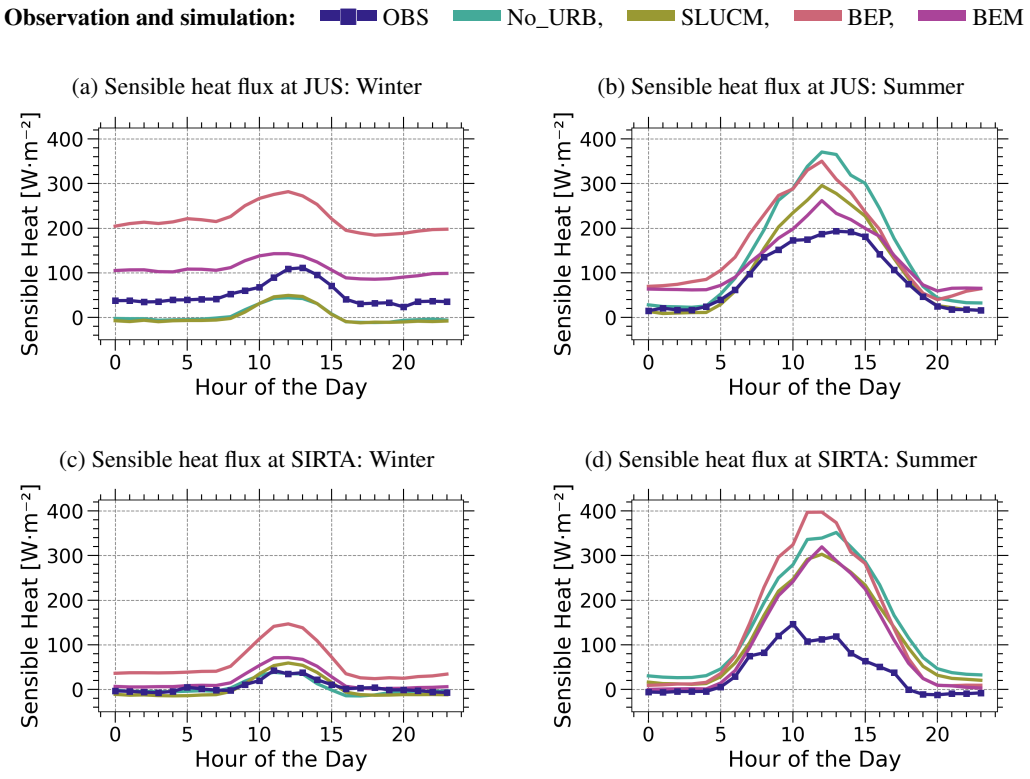

Figure 3. Diurnal cycles of sensible heat flux comparing observations with WRF simulations at 900 m horizontal resolution for different urban physics schemes. Panels (a) and (b) show winter (10–31 January 2024) and summer (01–20 June 2024) conditions, respectively, at the urban core site Jussieu (JUS). Panels (c) and (d) show winter and summer conditions, respectively, at the suburban site SIRTA. Diurnal cycles illustrate the temporal evolution and magnitude of sensible heat flux under contrasting urban representations.

Simulations without an urban scheme (No_URB) show reduced skill in capturing the spatial and temporal variability of LH, while SLUCM and BEP improve the representation of variability. Nevertheless, the differences among the urban schemes remain modest. BEM tends to produce higher LH values compared to the other schemes but maintains error levels comparable to the other configurations, indicating that its strong performance for HFX is achieved without degrading latent heat flux simulations. Overall, these results confirm that LH plays a secondary but seasonally dependent role in the urban energy balance, with improved yet still challenging representation during summer conditions.

These findings indicate that LH is weakly constrained by urban physics during winter but becomes increasingly sensitive to land-surface and urban parameterizations in summer, particularly in suburban environments. Compared with HFX, LH exerts weaker control on boundary-layer development during the study period, but it contributes to modulating the partitioning of surface energy and the seasonal evolution of near-surface turbulence.

https://doi.org/10.5194/egusphere-2026-2109
Preprint. Discussion started: 1 July 2026

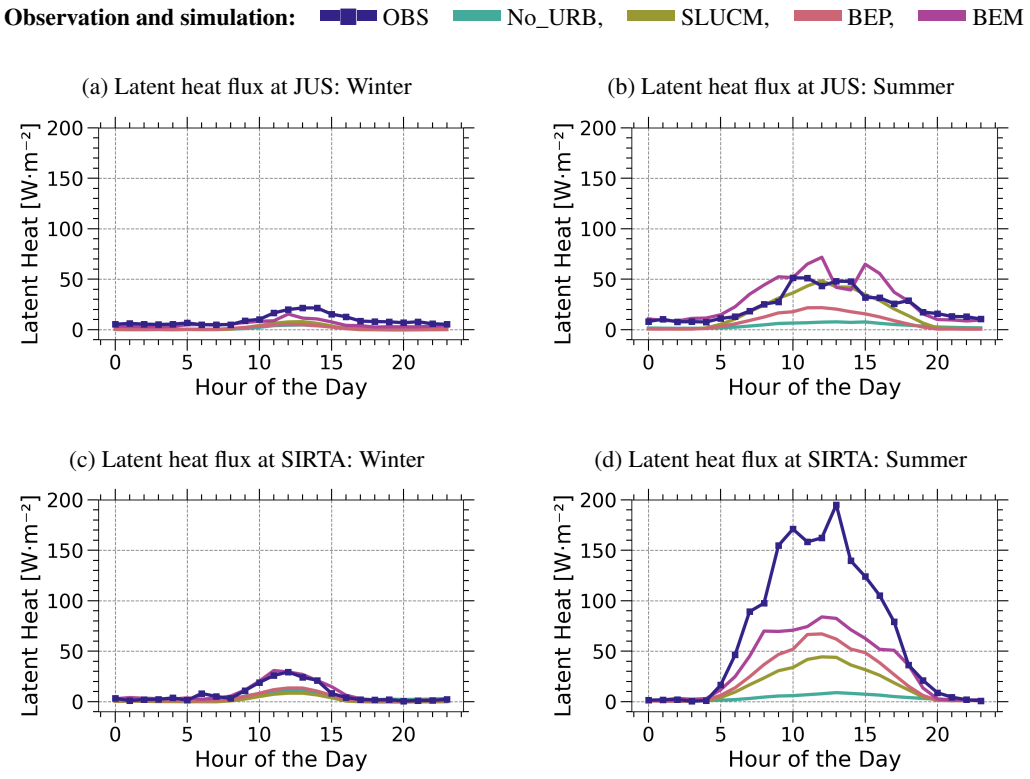

Figure 4. Same as Figure 3, but for latent heat flux.

3.2 Impact of urban physics on friction velocity and turbulent kinetic energy

While surface heat fluxes determine the available energy for atmospheric mixing, the actual efficiency of vertical and horizontal transport within the urban boundary layer is controlled by turbulence intensity. To better understand the mechanisms linking urban surface representation to boundary-layer development and tracer transport, we analyze friction velocity (u_*) and turbulence kinetic energy (TKE), which characterize shear-driven and buoyancy-driven turbulence, respectively. Both u_* and TKE are used here as diagnostics of how urban physics schemes influence boundary layer mixing and associated differences in PBLH and near-surface CO_2.

u_* exhibits a clear diurnal cycle at both sites and in both seasons. Compared to surface heat fluxes, u_* is less directly driven by radiative forcing and is instead strongly controlled by the representation of urban morphology and momentum exchange within the surface layer.

At the dense urban site JUS, the No_URB and SLUCM configurations reproduce the observed diurnal evolution of u_* reasonably well in both winter and summer (Figures 5a and 5b). In winter, both schemes slightly underestimate u_* during daytime hours, consistent with their simplified treatment of urban roughness elements. In summer, No_URB produces a small daytime overestimation, while SLUCM continues to slightly underestimate u_*, indicating modest differences in how surface

https://doi.org/10.5194/egusphere-2026-2109
Preprint. Discussion started: 1 July 2026

Table 3. Statistical evaluation of surface heat flux simulated by WRF at 900 m resolution for winter (10-31 January) and summer (01-20 June) periods. Data are averaged over the active daytime period (10–16 UTC in winter and 09–18 UTC in summer. Results are shown for four urban physics configurations: No_URB, SLUCM, BEP, and BEM. Statistics include the correlation coefficient (R), mean bias error (MBE), mean absolute error (MAE) and root mean square error (RMSE), are computed across all available observation sites.

		Winter (January)				Summer (June)			
Variable	**Scheme**	R	MBE	MAE	RMSE	R	MBE	MAE	RMSE
Sensible Heat Flux ($W\ m^{-2}$)	No_URB	0.37	-12.7	37.9	50.6	0.50	128.9	140.2	168.3
	SLUCM	0.36	-7.8	37.6	49.6	0.47	86.9	104.0	126.6
	BEP	0.64	91.0	102.9	126.7	0.46	110.1	124.6	155.1
	BEM	0.64	30.8	44.7	57.1	0.53	71.9	92.2	118.2
Latent Heat Flux ($W\ m^{-2}$)	No_URB	0.1	4.5	20.1	26.8	0.48	-10.6	95.0	120.0
	SLUCM	0.18	2.7	17.7	21.7	0.50	8.4	80.1	108.9
	BEP	0.11	6.7	20.8	28.3	0.55	19.1	73.0	102.7
	BEM	0.16	10.8	20.8	28.3	0.79	36.2	77.4	105.3

MBE, MAE, and RMSE have the same units as the variable ($W\ m^{-2}$), while R is dimensionless.

drag is represented under stronger convective conditions. Overall, however, both schemes yield magnitudes close to observations, suggesting that bulk roughness parameterizations can capture the first-order mechanical forcing in dense urban areas. In contrast, the multi-layer urban schemes BEP and BEM systematically overestimate u_* at JUS in both seasons. This overestimation is evident throughout the diurnal cycle and is modulated by daytime instability, reflecting the explicit representation of building-induced drag and enhanced momentum absorption within the urban canopy. BEM produces slightly higher u_* than BEP. These results indicate that while BEP and BEM more explicitly account for urban morphology, they may over-enhance mechanical turbulence in densely built environments. This enhanced u_* likely contributes to the HFX overestimation discussed above by increasing turbulent heat exchange efficiency, and may be further amplified by an overestimation of the effective roughness length, as the tower footprint corresponds to a more homogeneous urban fabric than represented at the model grid scale. The unusually high u_* values in BEP and BEM are primarily mechanically driven, with buoyancy-driven contributions playing a secondary role at dense urban sites like JUS.

At the suburban site SIRTA, all urban physics configurations produce very similar diurnal cycles and magnitudes of u_*, in good agreement with observations (Figures 5c and 5d). The differences between schemes are small in both winter and summer, reflecting the reduced influence of complex urban morphology and the greater dominance of vegetated surfaces and open terrain. In this transitional environment, surface roughness is less sensitive to the choice of urban parameterization, and mechanical turbulence is adequately represented by all configurations.

https://doi.org/10.5194/egusphere-2026-2109
Preprint. Discussion started: 1 July 2026

To complement the site-specific diurnal analysis, Table 4 summarizes the statistical performance of u_* across all available observation sites during daytime periods. In both winter and summer, the No_URB and SLUCM configurations exhibit the strongest overall agreement with observations, characterized by higher correlation coefficients and relatively small biases and error statistics. This behavior confirms the diurnal cycle results, indicating that simplified urban representations reproduce the magnitude of mechanically driven momentum exchange reasonably well, despite their limited explicit treatment of urban morphology. Minor seasonal differences are evident, with near neutral to slightly negative biases in winter and modest positive biases in summer, consistent with seasonal variations in atmospheric stability and surface atmosphere coupling. In contrast, the multi-layer urban schemes BEP and BEM show systematically reduced correlations and substantially larger positive biases in both seasons. These statistical characteristics reflect the persistent overestimation of u_* identified in the diurnal cycles at dense urban sites, driven by the explicit representation of building induced drag and enhanced momentum exchange within the urban canopy. Among the multi-layer schemes, BEM consistently exhibits the strongest overestimation and largest error statistics in both winter and summer, indicating that the combined effects of building drag, vertical canopy structure, and building-atmosphere interactions lead to excessive surface drag and momentum transfer. BEP also overestimates u_*, but to a lesser extent, suggesting a more moderate enhancement of urban roughness effects. When aggregated across the observational network, these systematic biases dominate the error statistics, resulting in larger MAE and RMSE for BEP and especially for BEM compared to simpler urban representations.

Overall, the statistical results reinforce the diurnal cycle interpretation that u_* is highly sensitive to the treatment of urban roughness in dense urban areas, while remaining comparatively insensitive in suburban environments. Simplified schemes capture the bulk mechanical forcing with reasonable accuracy, whereas multi-layer schemes tend to over-enhance momentum exchange. These differences suggest potential implications for TKE production, the representation of boundary layer processes and tracer transport in urban environments, which are examined in the following sections.

To assess the impact of urban representation on turbulent energy, we compare TKE simulated by WRF using No_URB, SLUCM, BEP, and BEM schemes (Figure 6), highlighting how differences in urban morphology, surface forcing, and momentum exchange influence turbulence generation in both dense urban and suburban environments.

At the dense urban site JUS, the behavior of TKE differs from that of u_*. In winter (Figure 6a), BEP and BEM reproduce the magnitude and diurnal evolution of TKE reasonably well, despite overestimating HFX and u_*. This apparent paradox reflects the fact that TKE integrates multiple production mechanisms and does not respond linearly to individual surface fluxes. Enhanced building-induced drag and surface heating in multi-layer schemes increase mechanical and buoyancy-driven turbulence production, but this does not result in proportionally larger TKE. These effects suggest that enhanced mechanical and buoyancy-driven turbulence production in the multi-layer schemes is balanced by other unresolved or parameterized processes within the urban canopy and roughness sublayer, potentially including increased turbulent dissipation, leading to a net TKE magnitude close to observations. In contrast, No_URB and SLUCM substantially underestimate TKE, reflecting their weaker surface forcing and limited treatment of urban roughness, which restricts both buoyancy-driven and mechanically induced turbulence within the urban canopy.

https://doi.org/10.5194/egusphere-2026-2109
Preprint. Discussion started: 1 July 2026

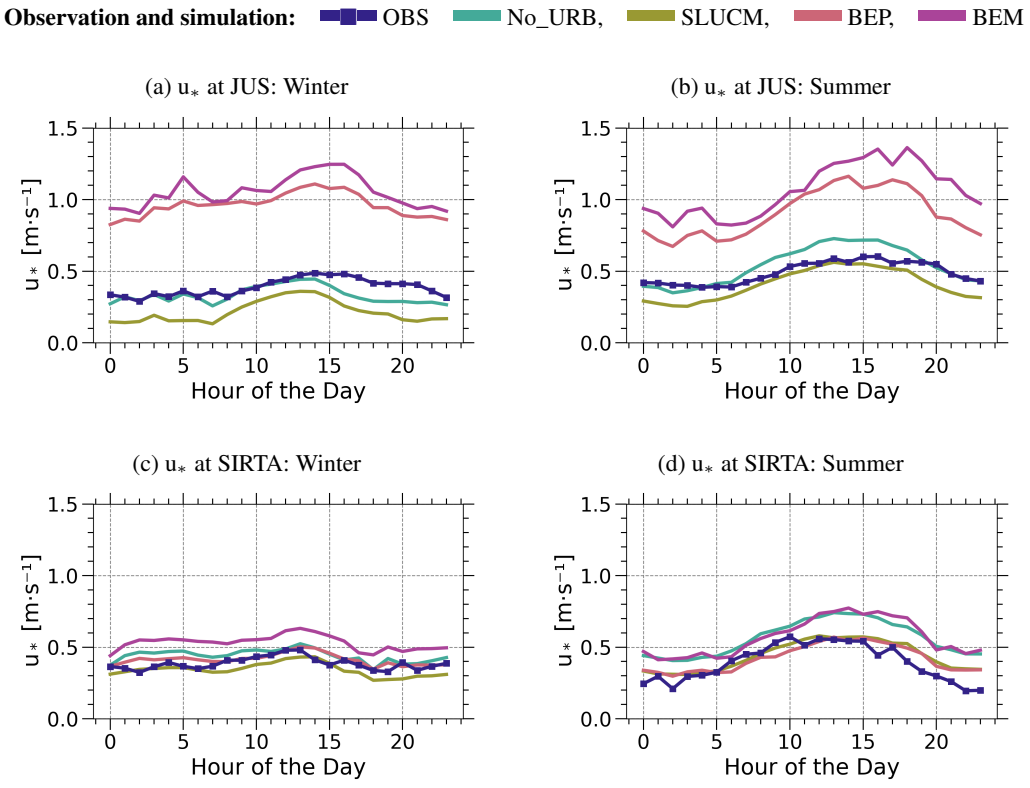

Figure 5. Same as Figure 3, but for friction velocity (u_*).

During summer, the diurnal pattern at JUS is broadly similar, but both BEP and BEM slightly underestimate TKE relative to observations, while No_URB and SLUCM follow the timing of the multi-layer schemes yet remain further below observed values (Figure 6b). This seasonal shift is consistent with stronger convective instability and enhanced HFX in summer, which promote buoyancy-driven turbulence throughout the boundary layer. Under these conditions, near-surface TKE becomes less directly controlled by local mechanical production associated with surface roughness and urban canopy drag. In multi-layer schemes, the enhanced buoyant forcing leads to more efficient vertical transport and redistribution of turbulence, so that a larger fraction of TKE is generated and maintained aloft within the mixed layer. As a result, near-surface TKE can be slightly underestimated despite realistic representations of urban morphology and surface fluxes.

The seasonal difference between winter and summer can be attributed to the deeper summer PBL: in winter, the mixed layer is shallow and surface-layer turbulence dominates, whereas in summer, enhanced buoyancy and a taller PBL redistribute TKE aloft, so near-surface TKE may appear slightly underestimated despite realistic surface fluxes and urban morphology.

At the suburban SIRTA site, all urban physics schemes capture a broadly similar diurnal evolution with only slight differences among them (Figures 6c and 6d). However, all configurations systematically underestimate TKE relative to observations. This bias occurs despite broadly realistic u_* and an enhanced HFX, accompanied by a systematic underestimation of LH in both

https://doi.org/10.5194/egusphere-2026-2109
Preprint. Discussion started: 1 July 2026

seasons. The resulting imbalance in surface energy partitioning may limit the efficiency of turbulence generation, particularly through reduced buoyancy contributions associated with moisture driven processes. In addition, this behavior points to limitations in the model representation of turbulence production, vertical transport, or dissipation under suburban conditions, where surface heterogeneity, vegetation-atmosphere interactions, and intermittent turbulent events likely play an important role. Consequently, even with strong sensible heat forcing, simulated near surface turbulence intensity remains lower than observed.

Although modeled HFX is larger than observed, near-surface TKE remains underestimated. This is likely due to a combination of factors: turbulence is redistributed in the relatively deep PBL at SIRTA (analogous to summer conditions at JUS), and suburban heterogeneity, vegetation interactions, and intermittent turbulent events are not fully captured in the model. Additionally, the systematic underestimation of LH may limit moisture-driven turbulence, so the enhanced sensible heat flux alone does not fully translate into higher near-surface TKE.

Beyond the site-specific analysis, Table 4 provides an overview of the statistical performance of TKE aggregated over all daytime observation periods. All configurations exhibit moderate correlations for TKE in both winter and summer, accompanied by consistently negative biases, consistent with the underestimation of turbulence intensity discussed above. Simplified schemes (No_URB and SLUCM) show larger negative biases and higher error metrics, particularly during winter, whereas the multi-layer schemes (BEP and BEM) substantially reduce bias and errors, likely reflecting a more realistic representation of urban morphology and turbulence generation in dense urban environments. During summer, correlations and error statistics across all schemes become more similar, suggesting that enhanced convective forcing partially offsets structural differences among urban representations. Although multi-layer schemes continue to perform comparably or slightly better than simplified approaches, all configurations retain a notable negative bias, highlighting persistent challenges in simulating TKE under strongly convective conditions. Overall, these statistics reinforce the diurnal cycle interpretation and demonstrate the strong sensitivity of TKE to urban morphology and surface energy fluxes, particularly in densely built areas.

Overall, these results demonstrate the coupled nature of surface energy fluxes, u_*, and TKE. In dense urban areas, overestimation of HFX and u_* in BEM and BEP leads to enhanced mechanical and buoyancy-driven turbulence that brings TKE closer to observed values. In contrast, simplified schemes systematically underestimate both surface forcing and turbulence. In suburban environments, the smaller-scale surface heterogeneity limits turbulence generation, so differences between urban physics schemes are reduced. These dynamics highlight the potential influence of urban physics, surface heat fluxes, u_*, and TKE on boundary-layer development and near-surface CO_2 mixing ratios, which will be examined in the subsequent section.

3.3 Impact of urban physics on boundary layer development

The influence of urban physics on boundary layer development is examined using the PBLH, based on the same set of four simulations (No_URB, SLUCM, BEP, and BEM) conducted at 900 m horizontal resolution. Differences in the representation of urban processes in WRF strongly influence the simulated PBLH, through modifications of surface energy fluxes and turbulence associated with urban roughness. The analysis evaluates how these differences affect boundary layer growth and structure, with results examined for both winter and summer periods.

https://doi.org/10.5194/egusphere-2026-2109
Preprint. Discussion started: 1 July 2026

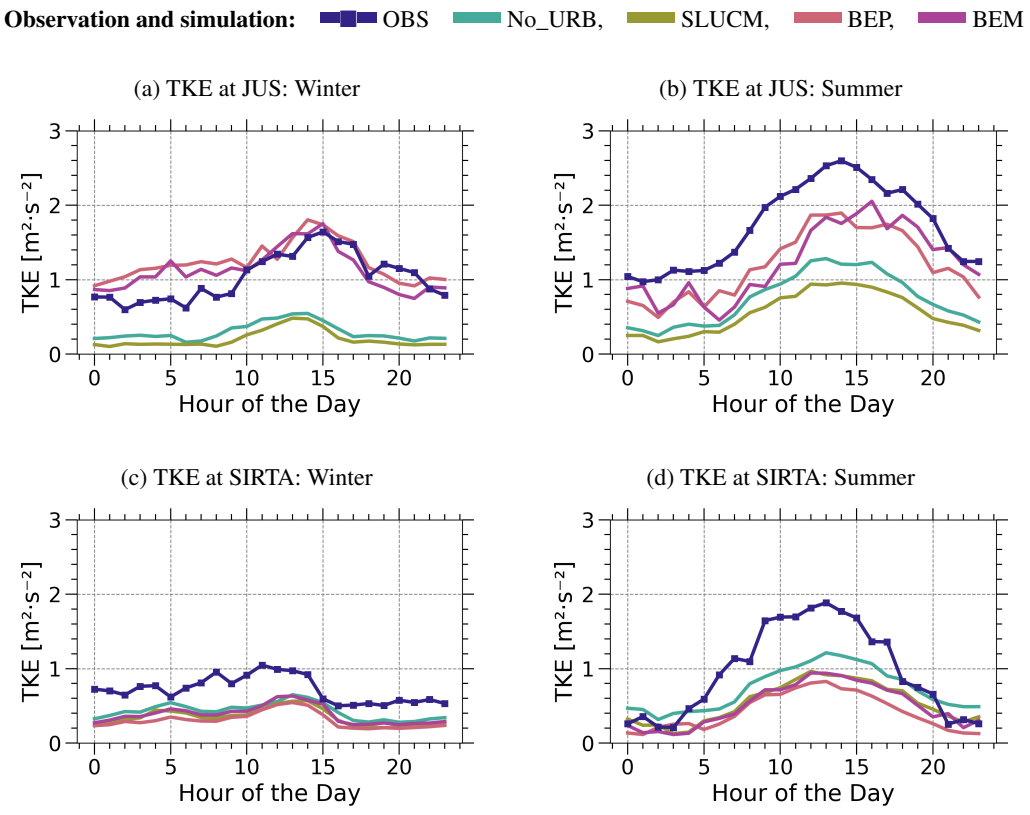

Figure 6. Same as Figure 3, but for turbulent kinetic energy (TKE)

The diurnal cycle of the PBLH is first examined to assess how urban physics influence the daytime growth and evolution of the boundary layer through their integrated response to surface heat fluxes and urban-induced turbulence.

At the dense urban site Qualair (Paris), pronounced differences in the diurnal evolution of PBLH are observed among the urban physics schemes, particularly in winter. During daytime, No_URB and SLUCM substantially underestimate PBLH, reflecting their limited representation of urban roughness and surface–atmosphere coupling, which leads to weaker turbulent mixing. In contrast, the multi-layer schemes BEP and BEM capture the diurnal evolution of PBLH but tend to overestimate it relative to observations, with BEP showing a larger bias than BEM (Figure 7c). This behavior is consistent with enhanced daytime HFX, combined with high u_* and slightly overestimated TKE, which together support stronger buoyancy and mechanically driven boundary-layer growth. At night, however, BEP and BEM exhibit larger deviations from observations than during daytime, likely reflecting differences in the representation of urban heat storage release and nocturnal turbulence within the urban canopy.

In summer at Qualair, all urban schemes exhibit a broadly similar diurnal evolution, with boundary-layer growth beginning in the early morning in phase with observations (Figure 7d). However, notable discrepancies appear during the mature convective period. While observations show a continuous increase in PBLH from mid-morning until late afternoon, maintaining a maximum

https://doi.org/10.5194/egusphere-2026-2109
Preprint. Discussion started: 1 July 2026

Table 4. Statistical evaluation of surface u_* and TKE simulated by WRF at 900 m resolution for winter (10-31 January) and summer (01-20 June) periods. Data are averaged over the active daytime period (10–16 UTC in winter and 09–18 UTC in summer. Results are shown for four urban physics configurations: No_URB, SLUCM, BEP, and BEM. Statistics include the correlation coefficient (R), mean bias error (MBE), mean absolute error (MAE) and root mean square error (RMSE) and are computed across all available observation sites.

		Winter (January)				**Summer (June)**			
Variable	**Scheme**	R	MBE	MAE	RMSE	R	MBE	MAE	RMSE
u_* ($m\ s^{-1}$)	No_URB	0.65	0.00	0.13	0.17	0.60	0.10	0.17	0.21
	SLUCM	0.62	-0.04	0.13	0.17	0.53	-0.01	0.15	0.20
	BEP	0.51	0.15	0.23	0.33	0.49	0.10	0.21	0.29
	BEM	0.51	0.19	0.26	0.40	0.45	0.18	0.26	0.36
TKE ($m^2\ s^{-2}$)	No_URB	0.58	-0.61	0.65	0.89	0.56	-0.82	0.89	1.14
	SLUCM	0.52	-0.65	0.68	0.94	0.53	-1.02	1.05	1.31
	BEP	0.60	-0.36	0.51	0.74	0.51	-0.96	1.02	1.27
	BEM	0.60	-0.36	0.52	0.76	0.56	-0.90	0.97	1.20

MBE, MAE, and RMSE are expressed in the same units as the corresponding variable: u_* in $m\ s^{-1}$ and TKE in $m^2\ s^{-2}$, while R is dimensionless.

of about 1.5–1.6 km until around 18 UTC, all model schemes exhibit a similar evolution with an earlier peak around 13 UTC but followed directly by a gradual decline. This decrease should be interpreted with caution, as it largely reflects temporal averaging rather than the actual boundary layer dynamics, in reality, the decay of turbulence and the transition to a stable nocturnal boundary layer occur more abruptly. In addition, the diagnosed timing of the evening transition may be affected by uncertainties in the PBLH retrieval method. Among the models, BEM follows the observed trend most closely, but the earlier transition leads to an apparent underestimation of PBLH during the late afternoon and evening period. This interpretation is consistent with the summer TKE results, which show that even multi-layer schemes (BEP and BEM) slightly underestimate near-surface TKE, while simpler schemes (No_URB and SLUCM) exhibit a stronger TKE deficit despite comparable u_*.

At the suburban site Palaiseau, scheme to scheme differences in PBLH are generally smaller, reflecting the reduced influence of urban morphology on boundary-layer dynamics. In winter, all schemes underestimate daytime PBLH, with the strongest negative bias in No_URB and SLUCM and smaller discrepancies in BEP and BEM, while nighttime PBLH is comparatively well captured by all configurations, indicating limited sensitivity to urban physics under stable conditions. This behavior is consistent with the suburban surface energy and momentum budgets, where HFX and u_* are well reproduced across schemes, and turbulent kinetic energy is systematically underestimated but shows little sensitivity to the choice of urban physics. In addition, the winter wind regime is characterized by mixed and variable directions (Figure F1), limiting persistent advection of urban air masses from Paris toward SIRTA. Nevertheless, even these relatively modest differences in PBLH (on the order of tens

https://doi.org/10.5194/egusphere-2026-2109
Preprint. Discussion started: 1 July 2026

of meters) may still influence near-surface CO_2 mixing ratios by modifying the effective mixing volume, particularly under weak-wind conditions or during periods of sustained emissions.

During summer at Palaiseau, all schemes reproduce a similar diurnal evolution but systematically underestimate PBLH throughout most of the day. Agreement with observations is limited to the early morning growth phase between 06 and 10 UTC. After this period, modeled PBLH continues to increase moderately, reaching a maximum of about 1.2 km around 14 UTC before starting to decrease, while the observations continue to increase to approximately 1.4 km and maintain this higher PBLH until later in the afternoon. This apparent evolution likely reflects temporal averaging, as the evening transition is abrupt and not well captured by averaged PBLH diagnostics. As at the urban site, this discrepancy points to limitations in representing sustained convective growth rather than deficiencies in surface forcing alone, consistent with the underestimation of TKE despite a slightly higher HFX and realistic u_*. In addition, the summer period is characterized by frequent northerly to northeasterly winds in the observations (Figure F2), which tend to place the Palaiseau (SIRTA) site downwind of the Paris urban area. Under such conditions, advection of urban air masses can enhance boundary layer development and may contribute to the higher observed PBLH compared to the simulations. However, the wind rose analysis also reveals discrepancies between observations and the model at SIRTA, where observed winds are more frequently easterly, while the model favors northwesterly directions. This directional bias likely limits the model's ability to reproduce the advection of urban air masses, and thus contributes to the underestimation of PBLH. Although convection is explicitly resolved at kilometer-scale resolution and cumulus parameterizations are switched off, the grid may not fully capture deep convective plumes, which can further lead to underestimation of PBL growth and vertical mixing in summer.

The pronounced nighttime underestimation of PBLH at Palaiseau, with modeled values around 200–250 m compared to observed heights near 500 m, occurs despite comparable TKE and overestimated u_*, indicating that the issue is not a lack of turbulence intensity but rather its vertical distribution. Under stable conditions over suburban terrain, the model likely confines turbulence too close to the surface and underestimates non-local and intermittent mixing processes, leading to insufficient coupling with the residual layer and an excessively shallow nocturnal boundary layer.

Table 5 summarizes the statistical performance of the different urban configurations in simulating daytime PBLH during winter and summer, complementing the diurnal cycle analysis with quantitative measures of correlation and error.

In winter, all configurations exhibit moderate correlations with observed PBLH ($R \approx 0.56$–0.64), but systematic differences in bias and error magnitude are evident. The No_URB and SLUCM simulations consistently underestimate PBLH, reflecting suppressed daytime boundary layer growth associated with weak surface buoyancy forcing and limited turbulent mixing. SLUCM shows slightly larger negative bias and error statistics than No_URB, indicating that the simplified canyon representation does not substantially improve wintertime boundary layer development. In contrast, BEP tends to overestimate PBLH, resulting in the largest MAE and RMSE among the schemes, consistent with excessive buoyancy driven mixing associated with enhanced sensible heat flux. The BEM configuration provides the most balanced winter performance, combining the highest correlation with minimal systematic bias and the lowest error statistics. This improved performance of BEM compared to BEP likely reflects the inclusion of building thermal inertia and indoor–outdoor energy exchanges, which buffer surface heating and reduce excessive HFX, thereby limiting overactive buoyancy-driven mixing and leading to more realistic boundary layer growth. This

https://doi.org/10.5194/egusphere-2026-2109
Preprint. Discussion started: 1 July 2026

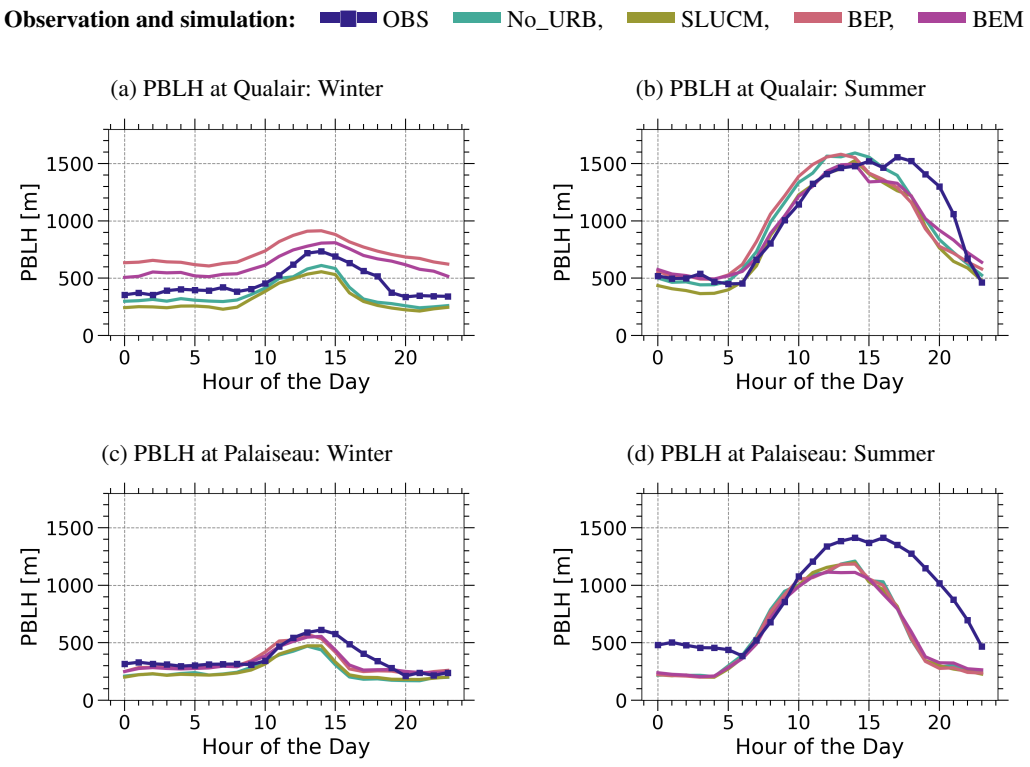

Figure 7. Diurnal cycles of PBLH comparing observations with WRF simulations at 900 m horizontal resolution for different urban physics schemes. PBLH is diagnosed using the bulk Richardson number for all runs. Panels (a) and (b) show winter (10–31 January 2024) and summer (01–20 June 2024) conditions, respectively, at the urban core site Qualair. Panels (c) and (d) show winter and summer conditions, respectively, at the suburban site Palaiseau.

indicates a more realistic representation of surface energy partitioning and turbulent mixing that supports boundary layer growth without excessive deepening.

In summer, all urban configurations systematically underestimate PBLH, with substantially larger biases and errors compared to winter and only small differences among schemes. Correlation coefficients are similar across all configurations ($R \approx 0.53$–0.59), and the magnitude of underestimation exceeds 150 m for all cases. These results indicate that, despite stronger surface forcing and enhanced turbulence during summer, none of the urban schemes is able to adequately reproduce observed daytime boundary layer depths. The convergence of error statistics across schemes suggests a common limitation in the representation of convective boundary layer growth, likely related to processes such as entrainment at the PBL top and incomplete representation of 3D convective turbulence. At kilometer-scale resolution, explicit convection is only partially resolved (the "gray-zone"), which can limit full vertical mixing. This interpretation is consistent with the summer TKE results, which show persistent underestimation of turbulent energy near the surface, limiting the model's ability to sustain vertical mixing and boundary layer deepening under strongly convective conditions.

https://doi.org/10.5194/egusphere-2026-2109
Preprint. Discussion started: 1 July 2026

Table 5. Statistical evaluation of PBLH simulated by WRF at 900 m resolution for winter (10-31 January) and summer (01-20 June) periods. Data are averaged over the active daytime period (10–17 UTC in winter and 10–19 UTC in summer. Results are shown for four urban physics configurations: No_URB, SLUCM, BEP, and BEM. Statistics include the correlation coefficient (R), mean bias error (MBE), mean absolute error (MAE) and root mean square error (RMSE). Winter statistics are computed across all available observation sites, whereas summer statistics are limited to the Qualair and Palaiseau sites due to data availability.

		Winter (January)				**Summer (June)**			
Variable	**Scheme**	R	MBE	MAE	RMSE	R	MBE	MAE	RMSE
PBLH (m)	No_URB	0.63	-134	229	305	0.54	-146	332	445
	SLUCM	0.61	-150	249	321	0.57	-204	330	447
	BEP	0.56	83	253	345	0.53	-167	343	461
	BEM	0.64	27	212	286	0.59	-209	333	455

MBE, MAE, and RMSE have the same units as the variable (m), while R is dimensionless

The PBLH results highlight the tight coupling between urban surface energy partitioning, turbulence generation, and boundary layer development. Multi-layer urban schemes enhance the representation of daytime boundary layer growth in dense urban environments, particularly in winter, by strengthening both buoyancy and mechanically driven turbulence. In contrast, during summer, all configurations exhibit a tendency toward premature boundary layer saturation, pointing to shared limitations in the representation of convective mixing and entrainment at the PBL top. This tendency toward premature boundary layer saturation in summer is also consistent with the observed nighttime underestimation of PBLH at Palaiseau. Consequently, although urban physics strongly modulate surface energy partitioning, their impact on summertime PBLH remains constrained by these broader model limitations, leading to relatively muted differences among schemes compared to winter and prevents the models from sustaining the deep convective PBL observed in the late afternoon, despite substantial contrasts in urban representation and surface heat fluxes.

While the diurnal cycle and statistical evaluation demonstrate the sensitivity of PBLH magnitude and temporal variability to urban physics at specific sites, they provide only a partial view of how urbanization shapes the spatial structure of the boundary layer across the city. To complement this site-based analysis, we next examine a cross-urban transect of PBLH extending from rural surroundings through the urban core and back to rural conditions, allowing a direct assessment of spatial gradients associated with urban land cover.

3.4 Spatial structure of the urban boundary layer

Figure 8 illustrates the wintertime spatial structure of the planetary boundary layer height (PBLH) along a transect extending from rural areas outside Paris, across the urban core, and back into rural surroundings. The left panel shows the geographical location of the transect and the PBLH observational stations intersected by it, while the right panel presents observed PBLH

https://doi.org/10.5194/egusphere-2026-2109
Preprint. Discussion started: 1 July 2026

at the station locations together with PBLH simulated by the different WRF configurations sampled continuously along the transect.

Consistent with the winter diurnal cycles and statistical evaluation, the No_URB and SLUCM configurations exhibit only weak enhancement of PBLH over the urban area, remaining close to rural background values. This muted urban signal reflects their limited representation of urban surface forcing and reduced buoyancy driven and mechanical turbulence, which leads to the systematic underestimation of daytime PBLH identified earlier. In contrast, the BEP configuration produces a pronounced and spatially extensive urban PBLH maximum, forming a broad "urban dome" over the city. This behavior is consistent with the slight overestimation of daytime PBLH seen in the statistical analysis and reflects excessive sensible heat fluxes and enhanced turbulence that drive overly vigorous boundary layer growth in winter. The BEM simulation captures a well defined but more moderate urban PBLH dome, with sharper urban–rural gradients and a realistic transition back to rural conditions on either side of the city. This spatial pattern aligns with the diurnal cycle and statistical results, which showed that BEM provides the most balanced representation of wintertime surface forcing and turbulence, yielding PBLH magnitudes and variability closest to observations. Overall, the transect analysis complements the site-based diagnostics by demonstrating how differences in urban physics not only affect the temporal evolution of PBLH but also control the horizontal extent and intensity of the wintertime urban boundary layer.

3.5 Impact of urban physics on near-surface and boundary layer meteorology

Near-surface meteorological variables, including air temperature, relative humidity, wind speed, and wind direction, are evaluated over the full diurnal cycle to assess model performance across the four urban physics configurations (No_URB, SLUCM, BEP, and BEM) for both winter and summer periods. In contrast to surface heat fluxes and PBLH, which are evaluated during daytime hours to focus on periods of active turbulence and boundary layer development, near-surface meteorological variables are evaluated over the full diurnal cycle. This approach captures both daytime and nighttime conditions and allows a comprehensive assessment of model performance under a wide range of stability regimes, while maintaining consistency with the analyses of CO_2 mixing ratios, surface energy fluxes, and boundary-layer height.

Temperature is well represented across all schemes in both winter and summer, with minor cold biases in simpler configurations (No_URB, SLUCM) during winter and slight warm biases in the multi-layer schemes (BEP, BEM), reflecting the impact of detailed urban representations on heat retention and local warming. These small temperature biases are consistent with the overestimation of daytime HFX in BEP and BEM (Table 3). In dense urban areas, this may reflect the combined effects of enhanced urban heat storage and detailed canopy representation in the multi-layer schemes, which can lead to slightly higher near-surface temperatures.

For relative humidity, although the mean absolute errors are comparable across urban physics schemes, the sign of the humidity bias shows a seasonal consistency with the simulated latent heat flux. In winter, LH biases remain small for all schemes: near-neutral for No_URB (4.5 W m^{-2}) and SLUCM (2.7 W m^{-2}), slightly positive in BEP (6.7 W m^{-2}), and modestly positive in BEM (10.8 W m^{-2}) (Table 3). Consequently, differences in near-surface humidity are limited, indicating that wintertime relative humidity is only weakly sensitive to urban physics through latent heat exchange. In summer, LH biases diverge more

https://doi.org/10.5194/egusphere-2026-2109
Preprint. Discussion started: 1 July 2026

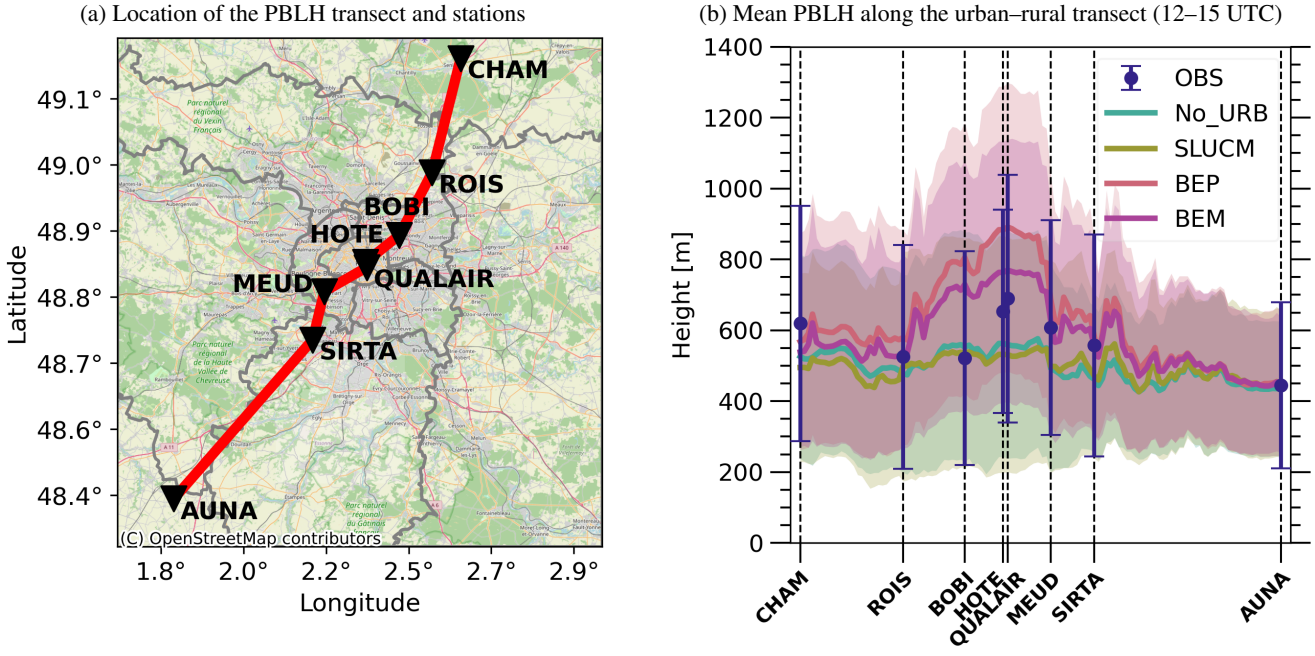

Figure 8. Spatial variation of planetary boundary layer height (PBLH) across the Paris metropolitan area during winter. (a) Map showing the location of the transect crossing rural areas outside Paris, the urban core, and rural areas on the opposite side, together with the PBLH observational stations intersected by the transect (Looschelders and et al., 2026, in prep; to be updated with the preprint citation). (b) Mean PBLH along the transect averaged between 12:00 and 15:00 UTC, corresponding to the period of maximum boundary layer development, showing observed PBLH at station locations and WRF-simulated PBLH sampled continuously along the transect for the different urban physics configurations. Shaded area and bars represent standard deviation.

noticeably among schemes, as shown in Table 3: No_URB substantially underestimates LH, SLUCM shows a small positive bias, BEP exhibits a moderate positive bias, and BEM has the largest positive bias. These differences in LH translate into near-surface humidity variations, with No_URB producing slightly drier conditions and the multi-layer urban schemes generating a modest moist bias. Overall, the relatively small spread in relative humidity across schemes reflects the secondary role of urban physics in controlling near-surface moisture, compared to its stronger influence on surface energy partitioning and turbulent mixing.

Near-surface wind speed and direction show limited sensitivity to the choice of urban scheme. Multi-layer configurations (BEP, BEM), despite producing higher friction velocities (Table 4), do not substantially alter near-surface winds compared to observations. Among the schemes, BEP and BEM show slightly better performance in both wind speed and direction during winter, with marginally higher correlations and lower RMSE.

While differences among urban schemes are modest in near-surface wind statistics, vertical profiles of wind speed and direction reveal a clearer sensitivity to urban physics within the lowest few hundred meters of the atmosphere, where urban canopy effects and surface driven turbulence exert the strongest influence. These profiles, evaluated against Doppler lidar

https://doi.org/10.5194/egusphere-2026-2109
Preprint. Discussion started: 1 July 2026

observations at four sites, during winter, provide insight into the vertical distribution of momentum and the representation of urban drag and mixing processes that are not fully captured by near-surface diagnostics alone. Figure 9 shows the vertical profiles of MAE and RMSE for wind speed and wind direction during winter, computed between model simulations and lidar observations. Across all sites, the largest differences between urban schemes occur in the lowest part of the profile, particularly below 400-500 m. In this layer, multi-layer urban schemes (BEP and BEM) systematically reduce wind speed and wind direction RMSE relative to SLUCM and No_URB, with differences reaching approximately 1 m s^{-1} for wind speed. At the JUS site, wind speed RMSE values are higher for all configurations, ranging from approximately 2.4 to 3.3 m s^{-1} in the lower PBL, indicating more complex flow conditions and a stronger influence of unresolved local heterogeneity. Nevertheless, the relative ranking of urban schemes remains consistent, with BEP and BEM generally outperforming simpler schemes in the lowest levels.

Above approximately 400-500 m, differences in wind speed and wind direction MAE and RMSE among urban schemes diminish, and profiles converge toward similar values. This convergence reflects the reduced influence of urban canopy processes with height, as flow transitions from the urban roughness sublayer to the overlying mixed layer, where synoptic and mesoscale forcing dominate and urban parameterizations exert limited control. The improved representation of wind profiles by BEP and BEM in the lowest below 400-500 m is particularly relevant for urban CO_2 transport, as this layer contains the majority of anthropogenic emissions and governs near-surface ventilation and vertical dilution. Even moderate improvements in wind speed can influence CO_2 mixing ratios in this layer due to its role in transport.

Overall, the modest inter-scheme differences in near-surface temperature and humidity indicate that these variables are only weakly sensitive to the choice of urban representation, likely due in part to the relatively large model grid, which smooths surface heterogeneity; finer-scale representation could enhance sensitivity to the urban scheme. Near-surface wind speed and direction also respond to urban physics, though differences among schemes at the surface are modest (typically 0.3–0.6 m s^{-1} in RMSE) compared to the more pronounced contrasts observed in the vertical wind profiles within the lowest few hundred meters of the atmosphere during winter. Multi-layer urban schemes (BEP and BEM) generally improve the representation of vertical momentum distribution relative to simpler configurations, highlighting the height dependent influence of urban physics. The impact of urban physics on near-surface meteorology occurs primarily through its effect on surface sensible and latent heat fluxes and momentum exchange, rather than through systematic biases in the large scale and mesoscale atmospheric forcing imposed through the boundary conditions. As a result, variables such as HFX, LH, u_*, TKE, and the vertical structure of wind are more sensitive to urban canopy parameterizations than near-surface temperature and humidity. The relatively small differences in near-surface meteorology suggest that the pronounced variations observed in surface energy fluxes and boundary-layer properties arise mainly from differences in urban energy partitioning and turbulent mixing, rather than from biases in the simulated large scale atmospheric conditions.

3.6 Implications for CO_2 variation and extreme events

This section focuses on the influence of urban physics representations on near-surface CO_2 mixing ratios, considering their magnitude, diurnal cycle, and relationships with observations.

https://doi.org/10.5194/egusphere-2026-2109
Preprint. Discussion started: 1 July 2026

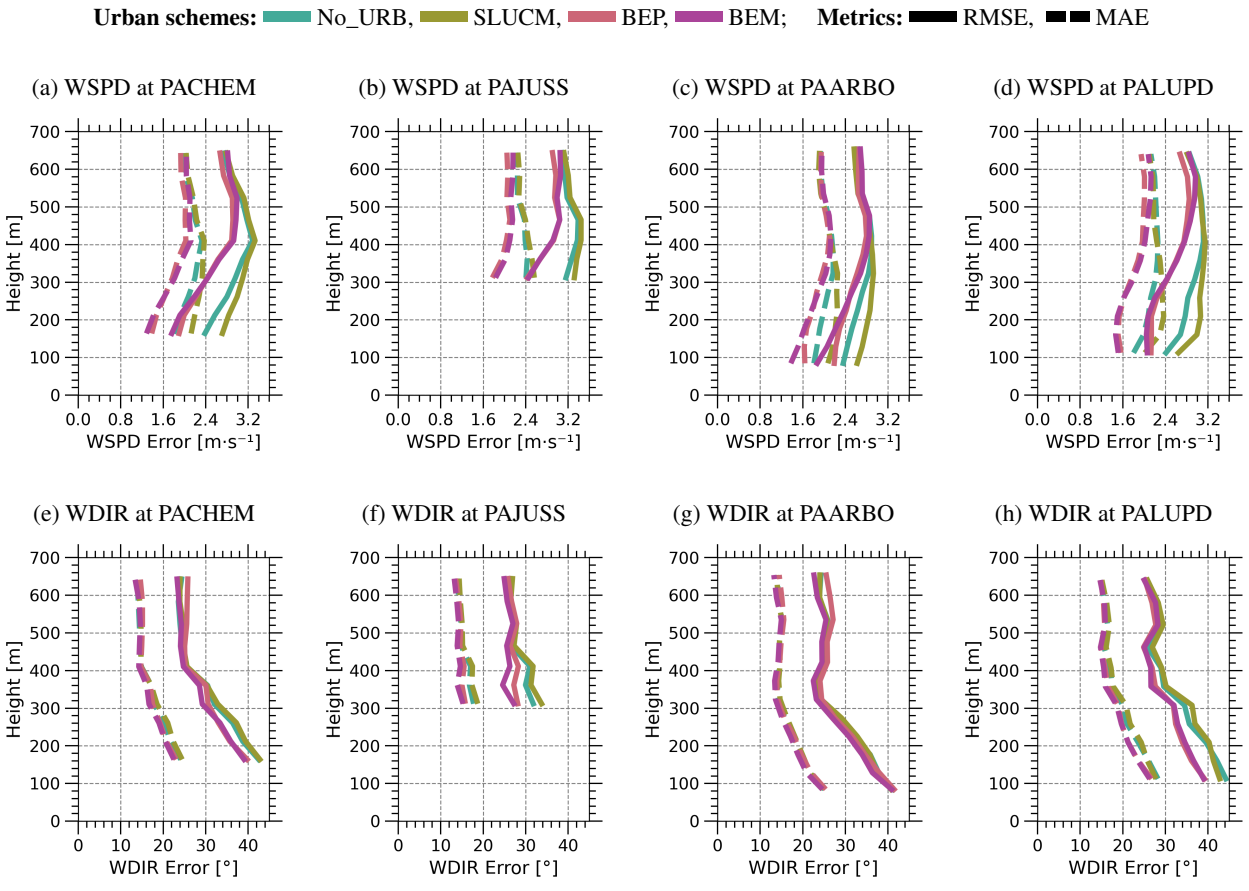

Figure 9. Vertical profiles of root mean square error (RMSE; solid lines) and mean absolute error (MAE; dashed lines) between WRF simulations and Doppler wind lidar observations for wind speed (WSPD, top row) and wind direction (WDIR, bottom row). Results are shown for four sites (PACHEM, PAJUSS, PAARBO, and PALUPD) during wintertime conditions (10–31 January 2024). All simulations were performed at 900 m horizontal resolution using different urban physics schemes. Statistics are computed over the full diurnal cycle.

https://doi.org/10.5194/egusphere-2026-2109
Preprint. Discussion started: 1 July 2026

Table 6. Statistical evaluation of near-surface meteorological variables simulated by WRF at 900 m resolution for winter (10-31 January) and summer (01-20 June) periods. Statistics are computed over the full diurnal cycle. Results are shown for four urban physics configurations: No_URB, SLUCM, BEP, and BEM. Statistics include the correlation coefficient (R), mean bias error (MBE), mean absolute error (MAE), and root mean square error (RMSE).

		Winter (January)				**Summer (June)**			
Variable	**Scheme**	R	MBE	MAE	RMSE	R	MBE	MAE	RMSE
Temperature	No_URB	0.97	-1.1	1.4	1.7	0.88	0.0	1.2	1.7
	SLUCM	0.95	-2.0	2.2	2.6	0.87	-0.4	1.4	1.8
	BEP	0.95	1.1	1.6	2.1	0.88	-0.4	1.2	1.7
	BEM	0.96	0.3	1.2	1.6	0.88	-0.7	1.3	1.8
Relative Humidity	No_URB	0.79	2.9	6.2	7.8	0.82	-3.7	7.4	9.9
	SLUCM	0.74	7.0	8.7	10.9	0.82	-2.0	7.1	9.4
	BEP	0.72	-8.9	10.0	12.4	0.82	-1.9	6.8	9.1
	BEM	0.75	-3.4	6.8	8.6	0.81	1.1	7.0	9.4
Wind Speed	No_URB	0.91	0.5	1.2	1.7	0.79	0.4	1.2	1.6
	SLUCM	0.90	0.8	1.4	1.9	0.78	0.7	1.4	1.8
	BEP	0.91	0.4	1.0	1.5	0.81	0.2	1.1	1.5
	BEM	0.92	0.0	1.0	1.4	0.80	-0.2	1.1	1.5
Wind Direction	No_URB	0.82	2.8	18.4	30.3	0.82	3.7	28.2	44.9
	SLUCM	0.82	2.2	18.9	31.2	0.82	3.2	28.2	45.0
	BEP	0.82	5.6	20.2	33.6	0.82	2.9	27.9	44.9
	BEM	0.85	3.8	18.1	30.2	0.82	2.1	27.5	44.6

Temperature is in °C, relative humidity in %, wind speed in m s^{-1}, and wind direction in degrees. Wind direction statistics are restricted to periods with wind speed exceeding 1 m s^{-1} to avoid ill-defined directions under weak wind conditions.

During winter at the urban sites JUS and EIF (Figures 10a, and 10c), clear and physically consistent differences emerge among the urban physics configurations. In line with the earlier analyses of surface energy fluxes and PBLH, the No_URB and SLUCM simulations produce systematically shallower boundary layers and weaker turbulent mixing as a consequence of underestimated sensible heat flux. These conditions favor enhanced near-surface accumulation of CO_2, allowing the model to reproduce pronounced concentration peaks, such as the event observed on 16 January. However, these apparent agreements arise from physically inconsistent processes: insufficient surface heating, weak turbulence, and suppressed boundary-layer

https://doi.org/10.5194/egusphere-2026-2109
Preprint. Discussion started: 1 July 2026

growth amplify nocturnal CO_2 trapping and can generate exaggerated or spurious peaks that are not consistently supported by observations.

In contrast, the multi-layer urban schemes (BEP and BEM) simulate more realistic CO_2 variability by explicitly accounting for urban energy exchange and turbulence. Nevertheless, the two schemes exhibit distinct behaviors linked to their surface flux and PBLH characteristics. BEP overestimates sensible heat flux and slightly over-deepens the boundary layer, enhancing vertical mixing and leading to systematic underestimation of near-surface CO_2 mixing ratios and extreme peaks. BEM provides a more balanced representation of surface energy partitioning and boundary layer development, resulting in realistic diurnal CO_2 cycles and more moderate peak magnitudes. Despite this improved physical consistency, the enhanced mixing in BEM limits the model's ability to fully reproduce the strongest accumulation events, including the 16 January peak; this underestimation likely reflects a temporary attenuation of PBLH under highly stable conditions associated with a pronounced anti-cyclone and very low wind speeds during the first half of the day, which reduces near-surface trapping and limits peak CO_2 buildup, even though overall temporal variability and background levels are well captured.

The corresponding diurnal cycles at the urban sites (Figures 11a and 11c) reinforce these conclusions. No_URB and SLUCM strongly overestimate nighttime and early morning CO_2 mixing ratios, with the largest bias in SLUCM, reflecting excessive nocturnal trapping under weak turbulent mixing. BEP underestimates CO_2 throughout most of the diurnal cycle, consistent with its overly deep boundary layer and enhanced vertical dilution. BEM reproduces the diurnal evolution most realistically, closely matching observed CO_2 variations from late morning through nighttime, with only a slight underestimation during the early morning hours. This consistency between the time series and diurnal analyses confirms that realistic urban energy partitioning and boundary layer mixing are essential for simulating wintertime CO_2 variability, even if extreme accumulation events remain difficult to capture.

At the suburban site SAC (Figure 10e), scheme to scheme differences are reduced but remain evident. Compared to the urban core, all configurations exhibit smaller CO_2 variability and weaker accumulation events, reflecting lower emission intensity and more homogeneous surface characteristics. The No_URB and SLUCM simulations still tend to produce episodic overestimations of near-surface CO_2, although with substantially smaller amplitudes than at the urban sites. As in the city center, these overestimations are linked to weaker turbulent mixing and shallower boundary layers, but their impact is muted under suburban conditions. The BEP and BEM schemes produce smoother and more realistic CO_2 time series at SAC, with limited differences between the two configurations. This convergence is consistent with the reduced sensitivity of suburban turbulence intensity and boundary-layer structure to urban physics, as previously documented for sensible heat flux, friction velocity, and TKE at this site. Unlike in the urban core, neither BEP nor BEM exhibits pronounced underestimation of background CO_2 levels, indicating a more balanced representation of mixing relative to emission strength.

The suburban diurnal cycles (Figure 11e) further highlight this contrast with the urban sites. No_URB and SLUCM reproduce the observed diurnal amplitude more closely; however, this apparent agreement partly reflects a compensation effect, as episodic nighttime overestimations evident in the time series are smoothed out in the diurnal averaging. BEP and BEM show a modest negative bias throughout the cycle, but the magnitude of this underestimation remains small (on the order of a few ppmv), substantially lower than in the urban core where stronger emissions amplify the effects of enhanced vertical mixing in BEP and,

https://doi.org/10.5194/egusphere-2026-2109
Preprint. Discussion started: 1 July 2026

to a lesser extent, BEM. This difference underscores the role of emission intensity in modulating the CO_2 response to boundary layer dynamics: under suburban conditions, even schemes that promote stronger mixing do not strongly suppress near-surface CO_2 mixing ratios.

Overall, the wintertime time series and diurnal cycle analyses highlight a key implication for urban CO_2 modeling: apparent agreement with observed extreme concentrations does not necessarily imply physically realistic behavior. Configurations lacking detailed urban physics (No_URB and SLUCM) can reproduce large CO_2 peaks through artificially suppressed turbulent mixing and shallow boundary layers, leading to excessive near-surface accumulation for the wrong physical reasons. In contrast, physically consistent schemes, particularly BEM provide a more robust representation of background concentrations and diurnal variability by realistically coupling surface energy fluxes, boundary layer development, and turbulence. Although such schemes may partially underestimate the most extreme accumulation events, they better capture the underlying processes governing CO_2 variability. These results confirm that wintertime near-surface CO_2 mixing ratios are primarily controlled by urban induced modifications of sensible heat flux, turbulence intensity, and boundary layer structure.

During summer at both urban (JUS and EIF) and suburban (SAC) sites (Figures 10b, 10d, and 10f), all urban physics configurations exhibit very similar temporal evolution and magnitudes of near-surface CO_2 mixing ratios. Compared to winter, scheme to scheme differences are strongly reduced, indicating a convergence in the effective boundary-layer control on CO_2 variability. This behavior is consistent with the summer PBLH analysis, which shows that all schemes reproduce the onset of morning boundary-layer growth but systematically underestimate its continued deepening during the mature convective period. Despite persistent differences in surface heat fluxes, friction velocity, and near-surface turbulence intensity, the simulated boundary layer structure converges toward a common shallow daytime plateau, reducing the sensitivity of near-surface CO_2 mixing ratios to the choice of urban physics during summer. All configurations tend to underestimate nighttime and early morning CO_2 peaks, particularly during prolonged accumulation events. This behavior is not primarily driven by PBLH, which remains shallow at night in both observations and simulations, but rather by insufficient stabilization of the near-surface atmosphere. Slightly elevated friction velocity limits the development of strongly stable conditions, while near-surface TKE, although underestimated, does not fully collapse, allowing some mechanical mixing to persist. As a result, nocturnal CO_2 trapping is weaker than observed across all schemes, including BEP and BEM.

The diurnal cycles (Figures 11b, 11d and 11f) further clarify the mechanisms controlling summertime CO_2 variability. During daytime, simulated CO_2 mixing ratios are generally well reproduced, particularly during the morning transition when boundary layer growth and turbulent mixing are most active. At the suburban site SAC, this convergence among schemes is even more pronounced: all configurations display nearly identical CO_2 variability. Although all WRF configurations simulate a similar PBLH evolution, with a maximum reached around 13–14 UTC followed by a gradual decrease, observed CO_2 mixing ratios are already in a declining phase during this period. This indicates that a deep PBLH does not necessarily imply a fully mixed layer: turbulence decays gradually. Consequently, the earlier peak and subsequent decrease in modeled PBLH do not prevent the model from capturing the daytime CO_2 decline, as surface emissions are effectively diluted by ongoing vertical mixing and the expansion of the mixed-layer volume. The daytime decrease in CO_2 is therefore governed by the combined effects of boundary layer growth and sustained turbulent mixing, which, despite being underestimated in magnitude, remains

https://doi.org/10.5194/egusphere-2026-2109
Preprint. Discussion started: 1 July 2026

sufficient to dilute surface emissions. This explains why the model reproduces the general daytime CO_2 evolution despite systematic underestimation of afternoon PBLH, slight overestimation of friction velocity in some schemes, and underestimation of near-surface TKE. In summer, strong convective forcing dominates CO_2 variability, constraining the influence of urban physics on near-surface concentrations.

Overall, the summer CO_2 results indicate that near-surface concentrations become weakly sensitive to urban physics not because mixing is fully realistic, but because all schemes share similar limitations in representing sustained convective boundary layer deepening especially into the late afternoon. Under these conditions, differences in surface energy partitioning and urban complexity are largely masked, leading to convergent CO_2 behavior across configurations despite persistent biases in boundary layer structure. During summer nights, all configurations tend to underestimate CO_2 peaks, particularly during prolonged accumulation periods. This behavior reflects insufficient stabilization of the near-surface atmosphere: slightly elevated friction velocity and non-zero TKE prevent the full collapse of turbulence, reducing nocturnal trapping and allowing some mechanical mixing to persist. As a result, nighttime CO_2 accumulation is weaker than observed, highlighting a limitation common to all urban physics schemes during summer nocturnal periods.

After examining the time series and diurnal cycles, Figure 12 provides a statistical summary of daytime (11–16 UTC in winter and 10–18 UTC in summer) near-surface CO_2 mixing ratios, illustrating network-wide metrics that reveal how differences in urban driven boundary-layer mixing propagate into CO_2 mixing ratio biases. For both seasons, model–observation agreement is systematically higher for the Picarro network compared to the Mid-cost sensors. This is likely related to differences in measurement accuracy, stability, and noise characteristics between the two instrument types, rather than to differences in station siting, local flow conditions, or the atmospheric representativeness of the measurements.

During winter daytime conditions, the CO_2 evaluation reveals a strong sensitivity of near-surface concentrations to the choice of urban physics, reflecting differences in vertical mixing rather than in background meteorology or emissions (Figures 12a and 12c). Configurations without explicit urban representation (No_URB) systematically overestimate near-surface CO_2, consistent with their weak sensible heat fluxes, shallow boundary layers, and reduced turbulence intensity. These conditions limit both buoyancy and mechanically driven mixing, favoring the accumulation of surface emissions within a shallow mixing layer.

The single-layer urban canopy model (SLUCM) further exacerbates this behavior. Despite introducing an urban parameterization, its simplified representation of canyon processes does not sufficiently enhance turbulent exchange or boundary layer growth. As a result, SLUCM produces the largest CO_2 overestimations and the weakest agreement with observations, consistent with its suppressed PBLH and limited enhancement of friction velocity and TKE. In contrast, the BEP configuration substantially reduces near-surface CO_2 levels relative to No_URB and SLUCM. This behavior is physically consistent with its enhanced sensible heat flux, stronger turbulence production, and deeper daytime boundary layers, which promote efficient vertical dilution of surface emissions. However, the tendency of BEP to overestimate sensible heat flux and slightly over-deepen the boundary layer leads to excessive mixing, resulting in a systematic underestimation of near-surface CO_2 and reduced temporal coherence with observations. The BEM scheme provides the most balanced representation of wintertime CO_2 variability. Its improved treatment of building energy exchanges modifies surface energy partitioning, leading to enhanced sensible heat fluxes and friction velocity. Although these quantities are overestimated, their combined effect produces realistic levels of TKE and PBLH.

https://doi.org/10.5194/egusphere-2026-2109
Preprint. Discussion started: 1 July 2026

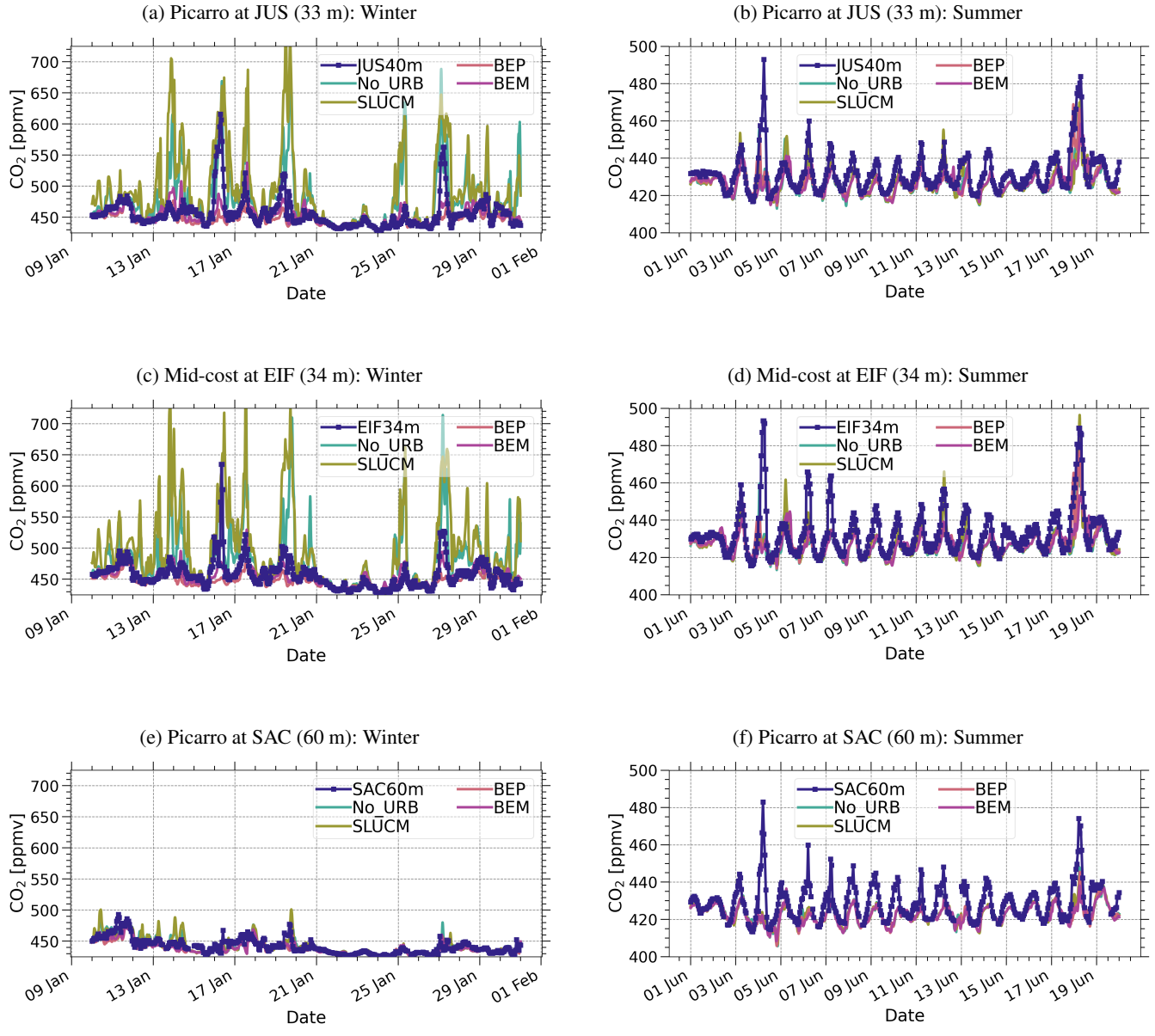

Figure 10. Time series of near-surface CO_2 mixing ratios during winter (10–31 January) and summer (1–20 June) 2024, comparing WRF simulations with different urban schemes to observations from the Picarro network and Mid-Cost hourly data: (a, c, e) winter at JUS, EIF, and SAC; (b, d, f) summer at the same sites.

https://doi.org/10.5194/egusphere-2026-2109
Preprint. Discussion started: 1 July 2026

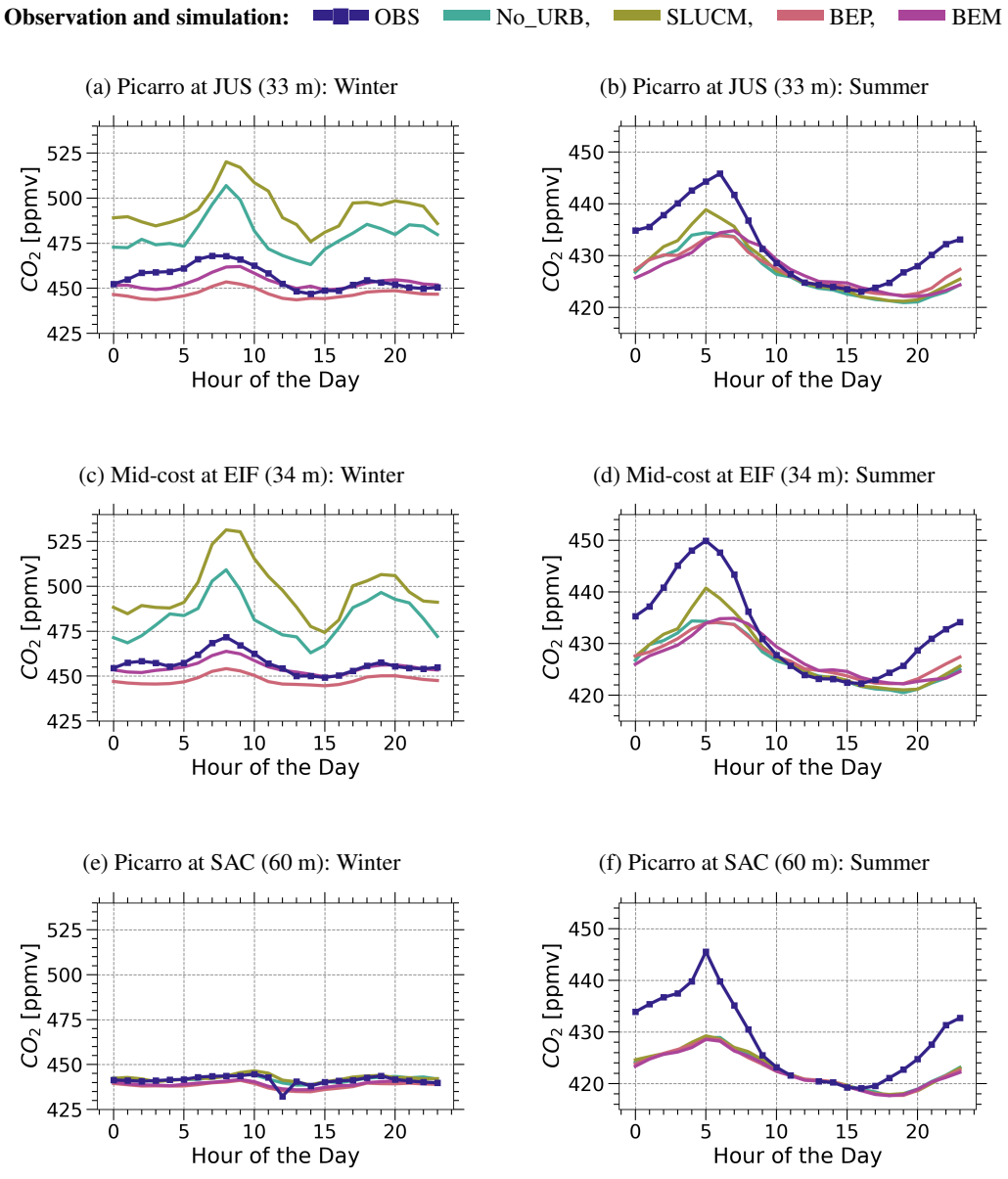

Figure 11. Diurnal cycles of near-surface CO_2 mixing ratios during winter (10–31 January) and summer (1–20 June) 2024, comparing WRF simulations with different urban schemes to observations from the Picarro network and Mid-Cost hourly data: (a, c, e) winter at JUS, EIF, and SAC; (b, d, f) summer at the same sites.

https://doi.org/10.5194/egusphere-2026-2109
Preprint. Discussion started: 1 July 2026

This balance translates into an effective but not excessive dilution of surface emissions, producing near-surface CO_2 mixing ratios that closely track observed temporal variability while maintaining minimal bias.

These results demonstrate that wintertime near-surface CO_2 mixing ratios are tightly coupled to urban induced modifications of boundary layer structure and turbulence. Differences among urban physics schemes primarily influence CO_2 through their control on sensible heat flux, friction velocity, TKE, and PBLH, with near-surface meteorological variables responding as part of this coupled boundary layer system rather than acting independently. The consistency between CO_2, surface fluxes, turbulence diagnostics, and PBLH underscores the critical role of urban energy partitioning in governing tracer transport under stable to weakly convective winter conditions.

During summer, differences among urban physics schemes are substantially reduced, and all configurations produce similar diurnal variability and overall magnitudes of near-surface CO_2 mixing ratios (Figures 12b and 12d). In contrast to winter, No_URB and SLUCM no longer exhibit strong positive biases, but instead yield CO_2 levels comparable to those simulated by BEP and BEM. Agreement with observations is generally good across all schemes, with moderate to high temporal correlations for both the Picarro and Mid-cost networks and relatively small biases and error magnitudes. This convergence among schemes reflects the dominant role of strong convective mixing during summer. Although BEP and BEM slightly overestimate friction velocity and TKE in urban areas, and all schemes tend to overestimate daytime sensible heat flux, the resulting PBLH remains broadly similar across configurations. The combination of strong surface forcing and comparable boundary layer heights promotes effective vertical dilution of CO_2, thereby reducing the sensitivity of near-surface concentrations to differences in urban representation. As a result, the strong contrasts observed in winter, when boundary layer development is more directly controlled by urban physics are largely muted under summertime conditions. Minor differences persist among schemes and between observational networks, with slightly larger biases in the Mid-cost network, but these variations remain small compared to wintertime discrepancies. Overall, the summer results indicate that when convective forcing is strong, boundary layer dynamics dominate CO_2 variability and limit the influence of urban physics parameterization on near-surface concentrations.

3.7 Sensitivity to PBL scheme and consequences for near surface CO_2 under BEM configuration

To assess the robustness of the CO_2 simulations to boundary layer parameterization, additional experiments were conducted using the BEM urban configuration coupled with the MYJ, YSU, and BouLac PBL schemes. Figure 13 shows the diurnal cycles of surface HFX and u_* at JUS, and PBLH at QUALAIR, for winter (10-31 January) and summer (01-20 June) 2024. HFX and u_* remain nearly identical among the three PBL schemes in both seasons, indicating comparable surface forcing. However, BouLac slightly overestimates u_* compared with the other schemes during winter. In general, all schemes overestimate u_*, with a bias of about 0.5 m s^{-1} relative to observations. For HFX, MYJ shows the largest bias in winter compared to BouLac and YSU, although all schemes overestimate HFX. In summer, daytime HFX values are similar among the schemes, whereas MYJ exhibits a much larger nighttime bias. Notable differences also emerge in the diagnosed PBLH, highlighting a strong scheme dependency. In general, BouLac and YSU produce a deeper boundary layer than MYJ in both seasons. During winter, all schemes overestimate PBLH compared with observations. In summer, BouLac and YSU slightly overestimate PBLH up to the time of maximum development, whereas MYJ better reproduces the observed boundary layer growth. However, after the peak,

https://doi.org/10.5194/egusphere-2026-2109
Preprint. Discussion started: 1 July 2026

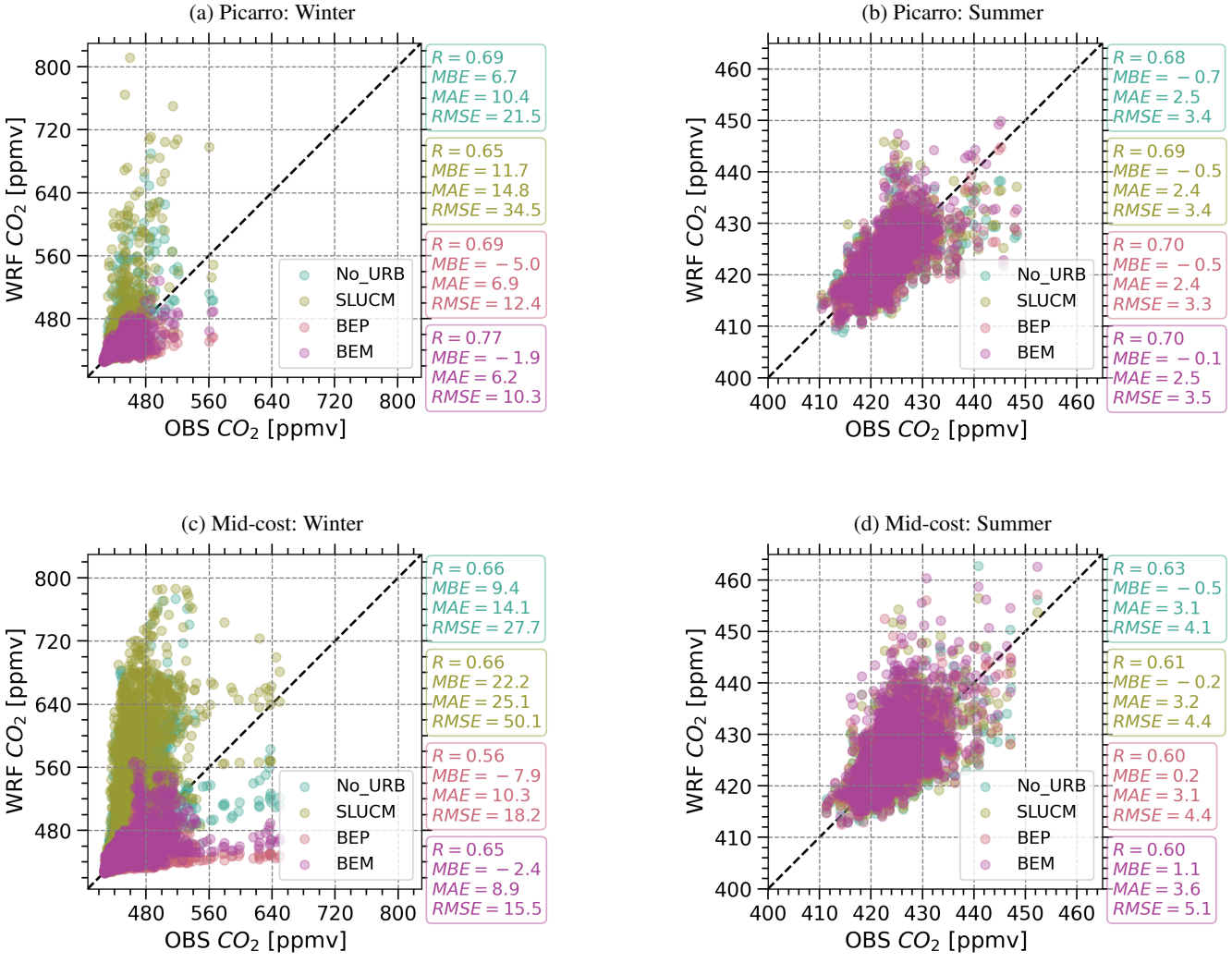

Figure 12. Comparison of near-surface CO_2 mixing ratios simulated by WRF at 900 m resolution for winter (10-31 January) and summer (01-20 June) periods. Data are averaged over the active daytime period (11–16 UTC in winter and 10–18 UTC in summer). Results are shown for four urban physics configurations: No_URB, SLUCM, BEP, and BEM. Statistics (correlation coefficient R, mean bias error MBE, mean absolute error MAE, and root mean square error RMSE) are computed over all stations.

https://doi.org/10.5194/egusphere-2026-2109
Preprint. Discussion started: 1 July 2026

all schemes fail to maintain the deep late afternoon boundary layer indicated by the observations. This behavior is consistent with previous evaluations of local TKE based schemes under convective conditions (Hu et al., 2010). Similar sensitivity to PBL representation has also been found in mesoscale urban modeling studies, where variations in PBL schemes substantially influenced simulated boundary layer characteristics in the context of the Indianapolis Flux Experiment (INFLUX) simulations (Sarmiento et al., 2017)

To illustrate the impact of PBL schemes on near-surface concentrations over the diurnal cycle, Figure 14 shows the diurnal cycles of CO_2 at JUS and EIF in the core urban area of Paris, during winter (10–31 January) and summer (01–20 June) 2024. In winter, the MYJ scheme closely reproduces the observed concentrations, while YSU tends to overestimate at night and underestimate during the daytime. BouLac exhibits a large underestimation, which is consistent with the deeper PBLH shown in the Figure 13. In summer, all schemes capture the daytime variation and magnitude well, aligning closely with observations. However, during the night and early morning, all schemes underestimate concentrations, with YSU showing a slight improvement over the others.

These results indicate that near-surface CO_2 mixing ratios are strongly controlled by stability, particularly during winter nights, where schemes with stronger sensitivity to suppressed mixing reproduce observations more accurately, with MYJ performing best. During summer days, despite differences in PBLH among the schemes, all capture the daytime concentrations similarly, highlighting that convective mixing dominates and reduces sensitivity to PBLH errors. At night and in transitional periods, differences in vertical mixing become more important, with YSU showing slightly better performance in summer nights, while MYJ consistently performs best during winter when CO_2 accumulation is strongest. Overall, these patterns reveal that near-surface CO_2 mixing ratios are largely governed by the interplay of turbulent mixing and boundary layer structure, with the MYJ configuration best capturing winter accumulation. The strong winter sensitivity to vertical mixing is consistent with previous studies over Paris that identified boundary layer representation as a dominant source of uncertainty in modeled CO_2, particularly under stable conditions (Lian et al., 2021). Similar sensitivity of simulated CO_2 mole fractions to PBL parameterization, as well as to the combined influence of multiple physical schemes, has been documented in regional transport studies over the US Midwest (Díaz-Isaac et al., 2018). More generally, tracer transport analyses have demonstrated the central role of PBL turbulence in scalar dispersion (McGrath-Spangler et al., 2015), showing that near-surface scalar concentrations are primarily governed by turbulent mixing in combination with PBL structure (Lopez-Coto et al., 2020). Our results reinforce that accurate representation of turbulent mixing, alongside PBLH, is essential for simulating diurnal variations in near-surface CO_2.

4 Discussion

This study demonstrates that the representation of urban surface processes exerts a first order control on simulated planetary boundary layer (PBL) dynamics and, consequently, on near-surface CO_2 mixing ratios over Paris. Across both winter and summer periods, differences among urban physics schemes consistently manifest through their modulation of surface energy partitioning, turbulence generation, and boundary layer development, rather than through changes in large scale meteorological forcing.

https://doi.org/10.5194/egusphere-2026-2109
Preprint. Discussion started: 1 July 2026

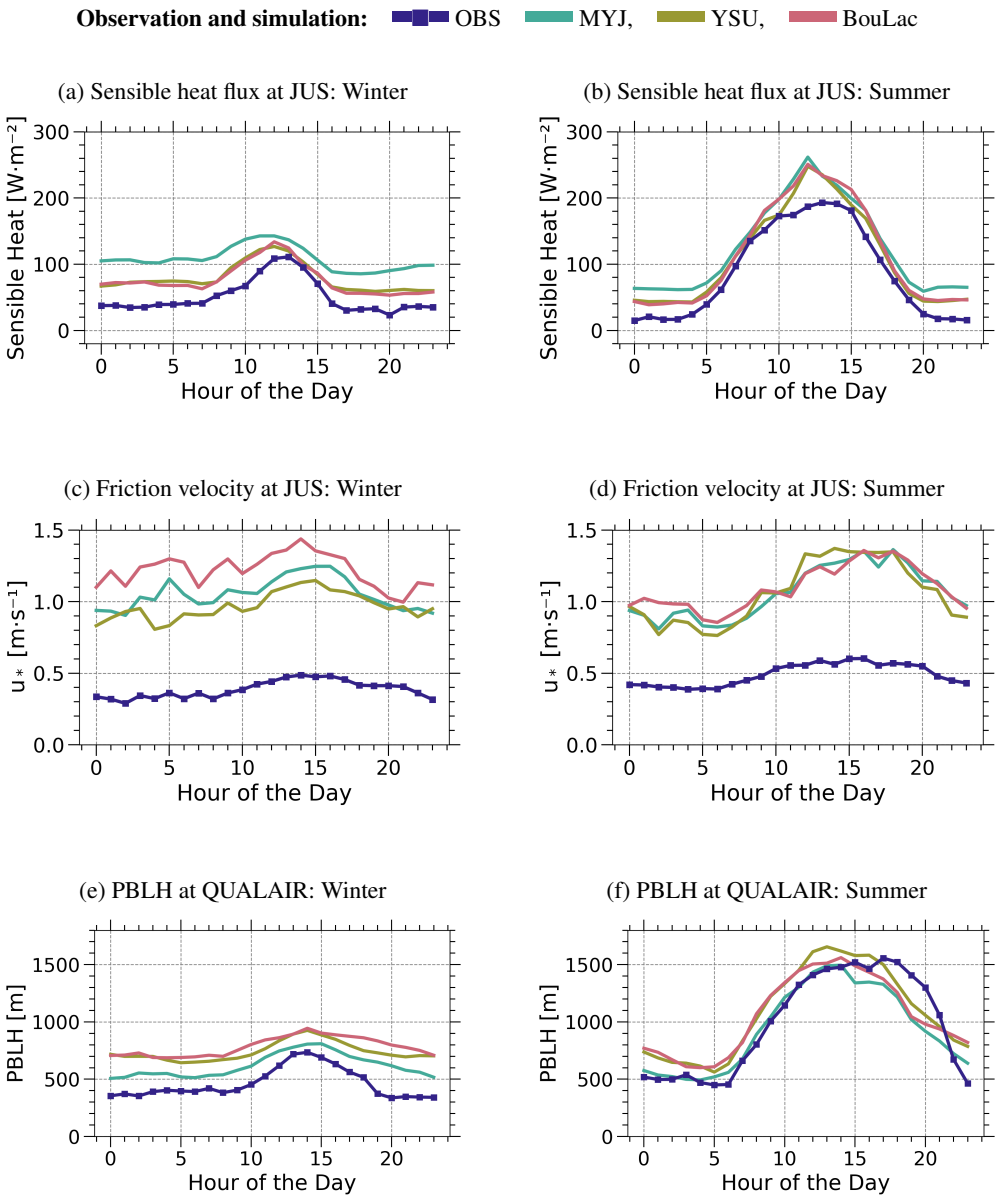

Figure 13. Diurnal cycles of sensible heat flux and friction velocity at JUS, and PBLH at QUALAIR, for winter (January) and summer (June) 2024 using the BEM configuration with MYJ, YSU, and BouLac schemes.

https://doi.org/10.5194/egusphere-2026-2109
Preprint. Discussion started: 1 July 2026

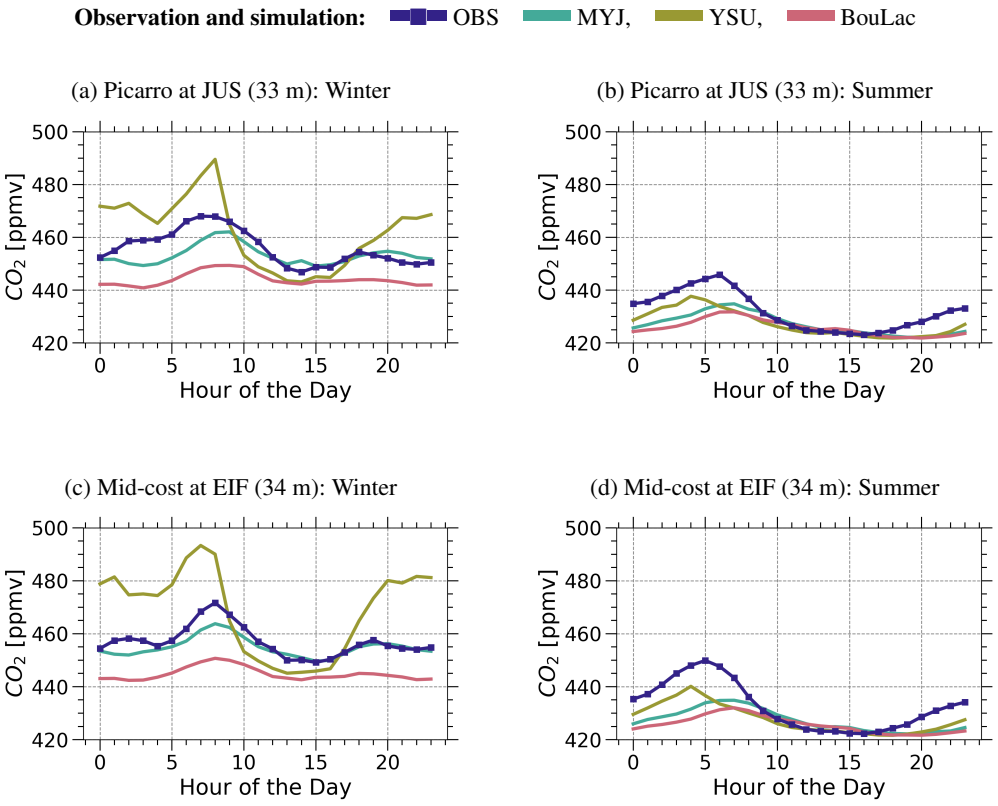

Figure 14. Diurnal cycles of near-surface CO_2 mixing ratios during winter (10–31 January) and summer (1–20 June) 2024 at JUS (33 m, Picarro) and EIF (34 m, mid-cost), using the BEM urban configuration coupled with MYJ, YSU, and BouLac PBL schemes. Simulations are compared with observations to assess the sensitivity of CO_2 to boundary layer parameterization under contrasting seasonal conditions.

In winter, urban physics strongly modulate daytime PBL development, and the error distributions of surface fluxes, turbulence, and PBLH (Figures 15) help clarify the mechanisms behind the contrasting scheme behaviors.

The No_URB and SLUCM configurations exhibit error distributions of HFX that are narrow and centered slightly below zero, together with near neutral or weakly underestimated u_* and a pronounced underestimation of TKE. This combination systematically limits both buoyancy production and turbulent transport, resulting in consistently shallow boundary layers, as reflected by PBLH error distributions skewed toward negative values. The coherence of these distributions indicates a physically consistent but weakly forced boundary layer that is unable to respond effectively to daytime heating.

In contrast, the BEP scheme shows a fundamentally different balance among processes. Its HFX error distribution is broad and strongly shifted toward positive values, indicating frequent episodes of excessive buoyancy forcing, while LH errors remain comparatively small and play a secondary role. BEP also exhibits a strong positive bias in u_*, reflecting enhanced mechanical forcing by explicit building drag. Despite this, near-surface TKE remains slightly underestimated, suggesting that turbulence production is not fully converted into sustained vertical mixing. Nevertheless, the combined effects of excessive surface heating

https://doi.org/10.5194/egusphere-2026-2109
Preprint. Discussion started: 1 July 2026

and strong mechanical forcing are sufficient to offset the TKE deficit, yielding a PBLH error distribution centered near zero but with a slight positive bias. This explains why BEP can reproduce near correct mean PBLH while still exhibiting physically imbalanced surface turbulence interactions.

The BEM scheme achieves a more coherent and physically balanced coupling across all variables. Compared to BEP, its HFX errors are smaller and more consistent, though not perfectly centered, while u_* exhibits a broader distribution with a slightly higher mean than BEP, but its lower quartile remains near zero, supporting effective mechanical mixing. Although TKE is still underestimated on average, the bulk of its error distribution is narrower than in No_URB and SLUCM, with only occasional extreme values, indicating generally improved turbulence representation. This balanced combination of buoyancy and mechanical forcing yields a tightly centered PBLH error distribution with median and mean values close to zero, indicating a realistic boundary layer response without systematic over or under development.

Taken together, the wintertime error distributions demonstrate that PBLH accuracy does not depend on any single process but emerges from the combined regulation of surface heating, momentum exchange, and turbulence generation. Excessive HFX and u_* can compensate for moderate TKE deficits, as in BEP, while realistic PBLH in BEM arises from a more consistent partitioning of errors across all contributing processes. Conversely, the coherent underestimation of heat flux and turbulence in No_URB and SLUCM leads inevitably to suppressed boundary-layer growth. This integrated view reinforces the importance of balanced urban physics representations for physically realistic boundary layer development.

In summer, the error distributions reveal that all schemes overestimate HFX, though with varying magnitudes: No_URB exhibits the largest positive bias, whereas BEM is closest to zero, with its first quartile aligned near zero (Figure 15f). LH shows more scheme dependent behavior: No_URB slightly underestimates, SLUCM and BEP exhibits a narrow error distribution centered around zero, and BEM shows a slight positive bias (Figure 15g).

u_* errors largely mirror winter patterns. BEM maintains a similar magnitude of overestimation, BEP and No_URB shows a small positive bias, and SLUCM exhibits a narrow distribution centered around zero (Figure 15h). TKE errors are consistently negative across all schemes, with the zero line lying above the bulk of the distribution (above the 3rd quartile), indicating persistent underestimation of turbulence (Figure 15i). Despite differences in surface and turbulence forcing, the PBLH errors remain broadly comparable across all schemes, with distributions generally centered between approximately -0.1 and -0.2 km (Figure 15j).

These distributions complement the broader result that, in summer, all schemes converge toward a similar boundary layer structure, characterized by an early saturation of convective growth and a limited ability to sustain further afternoon deepening relative to observations. Even though BEM reduces HFX errors compared to other schemes and maintains enhanced mechanical forcing, the PBL fails to deepen further in the afternoon. This convergence indicates a seasonal shift in sensitivity: wintertime PBLH strongly depends on the interaction of surface energy partitioning, urban morphology, and turbulence, whereas summertime PBL development appears constrained by more general model limitations, such as entrainment at the PBL top and vertical redistribution of turbulence as well as unresolved convective transport at kilometer-scale resolution. Consequently, differences among urban schemes in summer remain relatively small, even when contrasts exist in surface forcing and turbulence production.

https://doi.org/10.5194/egusphere-2026-2109
Preprint. Discussion started: 1 July 2026

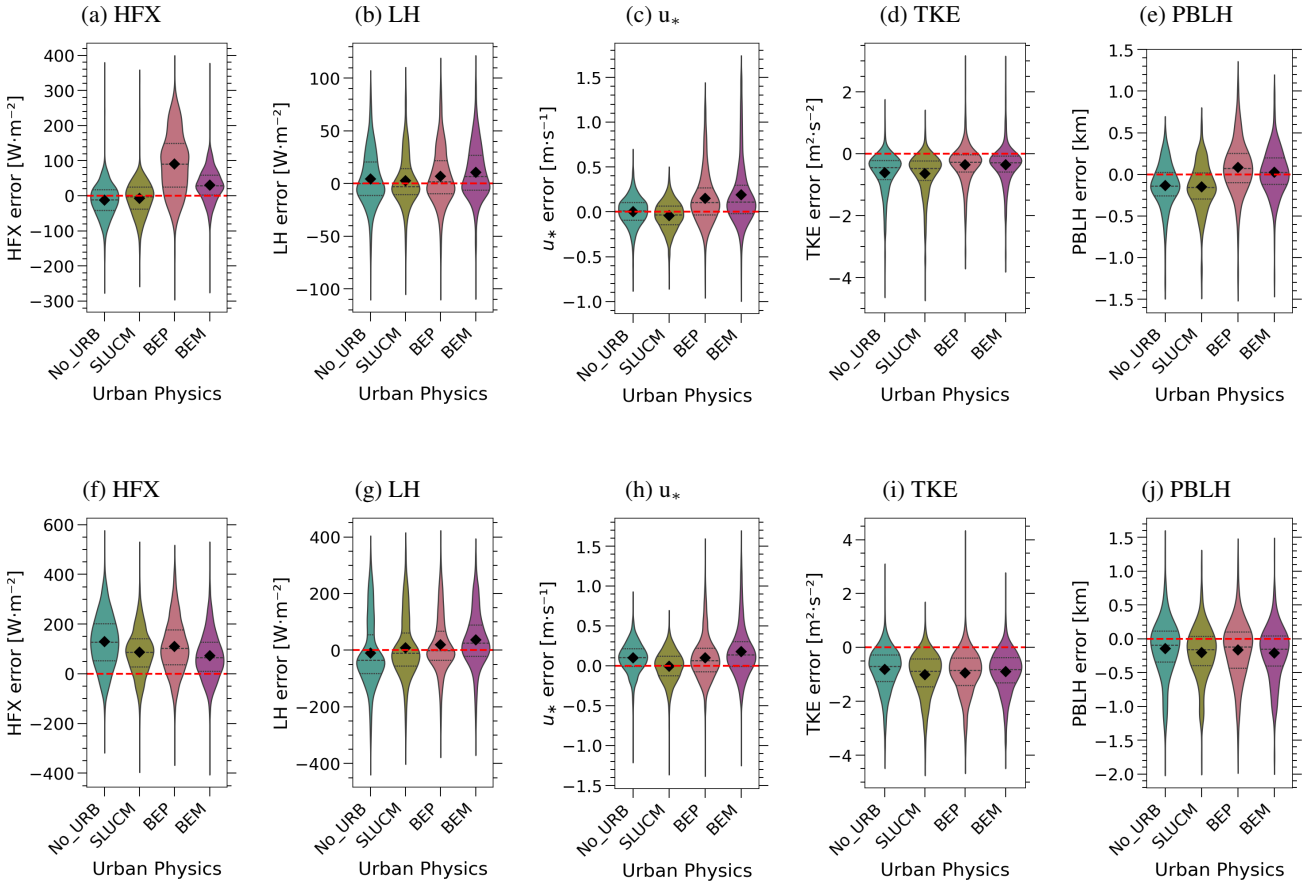

Figure 15. Distribution of errors (WRF - observations) for near-surface sensible heat flux (HFX), latent heat flux (LH), friction velocity (u_*), turbulent kinetic energy (TKE), and planetary boundary layer height (PBLH) during winter (10–31 January, top panels) and summer (1–20 June, bottom panels) 2024. Results compare WRF simulations using different urban parameterization schemes against observations across all sites during active daytime conditions. Black points indicate the mean error, dashed black lines represent the inter-quartile range, and the red dashed line denotes zero error.

https://doi.org/10.5194/egusphere-2026-2109
Preprint. Discussion started: 1 July 2026

The CO_2 analysis confirms that boundary layer structure and turbulence act as the primary mediators through which urban physics influence near surface concentrations. In winter, shallow boundary layers and weak turbulence in No_URB and SLUCM configurations favor excessive CO_2 accumulation, occasionally allowing these schemes to reproduce observed extreme peaks. However, such agreement arises from physically inconsistent mechanisms, namely artificially suppressed mixing, rather than from realistic urban atmosphere coupling. In contrast, BEP and BEM yield more physically consistent CO_2 variability by enhancing turbulent mixing and boundary layer growth, though at the cost of underestimating the most extreme accumulation events.

Importantly, this contrast highlights a key modeling pitfall: reproducing observed concentration peaks does not necessarily imply realistic process representation. The time series and diurnal analyses show that physically consistent schemes (particularly BEM) better capture background levels and temporal variability, even when peak magnitudes are partially underestimated. This finding underscores the need to prioritize physically realistic boundary layer dynamics over purely statistical agreement when simulating urban CO_2.

In summer, near-surface CO_2 mixing ratios exhibit markedly reduced sensitivity to urban physics. All schemes produce similar temporal evolution and magnitudes across urban and suburban sites, consistent with the convergence in PBLH. Nighttime and early morning CO_2 peaks are systematically underestimated, reflecting insufficient stabilization of the near-surface atmosphere rather than errors in PBL depth. During daytime, however, the observed CO_2 decline is well reproduced despite the premature saturation of PBLH, because this phase coincides with decreasing concentrations driven by ongoing mixing and an expanding mixed-layer volume. Consequently, summertime CO_2 variability is governed more by shared model limitations than by differences in urban representation.

The consistently better agreement with the Picarro network compared to the Mid-cost network across both seasons suggests that measurement characteristics, such as instrument precision, calibration stability, and response time play a non negligible role in model–observation comparisons. This emphasizes the importance of accounting for observational uncertainty when evaluating urban CO_2 simulations, particularly when differences among model configurations are subtle, as in summer.

The sensitivity of near-surface CO_2 to PBL scheme reflects differences in turbulence representation and boundary layer development. During winter, MYJ reproduces observed CO_2 most accurately, capturing realistic nighttime accumulation and daytime mixing, while YSU overestimates night concentrations and underestimates daytime values, and BouLac exhibits larger underestimation due to deeper mixing. In summer, daytime CO_2 is relatively insensitive to PBL scheme, as convective mixing dominates, though nighttime and early morning concentrations remain slightly better represented by YSU. These results indicate that accurate simulation of near-surface CO_2 requires PBL schemes that balance buoyancy and mechanical mixing, with MYJ performing best especially in stable condition.

Among the tested configurations, BEM coupled with MYJ emerges as the most physically consistent combination across seasons. Its balanced treatment of surface energy exchanges produces realistic HFX, u_*, turbulence levels, and boundary layer structure, yielding the most robust representation of near-surface CO_2 variability. While BEP enhances mixing excessively and simpler schemes rely on unrealistic suppression of turbulence, BEM provides a defensible compromise between physical

https://doi.org/10.5194/egusphere-2026-2109
Preprint. Discussion started: 1 July 2026

realism and model behavior, capturing both winter accumulation and summer diurnal variability more accurately than alternative configurations.

The results presented here align with and extend prior work demonstrating that urban canopy model complexity exerts a first-order influence on boundary layer structure and near-surface scalar transport. In mesoscale models, the hierarchy of urban canopy models (UCM), from simple bulk parameterizations such as the SLUCM (Kusaka et al., 2001) to the multilayer BEP (Martilli et al., 2002)) and BEP+BEM (Salamanca and Martilli, 2010), mimics the three-dimensionality of buildings and produces detailed momentum and thermal forcings based on complex urban morphology, and the usage of more sophisticated UCM has generally resulted in better forecasts in the urban environment. Our finding that BEM achieves the most physically balanced surface energy partitioning is consistent with offline evaluations by Salamanca and Martilli (2010), who showed that the inclusion of a building energy model substantially improved urban turbulent flux representation. Critically, our CO_2 analysis adds a new dimension to this body of work: it demonstrates that errors in boundary layer dynamics propagate directly into tracer concentration biases, as also highlighted for Paris by Lac et al. (2013); Lian et al. (2021), who stressed the importance of accurate PBL height representation for city-scale CO_2 transport modeling.

These findings motivate the focus of Part 2 of this study. While Part 1 establishes the importance of urban physics for boundary layer scale CO_2 variability and supports the use of multilayer UCMs coupled with TKE-based PBL schemes, including emerging multilayer BEP+BEM developments (Pappaccogli et al., 2025) that improve flux and momentum representation in complex urban environments, important aspects of fine-scale CO_2 gradients, plume structures, and other urban variables (e.g., temperature, wind, turbulence) remain unresolved at kilometer-scale resolution. This highlights the need to transition toward higher-resolution simulations and large-eddy simulation frameworks capable of explicitly resolving building-scale turbulence, street-canyon ventilation, and localized scalar variability.

5 Conclusion

This study systematically evaluates the influence of urban physics representations on boundary-layer dynamics and near-surface CO_2 mixing ratios over Paris under contrasting winter and summer conditions. The main conclusions can be summarized as follows.

In winter, differences among urban schemes are modest at the surface but become more pronounced in the vertical structure of wind within the lowest 400–500 m, where urban canopy processes and turbulence dominate. Multi-layer schemes (BEP and BEM) consistently improve wind speed and direction profiles relative to simpler configurations, reducing RMSE in the lower boundary layer and better representing momentum distribution relevant for urban CO_2 transport. Above this layer, scheme differences diminish as synoptic and mesoscale forcing prevails.

Urban physics exert a strong control on wintertime boundary layer development and CO_2 variability. Differences among urban schemes arise primarily through their impact on surface energy partitioning and turbulence generation, leading to substantial contrasts in planetary boundary layer height and near-surface CO_2 accumulation.

https://doi.org/10.5194/egusphere-2026-2109
Preprint. Discussion started: 1 July 2026

Apparent agreement with observed CO_2 extremes does not necessarily indicate physically realistic behavior. Simpler urban configurations may reproduce high concentrations through artificially suppressed mixing, whereas schemes with more consistent representations of urban energy exchange and turbulence provide more reliable background levels and diurnal variability.

In summer, the sensitivity of near-surface CO_2 to urban physics is markedly reduced. All configurations exhibit similar CO_2 behavior despite differences in surface fluxes and turbulence intensity, reflecting a common limitation in the representation of convective boundary layer growth. The premature saturation of daytime PBLH and the afternoon deepening of the PBL not being sustained as observed across all schemes suggest that entrainment and vertical redistribution of turbulence, rather than surface forcing alone, constrain summertime model performance.

Among the tested configurations, the Building Energy Model (BEM) provides the most balanced and physically consistent representation across seasons. Its treatment of urban energy exchanges yields realistic boundary-layer structure and CO_2 variability, making it a robust baseline for subsequent analyses.

Sensitivity tests with different PBL schemes indicate that MYJ best reproduces wintertime near-surface CO_2 variability, capturing realistic nighttime accumulation and daytime mixing, whereas YSU and BouLac show biases consistent with over or underestimation of turbulence and boundary layer growth. This reinforces that accurate turbulent mixing representation, in combination with urban energy exchanges, is critical for physically consistent CO_2 simulations.

At kilometer scale resolution, however, urban CO_2 simulations remain challenged in their ability to represent fine scale spatial gradients. While Part 1 captures the dominant boundary layer controls on near surface CO_2 variability, important aspects of urban CO_2 plumes, such as sharp urban–rural gradients and localized concentration structures relevant for satellite based analyses, may not be fully resolved.

Building on these findings, Part 2 of this study will investigate how horizontal resolution and turbulence resolving approaches influence the representation of urban CO_2 plumes. High resolution and large eddy simulations will be used to assess how fine scale turbulence and urban heterogeneity shape CO_2 structures observable from space, using the BEM configuration as a physically robust reference.

Future work could explore the influence of scheme-dependent CO_2 release heights, including sensitivity experiments using fluxes injected at different vertical levels or derived from three-dimensional emission sources within multi-layer urban schemes BEM.

https://doi.org/10.5194/egusphere-2026-2109
Preprint. Discussion started: 1 July 2026

Appendix A: Summary of urban physics parameterizations options used in this study

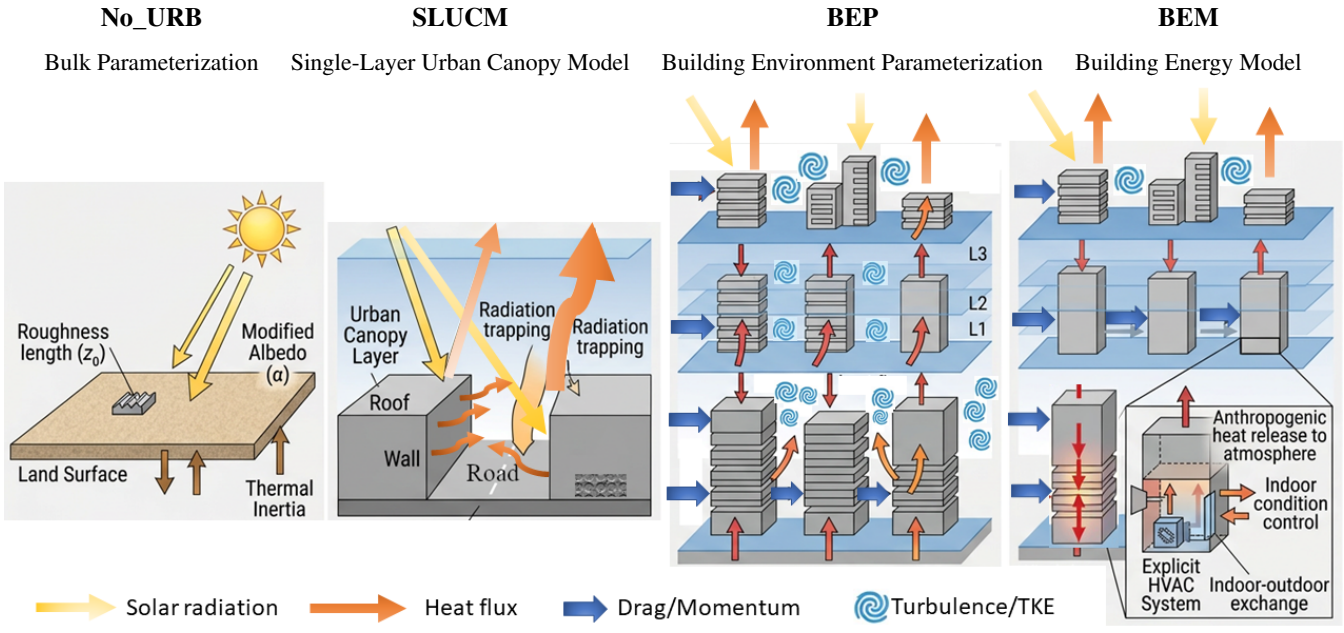

Figure A1. Comparison of urban physics parameterizations in the Weather Research and Forecasting (WRF) model. The description, key features, and physical representations are summarized in Table A1.

https://doi.org/10.5194/egusphere-2026-2109
Preprint. Discussion started: 1 July 2026

Table A1. Summary of urban physics options in WRF (Noah Land Surface Model (LSM) used)

Urban Scheme	**Description**	**Key Features**	**Physical Representation**
No_URB	Urban land cover included but treated with Noah LSM only	Default land surface physics; no explicit urban canopy processes; heat fluxes, temperature, and soil moisture calculated as for natural surfaces. Modifies surface roughness length (z_0), albedo (α), and thermal inertia. Does not account for 3D structure.	Urban areas represented as generic land-use type; no differentiation between roofs, walls, or streets; no anthropogenic heat; acts as a baseline/control; Logarithmic vertical wind profile.
SLUCM	3-category urban canopy: roofs, walls, streets	Single-layer urban canopy; Includes street canyons, shadow effects, and reflection. Calculates energy balance for roofs, walls, and roads; green roofs	Represents urban heterogeneity at surface level; simplified street canyon effects; only one vertical layer; interacts with the atmosphere at the lowest model level. Logarithmic vertical wind profile.
BEP	Multi-layer urban canopy model	Resolves multiple vertical layers of air in the urban canopy; building heights above the lowest model level considered; shading, trapping, and roughness included; Recognizes the vertical distribution of buildings. Directly affects momentum, heat, and Turbulent Kinetic Energy (TKE) at multiple vertical levels.	Explicit 3D building effects distributed across several atmospheric grid cells; interactions of walls, roofs, and streets with atmosphere; urban turbulence and heat storage realistically represented; Resolved vertical wind profile.
BEM	BEP + building energy budget	Extension of BEP. Simulates indoor-outdoor heat exchange, includes heating and cooling systems and anthropogenic heat release from buildings.	3D buildings with internal thermal mass and active climate control systems; simulates Heating, Ventilation, and Air Conditioning (HVAC) and internal energy fluxes; Resolved vertical wind profile.

https://doi.org/10.5194/egusphere-2026-2109
Preprint. Discussion started: 1 July 2026

Appendix B: Location details of the Doppler wind profiler LIDAR

Table B1. Doppler wind profiler LIDAR measurement stations locations.

Station Code	Station Name	Latitude (°)	Longitude (°)	Altitude (m)	Height station AGL (m)
PAROIS	Aéroport Roissy-Charles-de-Gaulle	49.0160	2.53366	112	4
PACHEM	Chemin Vert Bobigny	48.9046	2.44470	98	52
PAJUSS	Tour Zamansky Jussieu	48.8469	2.3555	125	88
PALUPD	LISA Université Paris Diderot	48.8278	2.38064	65	26
PAARBO	Arboretum de la Vallée-aux-Loups	48.7717	2.26769	99	1
PASIRT	Observatoire SIRTA	48.7173	2.20887	154	0

Appendix C: Location details of the measurement of surface turbulent flux

Table C1. Surface turbulence flux measurement stations and basic characteristics.

Station Name	Station Code	Latitude (°)	Longitude (°)	Altitude (m)	Height station AGL (m)
Jussieu	JUS	48.8461	2.3548	42	31
Romainville	RMV	48.8854	2.4225	128	103
Vincennes	VIN	48.8347	2.4664	62	23
Saclay	SAC	48.7227	2.1420	160	102
Fontainebleau-Barbeau	FON	48.4764	2.7801	103	37
Grignon	GRI	48.8442	1.9519	125	15
SIRTA Palaiseau	SIRTA	48.7130	2.2080	156	2, 50

https://doi.org/10.5194/egusphere-2026-2109
Preprint. Discussion started: 1 July 2026

Appendix D: Location details of Automatic LIDAR Ceilometers (ALC) locations used for planetary boundary layer height (PBLH) retrievals

Table D1. Planetary Boundary Layer Height (PBLH) measurement stations and basic characteristics.

Station Code	Latitude (°)	Longitude (°)	Altitude (m)
CHAM	49.2192	2.6114	73
ROIS	49.0160	2.5337	112
BOBI	48.9047	2.4447	97
HOTE	48.8559	2.3520	28
MEUD	48.8037	2.2405	159
SIRTA	48.7173	2.2089	155
AUNA	48.4315	1.8314	156
QUALAIR	48.8470	2.3560	50
PALAISEAU	48.7181	2.2074	156

Appendix E: Location details of the Picarro and mid-cost network station over Paris area

Table E1. CO_2 Picarro measurement stations and basic characteristics.

Station Code	Latitude (°)	Longitude (°)	Altitude (m)	Height station AGL (m)
OVS	48.7779	2.0486	150	20
SAC	48.7227	2.1420	160	15, 60, 100
JUS	48.8464	2.3561	38	23, 33
COU	48.9242	2.5680	126	30
MEU	48.8025	2.2044	173	65
AND	49.0126	2.3018	175	60
ROV	48.8854	2.4225	128	103
CDS	48.8956	2.3880	43	34
GNS	49.0052	2.4205	81	36

https://doi.org/10.5194/egusphere-2026-2109
Preprint. Discussion started: 1 July 2026

Table E2. CO_2 mid-cost sensor network stations grouped by sensor type: HPP and K96

Station Code	Latitude (°)	Longitude (°)	Altitude (m)	Height station AGL (m)
HPP Sensors				
CIT	48.8283	2.2314	49	88
BED	48.8197	2.3714	53	32
CAP	48.8632	2.2908	58	30
MON	48.8863	2.3421	126	16
OBS	48.8364	2.3367	65	27
VES	48.8960	2.1415	46	47
CRE	48.7733	2.4693	70	39
DEF	48.8892	2.2506	43	165
IGR	48.7942	2.3481	126	65
K96 Sensors				
ATC	48.7100	2.1475	163	10
VIL	48.9349	2.3357	34	40.5
NAS	48.8383	2.3213	85	110
TF1	48.8340	2.2604	32	60
CDS	48.8953	2.3870	48	34
CAC	48.7887	2.3203	58	60
SAD	48.9442	2.3812	30	54
NEY	48.8992	2.3487	48	55
BAS	48.8524	2.3704	51	50
BOB	48.9077	2.4445	52	54
MRG	48.7569	2.3463	88	54
BNF	48.8334	2.3774	43	80
PLA	48.8300	2.3077	65	51
HBO	48.9080	2.3105	35	80
JUS	48.8464	2.3561	38	33
EIF	48.8554	2.2926	42	34.5
POM	48.8612	2.3525	53	45
HMO	48.7976	2.4528	41	100

Appendix F: Examples of Wind Roses at three Île-de-France Sites: ROV, JUS, and SIRTA

https://doi.org/10.5194/egusphere-2026-2109
Preprint. Discussion started: 1 July 2026

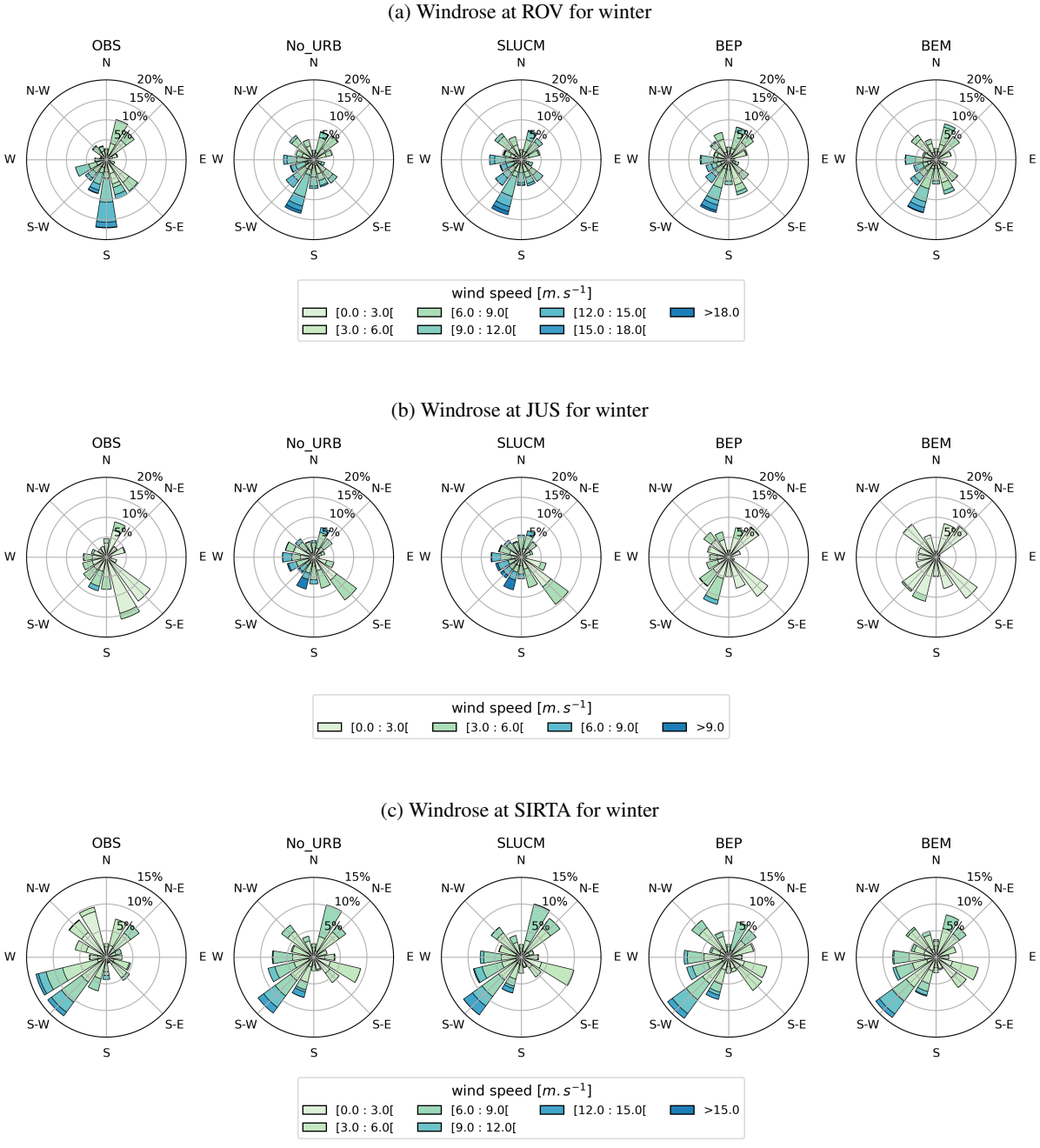

Figure F1. Wind rose distributions for the winter period (10–31 January 2024) at the three observation sites: ROV, JUS, and SIRTA. The figures show the frequency of wind direction and wind speed classes, allowing a comparison between WRF model simulations using different urban parameterization schemes and in situ observations.

https://doi.org/10.5194/egusphere-2026-2109
Preprint. Discussion started: 1 July 2026

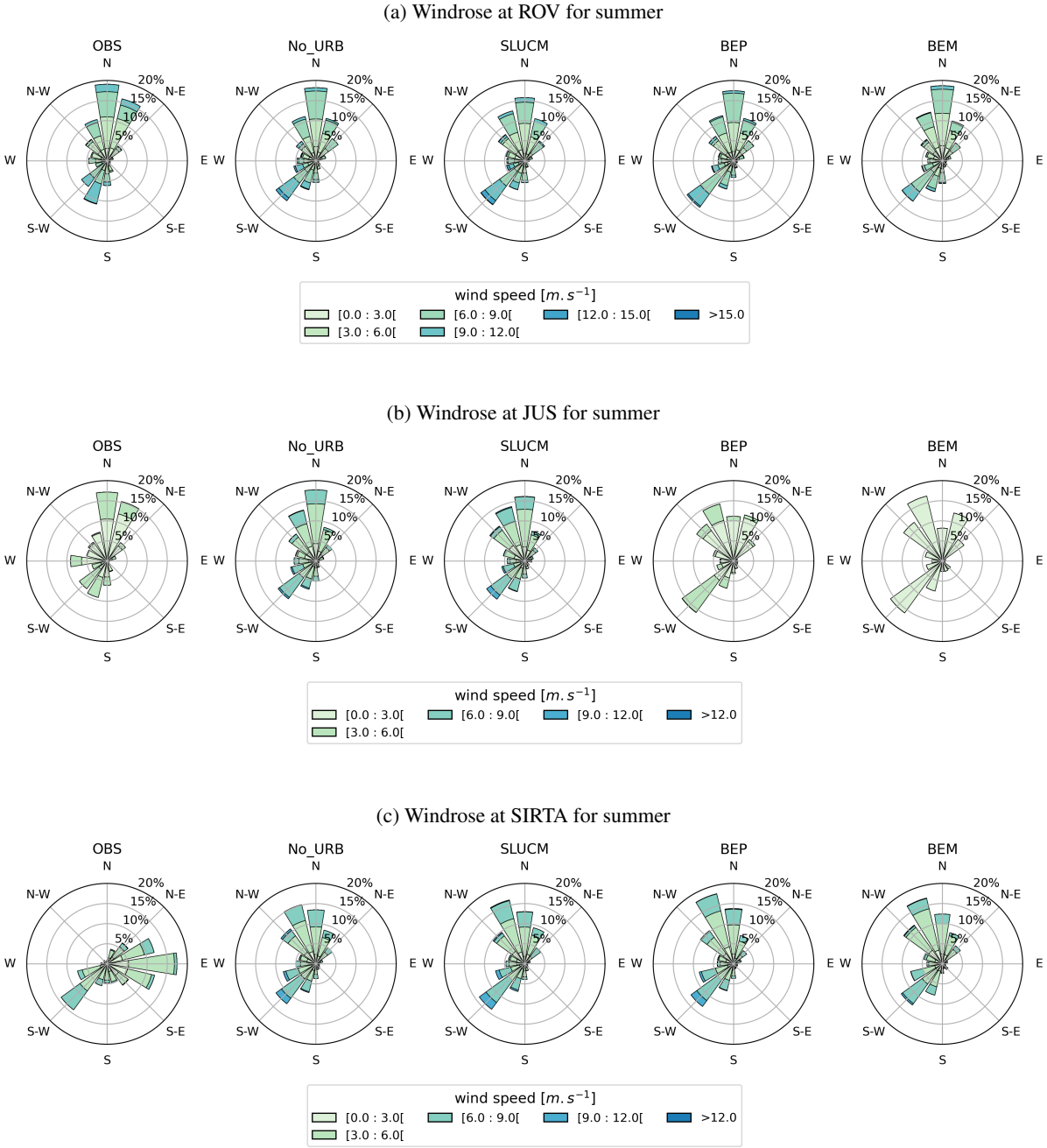

Figure F2. Wind rose distributions for the summer period (01–20 June 2024) at the three observation sites: ROV, JUS, and SIRTA. The figures show the frequency of wind direction and wind speed classes, allowing a comparison between WRF model simulations using different urban parameterization schemes and in situ observations.

https://doi.org/10.5194/egusphere-2026-2109
Preprint. Discussion started: 1 July 2026

Data availability. The wind lidar data used in this study are available on Zenodo at https://zenodo.org/records/17710093. Surface meteorological observations were obtained from the ACTRIS-FR and Météo-France networks and are available through the AERIS data portal at https://www.aeris-data.fr. The Copernicus Global Digital Elevation Model can be accessed at https://doi.org/10.5069/G9028PQB. The CAMS Greenhouse Gas Reanalysis dataset is provided via the Copernicus Atmosphere Data Store at https://doi.org/10.24380/8fck-9w87. The hybrid 100-m global land cover dataset including Local Climate Zones used for WRF model configuration is hosted on Zenodo at https://zenodo.org/records/7670653. Paris TCCON column CO_2 observations are available from the CaltechDATA repository at https://data.caltech.edu/records/6cj5y-spd74. Near-surface CO_2 station measurements were obtained from the ICOS Carbon Portal and can be accessed at https://data.icos-cp.eu/portal/. Planetary boundary layer height (PBLH) data from the Qualair platform are distributed via the IPSL Compute and Data Centre server at https://thredds-x.ipsl.fr/thredds/catalog/catalog.html. Surface flux datasets are taken from the ICOS ETC Level-2 flux product: Fontainebleau-Barbeau available at https://hdl.handle.net/11676/TmXcXgeyHJbBoxFwZqiB_XpW, Grignon at https://hdl.handle.net/11676/bEjMUuuYihCIxxm5nS8VrXdw, Paris Jussieu at https://hdl.handle.net/11676/yPaka4Xe4XdQ-wdMxNbvGCTd, Paris (FR-Jus, FR-Rmv and FR-Vin) at https://doi.org/10.18160/V4ZG-81AC, and long-term measurements from SIRTA at https://doi.org/10.25326/768. The Airparif emission inventories and the Urbisphere network PBLH data are confidential and not publicly available. Researchers interested in these datasets should contact the respective data providers directly.

Author contributions. AR and TL developed the idea of the paper. TL provided overall supervision and project leadership. AR performed the experiments, analyzed the results and wrote the manuscript. CA contributed to the modeling framework and its implementation. MC, MR, JD, and OL provided CO_2 observational data. AR, MK, and LJ participated in regular project meetings and discussions. AC and DL provided PBLH, Doppler Wind LIDAR data and flux data and also participated in regular project meetings and discussions. LD and OS provided CO_2 Airparif inventory data. LB and BL provided additional flux data. All authors contributed through critical review of the manuscript.

Competing interests. The authors declare that they have no competing interests.

Acknowledgements. The CATRINE project (grant agreement 101135000) is funded by the European Union. Views and opinions expressed are however those of the author(s) only and do not necessarily reflect those of the European Union or the Commission. Neither the European Union nor the granting authority can be held responsible for them. We acknowledge collaboration with the Atmosphere and Climate Competence Center (ACCC), funded by the Research Council of Finland (decision no. 359340). This work was supported by the Pilot Applications in Urban Landscapes (PAUL) - Towards integrated city observatories for greenhouse gases (ICOS Cities), funded by the European Union's Horizon 2020 Research and Innovation Programme under grant agreement No 101037319. T. Lauvaux was supported by the French Ministry of Research and Education (MESRI) through the Chaire de Professeur Junior (CASAL project). The authors acknowledge the QUALAIR team and infrastructure for their scientific support and especially Cristelle Cailteau-fischbach and Camille Viatte for letting access to the JUS site. QUALAIR is an observation platform of the OSU Ecce Terra of Sorbonne University operated by LATMOS with the support of IPSL. We acknowledge Jeremie Depuydt, Pedro Coimbra, Alain Fortineau and Anaïs Feron for helping getting the data of the JUS site. We also acknowledge the ERC Urbisphere project (Grant Agreement No 855005) for providing access to data and fruitful collaboration. The work

https://doi.org/10.5194/egusphere-2026-2109
Preprint. Discussion started: 1 July 2026

benefited from access to the HPC resources of IDRIS provided by GENCI (Grand Équipement National de Calcul Intensif). The authors would also like to acknowledge the use of the ROMEO HPC facility at the Université de Reims Champagne-Ardenne.

https://doi.org/10.5194/egusphere-2026-2109
Preprint. Discussion started: 1 July 2026

References

ACTRIS-FR and Météo-France: Surface meteorological observations from the French automatic station network, 6-minute temporal resolution, https://www.aeris-data.fr, accessed via AERIS;, 2024.

Agency, E. S.: Copernicus Global Digital Elevation Model, https://doi.org/10.5069/G9028PQB, 2024.

Agustí-Panareda, A., Barré, J., Massart, S., Inness, A., Aben, I., Ades, M., Baier, B. C., Balsamo, G., Borsdorff, T., Bousserez, N., Boussetta, S., Buchwitz, M., Cantarello, L., Crevoisier, C., Engelen, R., Eskes, H., Flemming, J., Garrigues, S., Hasekamp, O., Huijnen, V., Jones, L., Kipling, Z., Langerock, B., McNorton, J., Meilhac, N., Noël, S., Parrington, M., Peuch, V.-H., Ramonet, M., Razinger, M., Reuter, M., Ribas, R., Suttie, M., Sweeney, C., Tarniewicz, J., and Wu, L.: Technical note: The CAMS greenhouse gas reanalysis from 2003 to 2020, Atmospheric Chemistry and Physics, 23, 3829–3859, https://doi.org/10.5194/acp-23-3829-2023, 2023.

Berveiller, D., Dufrêne, E., Delpierre, N., Morfin, A., Francois, C., Vincent, G., Bazot, S., Soudani, K., Girardin, C., Guillot, T., and Perot-Guillaume, C.: ETC L2 Fluxes from Fontainebleau-Barbeau, 2018-12-31–2025-12-31, https://hdl.handle.net/11676/TmXcXgeyHJbBoxFwZqiB_XpW, 2026.

Bougeault, P. and Lacarrere, P.: Parameterization of Orography-Induced Turbulence in a Mesobeta–Scale Model, Monthly Weather Review, 117, 1872 – 1890, https://doi.org/10.1175/1520-0493(1989)117<1872:POOITI>2.0.CO;2, 1989.

Buchhorn, M., Smets, B., Bertels, L., Roo, B. D., Lesiv, M., Tsendbazar, N.-E., Li, L., and Tarko, A.: Copernicus Global Land Service: Land Cover 100m: version 3 Globe 2015-2019: Product User Manual, https://doi.org/10.5281/zenodo.3938963, 2020.

Buysse, P., Loubet, B., Depuydt, J., Durand, B., and Kalalian, C.: ETC L2 Fluxes from Grignon, 2020-12-31–2025-12-31, https://hdl.handle.net/11676/bEjMUuuYihCIxxm5nS8VrXdw, 2026.

Che, K., Lauvaux, T., Taquet, N., Stremme, W., Xu, Y., Alberti, C., Lopez, M., García-reynoso, A., Ciais, P., Liu, Y., Ramonet, M., and Grutter, M.: CO_2 Emissions Estimate From Mexico City Using Ground- and Space-Based Remote Sensing, Journal of Geophysical Research: Atmospheres, 129, https://doi.org/10.1029/2024jd041297, 2024.

Chen, F. and Dudhia, J.: Coupling an Advanced Land Surface–Hydrology Model with the Penn State–NCAR MM5 Modeling System. Part I: Model Implementation and Sensitivity, MWR, 129, 569–585, https://doi.org/10.1175/1520-0493(2001)129<0569:CAALSH>2.0.CO;2, 2001.

Chen, H. W., Zhang, F., Lauvaux, T., Scholze, M., Davis, K. J., and Alley, R. B.: Regional CO2 Inversion Through Ensemble-Based Simultaneous State and Parameter Estimation: TRACE Framework and Controlled Experiments, Journal of Advances in Modeling Earth Systems, 15, e2022MS003 208, https://doi.org/10.1029/2022MS003208, e2022MS003208 2022MS003208, 2023.

Chevallier, F., Bréon, F.-M., and Rayner, P. J.: Contribution of the Orbiting Carbon Observatory to the estimation of CO2 sources and sinks: Theoretical study in a variational data assimilation framework, Journal of Geophysical Research: Atmospheres, 112, https://doi.org/10.1029/2006JD007375, 2007.

Christen, A. and Vogt, R.: Energy and radiation balance of a central European city, International Journal of Climatology, 24, 1395–1421, https://doi.org/10.1002/joc.1074, 2004.

Churkina, G.: The Role of Urbanization in the Global Carbon Cycle, Frontiers in Ecology and Evolution, Volume 3 - 2015, https://doi.org/10.3389/fevo.2015.00144, 2016.

Crippa, M., Guizzardi, D., Pisoni, E., Solazzo, E., Guion, A., Muntean, M., Florczyk, A., Schiavina, M., Melchiorri, M., and Hutfilter, A. F.: Global anthropogenic emissions in urban areas: patterns, trends, and challenges, Environmental Research Letters, 16, 074 033, https://doi.org/10.1088/1748-9326/ac00e2, 2021.

https://doi.org/10.5194/egusphere-2026-2109
Preprint. Discussion started: 1 July 2026

Danjou, A., Broquet, G., Lian, J., Bréon, F.-M., and Lauvaux, T.: Evaluation of light atmospheric plume inversion methods using synthetic XCO2 satellite images to compute Paris CO_2 emissions, Remote Sensing of Environment, 305, 113 900, https://doi.org/10.1016/j.rse.2023.113900, 2024.

Delaria, E. R., Kim, J., Fitzmaurice, H. L., Newman, C., Wooldridge, P. J., Worthington, K., and Cohen, R. C.: The Berkeley Environmental Air-quality and CO_2 Network: field calibrations of sensor temperature dependence and assessment of network scale CO_2 accuracy, Atmospheric Measurement Techniques, 14, 5487–5500, https://doi.org/10.5194/amt-14-5487-2021, 2021.

Demuzere, M., He, C., Martilli, A., and Zonato, A.: A hybrid 100-m global land cover dataset with Local Climate Zones for WRF, https://doi.org/10.5281/zenodo.7670653, 2023.

Díaz-Isaac, L. I., Lauvaux, T., and Davis, K. J.: Impact of physical parameterizations and initial conditions on simulated atmospheric transport and CO_2 mole fractions in the US Midwest, Atmospheric Chemistry and Physics, 18, 14 813–14 835, https://doi.org/10.5194/acp-18-14813-2018, 2018.

Doc, J., Ramonet, M., Bréon, F.-M., Combaz, D., Chariot, M., Lopez, M., Delmotte, M., Cailteau-Fischbach, C., Nief, G., Laporte, N., Lauvaux, T., and Ciais, P.: The monitoring network of greenhouse gas (CO_2, CH_4) in the Paris region, EGUsphere, 2024, 1–32, https://doi.org/10.5194/egusphere-2024-2826, 2024.

Eric, V.: MODIS/Terra Surface Reflectance 8-Day L3 Global 500m SIN Grid V061, https://doi.org/10.5067/MODIS/MOD09A1.061, 2021.

Feng, S., Lauvaux, T., Newman, S., Rao, P., Ahmadov, R., Deng, A., Díaz-Isaac, L. I., Duren, R. M., Fischer, M. L., Gerbig, C., Gurney, K. R., Huang, J., Jeong, S., Li, Z., Miller, C. E., O'Keeffe, D., Patarasuk, R., Sander, S. P., Song, Y., Wong, K. W., and Yung, Y. L.: Los Angeles megacity: a high-resolution land–atmosphere modelling system for urban CO_2 emissions, Atmospheric Chemistry and Physics, 16, 9019–9045, https://doi.org/10.5194/acp-16-9019-2016, 2016.

Fenner, D., Christen, A., Grimmond, S., Meier, F., Morrison, W., Zeeman, M., Barlow, J., Birkmann, J., Blunn, L., Chrysoulakis, N., Clements, M., Glazer, R., Hertwig, D., Kotthaus, S., König, K., Looschelders, D., Mitraka, Z., Poursanidis, D., Tsirantonakis, D., Bechtel, B., Benjamin, K., Beyrich, F., Briegel, F., Feigel, G., Gertsen, C., Iqbal, N., Kittner, J., Lean, H., Liu, Y., Luo, Z., McGrory, M., Metzger, S., Paskin, M., Ravan, M., Ruhtz, T., Saunders, B., Scherer, D., Smith, S. T., Stretton, M., Trachte, K., and Hove, M. V.: urbisphere-Berlin Campaign: Investigating Multiscale Urban Impacts on the Atmospheric Boundary Layer, Bulletin of the American Meteorological Society, 105, E1929 – E1961, https://doi.org/10.1175/BAMS-D-23-0030.1, 2024.

Gaudet, B. J., Lauvaux, T., Deng, A., and Davis, K. J.: Exploration of the impact of nearby sources on urban atmospheric inversions using large eddy simulation, Elementa: Science of the Anthropocene, 5, 60, https://doi.org/10.1525/elementa.247, 2017.

Glauch, T., Marshall, J., Gerbig, C., Botía, S., Gałkowski, M., Vardag, S. N., and Butz, A.: *pyVPRM*: a next-generation vegetation photosynthesis and respiration model for the post-MODIS era, Geoscientific Model Development, 18, 4713–4742, https://doi.org/10.5194/gmd-18-4713-2025, 2025.

Grell, G. A., Peckham, S. E., Schmitz, R., McKeen, S. A., Frost, G., Skamarock, W. C., and Eder, B.: Fully coupled online chemistry within the WRF model, Atmospheric Environment, 39, 6957–6975, https://doi.org/10.1016/j.atmosenv.2005.04.027, 2005.

Grimmond, C. S. B., Blackett, M., Best, M. J., Barlow, J., Baik, J.-J., Belcher, S. E., Bohnenstengel, S. I., Calmet, I., Chen, F., Dandou, A., Fortuniak, K., Gouvea, M. L., Hamdi, R., Hendry, M., Kawai, T., Kawamoto, Y., Kondo, H., Krayenhoff, E. S., Lee, S.-H., Loridan, T., Martilli, A., Masson, V., Miao, S., Oleson, K., Pigeon, G., Porson, A., Ryu, Y.-H., Salamanca, F., Shashua-Bar, L., Steeneveld, G.-J., Tombrou, M., Voogt, J., Young, D., and Zhang, N.: The International Urban Energy Balance Models Comparison Project: First Results from Phase 1, Journal of Applied Meteorology and Climatology, 49, 1268 – 1292, https://doi.org/10.1175/2010JAMC2354.1, 2010.

https://doi.org/10.5194/egusphere-2026-2109
Preprint. Discussion started: 1 July 2026

Gurney, K. R., Patarasuk, R., Liang, J., Song, Y., O'Keeffe, D., Rao, P., Whetstone, J. R., Duren, R. M., Eldering, A., and Miller, C.: The Hestia fossil fuel CO_2 emissions data product for the Los Angeles megacity (Hestia-LA), Earth System Science Data, 11, 1309–1335, https://doi.org/10.5194/essd-11-1309-2019, 2019.

Hedelius, J. K., Feng, S., Roehl, C. M., Wunch, D., Hillyard, P. W., Podolske, J. R., Iraci, L. T., Patarasuk, R., Rao, P., O'Keeffe, D., Gurney, K. R., Lauvaux, T., and Wennberg, P. O.: Emissions and topographic effects on column CO_2 variations, with a focus on the Southern California Megacity, Journal of Geophysical Research: Atmospheres, 122, 7200–7215, https://doi.org/10.1002/2017JD026455, 2017.

Hersbach, H., Bell, B., Berrisford, P., Hirahara, S., Horányi, A., Muñoz-Sabater, J., Nicolas, J., Peubey, C., Radu, R., Schepers, D., Simmons, A., Soci, C., Abdalla, S., Abellan, X., Balsamo, G., Bechtold, P., Biavati, G., Bidlot, J., Bonavita, M., De Chiara, G., Dahlgren, P., Dee, D., Diamantakis, M., Dragani, R., Flemming, J., Forbes, R., Fuentes, M., Geer, A., Haimberger, L., Healy, S., Hogan, R. J., Hólm, E., Janisková, M., Keeley, S., Laloyaux, P., Lopez, P., Lupu, C., Radnoti, G., de Rosnay, P., Rozum, I., Vamborg, F., Villaume, S., and Thépaut, J.-N.: The ERA5 global reanalysis, Quarterly Journal of the Royal Meteorological Society, 146, 1999–2049, https://doi.org/10.1002/qj.3803, 2020.

Hong, S.-Y., Dudhia, J., and Chen, S.-H.: A Revised Approach to Ice Microphysical Processes for the Bulk Parameterization of Clouds and Precipitation, Monthly Weather Review, 132, 103–120, https://doi.org/10.1175/1520-0493(2004)132<0103:ARATIM>2.0.CO;2, 2004.

Hong, S.-Y., Noh, Y., and Dudhia, J.: A New Vertical Diffusion Package with an Explicit Treatment of Entrainment Processes, Monthly Weather Review, 134, 2318 – 2341, https://doi.org/10.1175/MWR3199.1, 2006.

Hu, X.-M., Nielsen-Gammon, J. W., and Zhang, F.: Evaluation of Three Planetary Boundary Layer Schemes in the WRF Model, Journal of Applied Meteorology and Climatology, 49, 1831 – 1844, https://doi.org/10.1175/2010JAMC2432.1, 2010.

Huo, D., Huang, X., Dou, X., Ciais, P., Li, Y., Deng, Z., Wang, Y., Cui, D., Benkhelifa, F., Sun, T., Zhu, B., Roest, G., Gurney, K. R., Ke, P., Guo, R., Lu, C., Lin, X., Lovell, A., Appleby, K., DeCola, P. L., Davis, S. J., and Liu, Z.: Carbon Monitor Cities near-real-time daily estimates of CO_2 emissions from 1500 cities worldwide, Scientific Data, 9, 533, https://doi.org/10.1038/s41597-022-01657-z, 2022.

Iacono, M. J., Delamere, J. S., Mlawer, E. J., Shephard, M. W., Clough, S. A., and Collins, W. D.: Radiative forcing by long-lived greenhouse gases: Calculations with the AER radiative transfer models, JGR: Atmospheres, 113, https://doi.org/10.1029/2008JD009944, 2008.

ICOS, E. T. C., Bignotti, L., Loubet, B., Depuydt, J., Fortineau, A., Buysse, P., Coimbra, P., Viatte, C., Cailteau-Fischbach, C., Stagakis, S., Christen, A., Hilland, R., and Nicolini, G.: ETC L2 Fluxes from Paris Jussieu, 2022-12-31–2024-12-31, https://hdl.handle.net/11676/yPaka4Xe4XdQ-wdMxNbvGCTd, 2025.

Inness, A., Ades, M., Agustí-Panareda, A., Barré, J., Benedictow, A., Blechschmidt, A.-M., Dominguez, J. J., Engelen, R., Eskes, H., Flemming, J., Huijnen, V., Jones, L., Kipling, Z., Massart, S., Parrington, M., Peuch, V.-H., Razinger, M., Remy, S., Schulz, M., and Suttie, M.: The CAMS reanalysis of atmospheric composition, Atmospheric Chemistry and Physics, 19, 3515–3556, https://doi.org/10.5194/acp-19-3515-2019, 2019.

Janjic, Z. I.: The Step-Mountain Coordinate: Physical Package, MWR, 118, 1429–1443, https://doi.org/10.1175/1520-0493(1990)118<1429:TSMCPP>2.0.CO;2, 1990.

Janjic, Z. I.: The surface layer in the NCEP eta model in the eleventh conference on numerical weather prediction, Norfolk, VA, 19–23 August 1996, Amer. Meteor. Soc., Boston, MA, pp. 354–356, 1996.

Jiménez, P. A. and Dudhia, J.: Improving the Representation of Resolved and Unresolved Topographic Effects on Surface Wind in the WRF Model, Journal of Applied Meteorology and Climatology, 51, 300–316, https://doi.org/10.1175/JAMC-D-11-084.1, 2012.

Kiel, M., Eldering, A., Roten, D. D., Lin, J. C., Feng, S., Lei, R., Lauvaux, T., Oda, T., Roehl, C. M., Blavier, J.-F., and Iraci, L. T.: Urban-focused satellite CO_2 observations from the Orbiting Carbon Observatory-3: A first look at the Los Angeles megacity, Remote Sensing of Environment, 258, 112 314, https://doi.org/10.1016/j.rse.2021.112314, 2021.

https://doi.org/10.5194/egusphere-2026-2109
Preprint. Discussion started: 1 July 2026

Kljun, N., Calanca, P., Rotach, M. W., and Schmid, H. P.: A simple two-dimensional parameterisation for Flux Footprint Prediction (FFP), Geoscientific Model Development, 8, 3695–3713, https://doi.org/10.5194/gmd-8-3695-2015, 2015.

Kotthaus, S., Haeffelin, M., Drouin, M.-A., Dupont, J.-C., Grimmond, S., Haefele, A., Hervo, M., Poltera, Y., and Wiegner, M.: Tailored Algorithms for the Detection of the Atmospheric Boundary Layer Height from Common Automatic Lidars and Ceilometers (ALC), Remote Sensing, 12, https://doi.org/10.3390/rs12193259, 2020.

Kotthaus, S., Bravo-Aranda, J. A., Collaud Coen, M., Guerrero-Rascado, J. L., Costa, M. J., Cimini, D., O'Connor, E. J., Hervo, M., Alados-Arboledas, L., Jiménez-Portaz, M., Mona, L., Ruffieux, D., Illingworth, A., and Haeffelin, M.: Atmospheric boundary layer height from ground-based remote sensing: a review of capabilities and limitations, Atmospheric Measurement Techniques, 16, 433–479, https://doi.org/10.5194/amt-16-433-2023, 2023.

Krayenhoff, E. S., Jiang, T., Christen, A., Martilli, A., Oke, T. R., Bailey, B. N., Nazarian, N., Voogt, J. A., Giometto, M. G., Stastny, A., and Crawford, B. R.: A multi-layer urban canopy meteorological model with trees (BEP-Tree): Street tree impacts on pedestrian-level climate, Urban Climate, 32, 100 590, https://doi.org/10.1016/j.uclim.2020.100590, 2020.

Kusaka, H., Kondo, H., Kikegawa, Y., and Kimura, F.: A Simple Single-Layer Urban Canopy Model For Atmospheric Models: Comparison With Multi-Layer And Slab Models, Boundary-Layer Meteorology, 101, 329–358, https://doi.org/10.1023/A:1019207923078, 2001.

Lac, C., Donnelly, R. P., Masson, V., Pal, S., Riette, S., Donier, S., Queguiner, S., Tanguy, G., Ammoura, L., and Xueref-Remy, I.: CO_2 dispersion modelling over Paris region within the CO_2-MEGAPARIS project, Atmospheric Chemistry and Physics, 13, 4941–4961, https://doi.org/10.5194/acp-13-4941-2013, 2013.

Lauvaux, T., Schuh, A., Uliasz, M., Richardson, S., Miles, N., Andrews, A., Sweeney, C., Diaz-Isaac, L., Martins, D., Shepson, P., and Davis, K.: Constraining the CO2 budget of the corn belt: exploring uncertainties from the assumptions in a mesoscale inverse system, Atmospheric Chemistry and Physics, 12, 337–354, https://doi.org/10.5194/acp-12-337-2012, 2012.

Lauvaux, T., Miles, N. L., Deng, A., Richardson, S. J., Cambaliza, M. O., Davis, K. J., Gaudet, B., Gurney, K. R., Huang, J., O'Keefe, D., Song, Y., Karion, A., Oda, T., Patarasuk, R., Razlivanov, I., Sarmiento, D., Shepson, P., Sweeney, C., Turnbull, J., and Wu, K.: High-resolution atmospheric inversion of urban CO_2 emissions during the dormant season of the Indianapolis Flux Experiment (INFLUX), Journal of Geophysical Research: Atmospheres, 121, 5213–5236, https://doi.org/10.1002/2015JD024473, 2016.

Lei, R., Feng, S., Alexandre, D., Grégoire, B., Dien, W., John, C. L., Christopher, W. O., and Thomas, L.: Fossil fuel CO2 emissions over metropolitan areas from space: A multi-model analysis of OCO-2 data over Lahore, Pakistan, Remote Sensing of Environment, 264, 112 625, https://doi.org/10.1016/j.rse.2021.112625, 2021.

Lian, J., Bréon, F.-M., Broquet, G., Lauvaux, T., Zheng, B., Ramonet, M., Xueref-Remy, I., Kotthaus, S., Haeffelin, M., and Ciais, P.: Sensitivity to the sources of uncertainties in the modeling of atmospheric CO_2 concentration within and in the vicinity of Paris, Atmospheric Chemistry and Physics, 21, 10 707–10 726, https://doi.org/10.5194/acp-21-10707-2021, 2021.

Lian, J., Lauvaux, T., Utard, H., Bréon, F.-M., Broquet, G., Ramonet, M., Laurent, O., Albarus, I., Chariot, M., Kotthaus, S., Haeffelin, M., Sanchez, O., Perrussel, O., Denier van der Gon, H. A., Dellaert, S. N. C., and Ciais, P.: Can we use atmospheric CO_2 measurements to verify emission trends reported by cities? Lessons from a 6-year atmospheric inversion over Paris, Atmospheric Chemistry and Physics, 23, 8823–8835, https://doi.org/10.5194/acp-23-8823-2023, 2023.

Lian, J., Laurent, O., Chariot, M., Lienhardt, L., Ramonet, M., Utard, H., Lauvaux, T., Bréon, F.-M., Broquet, G., Cucchi, K., Millair, L., and Ciais, P.: Development and deployment of a mid-cost CO_2 sensor monitoring network to support atmospheric inverse modeling for quantifying urban CO_2 emissions in Paris, EGUsphere, 2024, 1–26, https://doi.org/10.5194/egusphere-2024-125, 2024.

https://doi.org/10.5194/egusphere-2026-2109
Preprint. Discussion started: 1 July 2026

Lipson, M., Grimmond, S., Best, M., Chow, W. T. L., Christen, A., Chrysoulakis, N., Coutts, A., Crawford, B., Earl, S., Evans, J., Fortuniak, K., Heusinkveld, B. G., Hong, J.-W., Hong, J., Järvi, L., Jo, S., Kim, Y.-H., Kotthaus, S., Lee, K., Masson, V., McFadden, J. P., Michels, O., Pawlak, W., Roth, M., Sugawara, H., Tapper, N., Velasco, E., and Ward, H. C.: Harmonized gap-filled datasets from 20 urban flux tower sites, Earth System Science Data, 14, 5157–5178, https://doi.org/10.5194/essd-14-5157-2022, 2022.

Lohou, F., Gouttevin, I., Canut-Rocafort, G., Dupont, J.-C., Derrien, S., Vial, A., Pique, E., Meyerfeld, Y., Saïd, F., Deliot, Y., and Merzisen, H.: Surface turbulent fluxes - 4 French long-term measurement - Processing with EddyPro, https://doi.org/10.25326/768, 2018.

Looschelders, D. and et al.: [Title to be updated], in preparation, 2026.

Looschelders, D., Christen, A., Grimmond, S., Kotthaus, S., Fenner, D., Dupont, J.-C., Haeffelin, M., and Morrison, W.: Inter-Instrument Variability of Vaisala CL61 Lidar-Ceilometer's Attenuated Backscatter, Cloud Properties and Mixed-Layer Height, Meteorological Applications, 32, e70 088, https://doi.org/10.1002/met.70088, e70088 MET-25-0027.R2, 2025.

Lopez-Coto, I., Hicks, M., Karion, A., Sakai, R. K., Demoz, B., Prasad, K., and Whetstone, J.: Assessment of Planetary Boundary Layer Parameterizations and Urban Heat Island Comparison: Impacts and Implications for Tracer Transport, Journal of Applied Meteorology and Climatology, 59, 1637 – 1653, https://doi.org/10.1175/JAMC-D-19-0168.1, 2020.

Loridan, T., Grimmond, C. S. B., Grossman-Clarke, S., Chen, F., Tewari, M., Manning, K., Martilli, A., Kusaka, H., and Best, M.: Trade-offs and responsiveness of the single-layer urban canopy parametrization in WRF: An offline evaluation using the MOSCEM optimization algorithm and field observations, Quarterly Journal of the Royal Meteorological Society, 136, 997–1019, https://doi.org/10.1002/qj.614, 2010.

Lwasa, S., Seto, K., X., B., Blanco, H., Gurney, K., Kilkis, S., Lucon, O., Murakami, J., Pan, J., Sharifi, A., and Yamagata, Y.: 2022: Urban systems and other settlements, In IPCC, 2022: Climate Change 2022: Mitigation of Climate Change. Contribution of Working Group III to the Sixth Assessment Report of the Intergovernmental Panel on Climate Change, https://doi.org/10.1017/9781009157926.010, 2022.

Mahadevan, P., Wofsy, S. C., Matross, D. M., Xiao, X., Dunn, A. L., Lin, J. C., Gerbig, C., Munger, J. W., Chow, V. Y., and Gottlieb, E. W.: A satellite-based biosphere parameterization for net ecosystem CO2 exchange: Vegetation Photosynthesis and Respiration Model (VPRM), Global Biogeochemical Cycles, 22, https://doi.org/10.1029/2006GB002735, 2008.

Martilli, A., Clappier, A., and Rotach, M. W.: An Urban Surface Exchange Parameterisation for Mesoscale Models, Boundary-Layer Meteorology, 104, 261–304, https://doi.org/10.1023/A:1016099921195, 2002.

McGrath-Spangler, E. L., Molod, A., Ott, L. E., and Pawson, S.: Impact of planetary boundary layer turbulence on model climate and tracer transport, Atmospheric Chemistry and Physics, 15, 7269–7286, https://doi.org/10.5194/acp-15-7269-2015, 2015.

Morrison, W., Looschelders, D., Céspedes, J., Claxton, B., Drouin, M.-A., Dupont, J.-C., Faucheux, A., Haeffelin, M., Holst, C. C., Kotthaus, S., Masson, V., McGregor, J., Price, J., Zeeman, M., Grimmond, S., and Christen, A.: Harmonised boundary layer wind profile dataset from six ground-based Doppler wind lidars in a transect across Paris, France, Earth System Science Data, 17, 6507–6529, https://doi.org/10.5194/essd-17-6507-2025, 2025.

Pappaccogli, G., Zonato, A., Martilli, A., Buccolieri, R., and Lionello, P.: MLUCM BEP + BEM: an offline one-dimensional multi-layer urban canopy model based on the BEP + BEM scheme, Geoscientific Model Development, 18, 7129–7145, https://doi.org/10.5194/gmd-18-7129-2025, 2025.

Peckham, S. E., Grell, G. A., McKeen, S. A., Ahmadov, R., Wong, K. Y., Barth, M., Pfister, G., Wiedinmyer, C., Fast, J. D., Gustafson, W. I., Ghan, S. J., Zaveri, R., Easter, R. C., Barnard, J., Chapman, E., Hewson, M., Schmitz, R., Salzmann, M., and Beck, V. Freitas, S. R.: WRF-Chem version 3.8.1 user's guide, Earth System Research Laboratory (U.S.), Global Systems Division, https://doi.org/10.7289/V5/TM-OAR-GSD-48, 2017.

https://doi.org/10.5194/egusphere-2026-2109
Preprint. Discussion started: 1 July 2026

Salamanca, F. and Martilli, A.: A new Building Energy Model coupled with an Urban Canopy Parameterization for urban climate simulations—part II. Validation with one dimension off-line simulations, Theoretical and Applied Climatology, 99, 345–356, https://doi.org/10.1007/s00704-009-0143-8, 2010.

Sarmiento, D. P., Davis, K. J., Deng, A., Lauvaux, T., Brewer, A., and Hardesty, M.: A comprehensive assessment of land surface-atmosphere interactions in a WRF/Urban modeling system for Indianapolis, IN, Elementa: Science of the Anthropocene, 5, 23, https://doi.org/10.1525/elementa.132, 2017.

Schuh, A. E., Otte, M., Lauvaux, T., and Oda, T.: Far-field biogenic and anthropogenic emissions as a dominant source of variability in local urban carbon budgets: A global high-resolution model study with implications for satellite remote sensing, Remote Sensing of Environment, 262, 112 473, https://doi.org/10.1016/j.rse.2021.112473, 2021.

Skamarock, W. C., Klemp, J. B., Dudhia, J., Gill, D. ., Liu, Z., Berner, J., Wang, W., Powers, J. G., Duda, M. G., Barker, D. M., and Huang, X.-Y.: A Description of the Advanced Research WRF Version 4, NCAR Tech. Note NCAR/TN-556+STR, p. 145pp., https://doi.org/10.5065/1dfh-6p97, 2019.

Stagakis, S., Bignotti, L., Lan, C., Vogt, R., Holst, C., Herig-Coimbra, P., Nicolini, G., Hilland, R., Christen, A., Fortineau, A., Depuydt, J., Jahn, C., Nief, G., Buysse, P., Lozano, M., Laurent, O., Cailteau-Fischbach, C., Viatte, C., Ramonet, M., Papale, D., Mauder, M., and Loubet, B.: Quality-controlled half-hourly EC fluxes and meteorological variables from Paris (FR-Jus, FR-Rmv & FR-Vin), ICOS ERIC – Carbon Portal, https://doi.org/10.18160/V4ZG-81AC, 2025.

Staufer, J., Broquet, G., Bréon, F.-M., Puygrenier, V., Chevallier, F., Xueref-Rémy, I., Dieudonné, E., Lopez, M., Schmidt, M., Ramonet, M., Perrussel, O., Lac, C., Wu, L., and Ciais, P.: The first 1-year-long estimate of the Paris region fossil fuel CO_2 emissions based on atmospheric inversion, Atmospheric Chemistry and Physics, 16, 14 703–14 726, https://doi.org/10.5194/acp-16-14703-2016, 2016.

Stauffer, D. R. and Seaman, N. L.: Multiscale Four-Dimensional Data Assimilation, Journal of Applied Meteorology and Climatology, 33, 416 – 434, https://doi.org/10.1175/1520-0450(1994)033<0416:MFDDA>2.0.CO;2, 1994.

Stull, B. R.: An Introduction to Boundary Layer Meteorology., Journal of Fluid Mechanics, 224, 660–661, https://doi.org/10.1017/S0022112091211921, 1988.

Sun, E., Wang, X., Ye, H., Wu, S., Shi, H., Li, D., An, Y., and Li, C.: Improving urban CO_2 spatial distribution modelling using multi-source data, Urban Climate, 55, 101 902, https://doi.org/10.1016/j.uclim.2024.101902, 2024.

Super, I., Dellaert, S. N. C., Visschedijk, A. J. H., and Denier van der Gon, H. A. C.: Uncertainty analysis of a European high-resolution emission inventory of CO_2 and CO to support inverse modelling and network design, Atmospheric Chemistry and Physics, 20, 1795–1816, https://doi.org/10.5194/acp-20-1795-2020, 2020.

Taylor, T. E., Eldering, A., Merrelli, A., Kiel, M., Somkuti, P., Cheng, C., Rosenberg, R., Fisher, B., Crisp, D., Basilio, R., Bennett, M., Cervantes, D., Chang, A., Dang, L., Frankenberg, C., Haemmerle, V. R., Keller, G. R., Kurosu, T., Laughner, J. L., Lee, R., Marchetti, Y., Nelson, R. R., O'Dell, C. W., Osterman, G., Pavlick, R., Roehl, C., Schneider, R., Spiers, G., To, C., Wells, C., Wennberg, P. O., Yelamanchili, A., and Yu, S.: OCO-3 early mission operations and initial (vEarly) XCO2 and SIF retrievals, Remote Sensing of Environment, 251, 112 032, https://doi.org/10.1016/j.rse.2020.112032, 2020.

Thompson, G., Field, P. R., Rasmussen, R. M., and Hall, W. D.: Explicit Forecasts of Winter Precipitation Using an Improved Bulk Microphysics Scheme. Part II: Implementation of a New Snow Parameterization, MWR, 136, 5095–5115, https://doi.org/10.1175/2008MWR2387.1, 2008.

Vogelezang, D. H. P. and Holtslag, A. A. M.: Evaluation and model impacts of alternative boundary-layer height formulations, Boundary-Layer Meteorology, 81, 245–269, https://doi.org/10.1007/BF02430331, 1996.

https://doi.org/10.5194/egusphere-2026-2109
Preprint. Discussion started: 1 July 2026

Wolf, T., Pettersson, L. H., and Esau, I.: A very high-resolution assessment and modelling of urban air quality, Atmospheric Chemistry and Physics, 20, 625–647, https://doi.org/10.5194/acp-20-625-2020, 2020.

Ye, X., Lauvaux, T., Kort, E. A., Oda, T., Feng, S., Lin, J. C., Yang, E. G., and Wu, D.: Constraining Fossil Fuel CO2 Emissions From Urban Area Using OCO-2 Observations of Total Column CO2, Journal of Geophysical Research: Atmospheres, 125, e2019JD030 528, https://doi.org/10.1029/2019JD030528, e2019JD030528 2019JD030528, 2020.

Ye, X., Li, W., Lauvaux, T., Lin, S., Zhang, Z., Lin, Y., Hua, J., You, Q., and Lin, J.: Constraining anthropogenic CO2 emissions using dense observations from OCO-3: Disentangling observed imprints over Xiamen-Zhangzhou-Quanzhou metropolitan area and challenges, Urban Climate, 63, 102 591, https://doi.org/10.1016/j.uclim.2025.102591, 2025.

Zhao, X., Chen, J., Marshall, J., Gałkowski, M., Hachinger, S., Dietrich, F., Shekhar, A., Gensheimer, J., Wenzel, A., and Gerbig, C.: Understanding greenhouse gas (GHG) column concentrations in Munich using the Weather Research and Forecasting (WRF) model, Atmospheric Chemistry and Physics, 23, 14 325–14 347, https://doi.org/10.5194/acp-23-14325-2023, 2023.